



THE HONG KONG
POLYTECHNIC UNIVERSITY

香港理工大學

Pao Yue-kong Library

包玉剛圖書館

Copyright Undertaking

This thesis is protected by copyright, with all rights reserved.

By reading and using the thesis, the reader understands and agrees to the following terms:

1. The reader will abide by the rules and legal ordinances governing copyright regarding the use of the thesis.
2. The reader will use the thesis for the purpose of research or private study only and not for distribution or further reproduction or any other purpose.
3. The reader agrees to indemnify and hold the University harmless from and against any loss, damage, cost, liability or expenses arising from copyright infringement or unauthorized usage.

IMPORTANT

If you have reasons to believe that any materials in this thesis are deemed not suitable to be distributed in this form, or a copyright owner having difficulty with the material being included in our database, please contact lbsys@polyu.edu.hk providing details. The Library will look into your claim and consider taking remedial action upon receipt of the written requests.

HIGHLY FLEXIBLE SOLUTION- PROCESSED SOLAR CELLS

ZHANG YAOKANG

PhD

The Hong Kong Polytechnic University

2018

The Hong Kong Polytechnic University

Institute of Textiles and Clothing

Highly Flexible Solution-Processed Solar Cells

ZHANG YAOKANG

**A Thesis Submitted in Partial Fulfillment of the Requirements for
the Degree of Doctor of Philosophy**

January 2018

Certificate of Originality

I hereby declare that this thesis is my own work and that, to the best of my knowledge and belief, it reproduces no material previously published or written, nor material that has been accepted for the award of any other degree or diploma, except where due acknowledgement has been made in the text.

_____ (Signed)

Yaokang Zhang

January 2018

In Memorial of a Familiar Friend

ABSTRACT

Flexible thin-film solar cells such as organic solar cells (OSCs), dye-sensitized solar cells (DSSCs), perovskite solar cells (PSCs) have attracted tremendous attention in recent years. Such solar cells are easy to fabricate and potentially high-efficient, and they can be flexible once fabricated on flexible substrates. However, there are two major issues for most of the reported thin-film solar cells. First, the fabrication of these solar cells requires high temperature or vacuum deposition technologies, which are neither low-cost nor scalable. Second, these solar cells employ transparent conducting oxides (TCOs) as transparent electrodes, which are not suitable for flexible applications due to their mechanical brittleness. Recently, there has been some reports on fabricating thin-film solar cells by low-cost solution-based roll-to-roll (R2R) process, but the solar cell efficiency was too low for practical applications. In this thesis, these issues are tackled by developing and optimizing of several solution-based deposition technologies through chemical approaches.

First, the chemical fabrication of Cu electrodes by polymer-assisted metal deposition (PAMD) was investigated. PAMD is an advanced electroless deposition (ELD) technology for metal thin films. Multiple examples of patterned Cu electrodes which were obtained by either patterning the catalytic precursor (PCP) or patterning the functional polymer (PFP) were demonstrated. The advantages and disadvantages of these two approaches were discussed.

Second, the application of nitric acid annealed poly(3,4-ethylenedioxythiophene) polystyrene sulfonate (n-PEDOT:PSS) on semi-transparent perovskite solar cells (st-PSCs) was studied. The optical and electrical properties of n-PEDOT:PSS were characterized by multiple

approaches to evaluate its eligibility as transparent electrode. Then, the n-PEDOT:PSS electrodes were applied on st-PSCs as both top electrodes and bottom electrodes. Highly efficient st-PSCs based on n-PEDOT:PSS electrodes were fabricated, and they were integrated with monocrystalline Si (c-Si) solar cells to form 4-terminal tandem solar cells. Furthermore, highly flexible st-PSCs were fabricated on polyethylene terephthalate (PET) and polyimide (PI) substrates. Such examples indicated the superior flexibility of n-PEDOT:PSS electrodes over the traditional TCOs.

Third, all-solution-processed ultrathin OSCs were designed and fabricated. The OSCs combined solution-processed Cu electrodes and PEDOT:PSS electrodes together on ultrathin PI substrates, which were also fabricated by solution-based coating technique. The excellent flexibility of the OSCs were verified by repeated stretch-compress test of the OSCs on pre-stretched elastomers.

In addition, BHF that can improve the light absorption of OSCs and PSCs were fabricated by one-step soft lithography molding. The optical transmittance and haze effect of the BHF was studied in detail, while the anti-reflection and light-trapping effects of BHF was characterized by the current density-voltage (J - V) and external quantum efficiency (EQE) measurements of the solar cells.

In conclusion, highly flexible PSCs and OSCs were fabricated by fully-solution-based processes. The solution-processed Cu and PEDOT:PSS electrodes were highly compatible with flexible PSCs and OSCs. Such solution-processed PSCs and OSCs showed satisfactory efficiency as well as excellent mechanical flexibility. In principle, these solution-based strategies for PSCs and OSCs are also versatile for the fabrication of other electronic devices based on metal or polymer conductors. Hence, this work is believed

to have great impact on the fields of flexible energy harvesting/storage devices, displays, sensors, and etc.

LIST OF PUBLICATIONS

Related Journal Publications

1. **Yaokang Zhang**, Zhongwei Wu, Peng Li, Luis K. Ono, Yabing Qi, Jixiang Zhou, Hui Shen, Charles Surya, Zijian Zheng, “Full-solution-processed TCO-free Semi-transparent Perovskite Solar Cells for Tandem and Flexible Applications”, *Adv. Energy Mater.* **2018**, DOI: 10.1002/aenm.201701569.

2. Kan Li[†], **Yaokang Zhang**[†], Hongyu Zhen, Helin Wang, Shenghua Liu, Feng Yan, Zijian Zheng, “Versatile Biomimetic Haze Film for Efficiency Enhancement of Photovoltaic Devices”, *J. Mater. Chem. A* **2017**, *5*, 969-974.
([†] equal contribution)

3. You Yu[†], Xiang Xiao[†], **Yaokang Zhang**[†], Kan Li, Casey Yan, Xiaoling Wei, Lina Chen, Hongyu Zhen, Hang Zhou, Shengdong Zhang, Zijian Zheng, “Photo-reactive and Metal-Platable Copolymer Inks for High-Throughput, Room-Temperature Printing of Flexible Metal Electrodes for Thin-Film Electronics”, *Adv. Mater.* **2016**, *28*, 4926-4934. ([†] equal contribution)

4. Kan Li, Hongyu Zhen, Liyong Niu, Xu Fang, **Yaokang Zhang**, Ruisheng Guo, You Yu, Feng Yan, Haifeng Li, Zijian Zheng, “Full-Solution Processed Flexible Organic Solar Cells Using Low-Cost Printable Copper Electrodes”, *Adv. Mater.* **2014**, *26*, 7271-7278.

Other Journal Publications

1. You Yu, **Yaokang Zhang**, Kan Li, Casey Yan, Zijian Zheng, “Bio-Inspired Chemical Fabrication of Stretchable Transparent Electrodes”, *Small* **2015**, *28*, 3444-3449.

2. Kan Li, **Yaokang Zhang**, Hongyu Zhen, Liyong Niu, Xu Fang, Zhike Liu, Feng Yan, Weidong Shen, Haifeng Li, Zijian Zheng, “Printed Light-Trapping Nanorelief Cu Electrodes for Full-Solution-Processed Flexible Organic Solar Cells”, *Mater. Res. Express* **2016**, 3, 074006.

Patents

Zijian Zheng, Kan Li, Hongyu Zhen, **Yaokang Zhang**, “Low-Cost Rose Petal Textured Film with High Transmission Haze for Photovoltaic Cells”, US Patent, submitted.

Conference Presentations

Yaokang Zhang, Zijian Zheng, “Vein-based Stretchable Transparent Electrodes Fabricated by Polymer-assisted Metal Deposition”, **The 16th International Meeting on Information Display (IMID 2016)**, August 23 – 26, 2016, ICC Jeju, Jeju, Korea.

ACKNOWLEDGEMENTS

First of all, I would like to express my sincerest thanks to my supervisor Prof. Zijian Zheng, for his long-term guidance and insightful enlightenment. His comprehensive knowledge on material science and rigorous attitude to scientific research have always been motivating me. The 4-years study has become a valuable period, during which I learnt writing and presentation skills, the way to originate scientific ideas, the manner of designing and executing experiments, and the ability of data analysis.

I've also been grateful to all members in Prof. Zheng's research group during these 4 years: Dr. Xuechang Zhou, Dr. Xiaoling Wei, Dr. Xinlei Ma, Dr. Zhilu Liu, Dr. Ruisheng Guo, Dr. Tingting Gao, Dr. Xuqing Liu, Dr. You Yu, Dr. Hongyu Zhen, Dr. Kan Li, Dr. Libin Liu, Dr. Ruitao Zhou, Dr. Yiyi She, Dr. Zhuang Xie, Dr. Liyong Niu, Dr. Lina Chen, Dr. Yu Yang, Dr. Jian Chang, Dr. Guoqiang Liu, Dr. Ting Xiao, Dr. Dongrui Wang, Dr. Dongdong Chen, Dr. Zhongwei Wu, Dr. Lei Yao, Dr. Qi Gan, Dr. Zhijun Ma, Mr. Chaojian Chen, Ms. Kate Yip, Ms. Casey Yan, Mr. Xiang Xiao, Ms. Younseon Wang, Mr. Shijin Zhu, Ms. Sze Wing Ng, Ms. Qiyao Huang, Mr. Shuaichen Wang, Mr. Peng Li, Mr. Xi Lu, Mr. Jian Shang, Ms. Yujing Zhu and Mr. Chuan Xie. They have always been reliable partners and sincere friends. In the meantime, I would like to thank other coworkers, Dr. Shenghua Liu and Prof. Feng Yan in the Department of Applied Physics, and Dr. Zhiwei Ren, Dr. Jixiang Zhou and Prof. Charles Surya in the Department of Electronic and Information Engineering.

I also gratefully acknowledge the financial support from the Hong Kong Polytechnic University (1-ZVK1), Guangdong-Hong Kong Technology Cooperation Funding Scheme (grant number: 2014B050505010), ECS of Hong Kong (PolyU 5030/12P), GRF of Hong Kong (PolyU 5036/13P), and

the Natural Science Foundation of Zhejiang Province (Grant No. LY15F050010).

Moreover, I express deep gratitude to my parents for their love, understanding, and support. It would be better if they could stop urging me on looking for a girlfriend.

At last, I would like to thank my dearest friends. The postgraduate study was tedious, tough and frustrating for most of the time, but with their company I afraid no longer.

TABLE OF CONTENTS

ABSTRACT	I
LIST OF PUBLICATIONS.....	IV
ACKNOWLEDGEMENTS.....	VI
LIST OF TABLES AND FIGURES.....	XII
LIST OF ABBREVIATIONS	XVIII
CHAPTER 1. INTRODUCTION	1
1.1 Background and challenge	1
1.2 Research Objectives	3
1.3 Research Originality	3
1.4 Outline of the Thesis	4
CHAPTER 2. LITERATURE REVIEW	6
2.1 The Development of OSCs and PSCs	6
2.1.1 Mechanism and Evolution of Solar Cells	8
2.1.2 Solar Cells with Organic Absorbers	13
2.1.3 Solar Cells with perovskite Absorbers	18
2.2 Solution-processed OSCs and PSCs.....	22
2.2.1 Solution Process for Active Materials	23
2.2.2 Solution Process for Electrodes	27
2.3 Flexible OSCs and PSCs	32
2.3.1 TCO-based Flexible OSCs and PSCs	33
2.3.2 TCO-free Flexible OSCs and PSCs.....	35
2.4 Conclusions and Summary of Research Gaps.....	37
CHAPTER 3. METHODOLOGY	40
3.1 Materials Preparation	40
3.1.1 PAMD Fabrication of Bottom Electrodes	40
3.1.2 Replica Molding of Rose Petals for BHF	41

3.2 Characterization.....	42
3.2.1 Optical Microscopy	42
3.2.2 Atomic Force Microscopy (AFM).....	42
3.2.3 Scanning Electron Microscopy (SEM).....	43
3.2.4 Raman Spectroscopy	44
3.2.5 X-ray Photoelectron Spectroscopy (XPS) and Ultraviolet Photoelectron Spectroscopy (UPS).....	44
3.2.6 Ultraviolet-Visible Spectroscopy (UV-Vis)	45
3.2.7 Current-Voltage (<i>I-V</i>) Characterization of Solar Cells	45
3.2.8 External Quantum Efficiency (EQE).....	45
CHAPTER 4. FABRICATION OF METAL ELECTRODES VIA ELECTROLESS DEPOSITION	47
4.1 Introduction	47
4.2 Experimental Section	49
4.2.1 Preparation of Cu Plating Bath	49
4.2.2 PAMD of Cu Electrodes by Patterning the Catalyst	49
4.2.3 Synthesis of Photoreactive Copolymer.....	49
4.2.4 Preparation of Copolymer Patterns by Printing Techniques	50
4.2.5 PAMD of Cu Electrodes by Patterning the Polymer	51
4.2.6 Characterization.....	52
4.3 Results and Discussions	52
4.4 Conclusions	57
CHAPTER 5. SOLUTION-PROCESSED TCO-FREE SEMI- TRANSPARENT PEROVSKITE SOLAR CELLS FOR FLEXIBLE AND TANDEM APPLICATIONS.....	58
5.1 Introduction	58
5.2 Experimental Section	60
5.2.1 Materials and synthesis.....	60

5.2.2 Device fabrication.....	61
5.2.3 Characterizations	62
5.3 Results and Discussions	63
5.3.1 Fabrication and Solar Cell Structure.....	63
5.3.2 Nitric Acid-annealed PEDOT:PSS	65
5.3.3 Solar Cell Performance.....	69
5.4 Conclusions	76
CHAPTER 6. ALL-SOLUTION PROCESSED ULTRATHIN ORGANIC SOLAR CELLS WITH EXTRA-HIGH MECHANICAL FLEXIBILITY AND DURABILITY	77
6.1 Introduction	77
6.2 Experimental Section	79
6.2.1 Materials	79
6.2.2 Fabrication of Cu Bottom Electrodes	79
6.2.3 Fabrication of OSCs	80
6.2.4 Characterization.....	81
6.3 Results and Discussions	81
6.3.1 Structure of All-solution-processed Organic Solar Cell.....	81
6.3.2 Photovoltaic Characteristics of the All-solution Processed OSCs	84
6.4 Conclusions	87
CHAPTER 7. BIOMIMETIC HAZE FILMS FOR EFFICIENCY ENHANCEMENT OF ORGANIC AND PEROVSKITE SOLAR CELLS.....	89
7.1 Introduction	89
7.2 Experimental Section	91
7.2.1 Materials	91
7.2.2 PSC fabrication.....	92

7.2.3 OSC fabrication	92
7.2.4 Characterization	93
7.3 Results and Discussions	93
7.4 Conclusions	102
CHAPTER 8. CONCLUSIONS AND OUTLOOK	104
8.1 Conclusions	104
8.2 Outlooks	106
REFERENCES	107

LIST OF TABLES AND FIGURES

Table 2.1 Comparison of 3 generations of solar cells in efficiency and cost.

Table 2.2 Chemical structure and HOMO energy level of some donor polymers used in BHJ OSCs.

Table 5.1. Summary of photovoltaic characteristics of PSCs fabricated on glass.

Table 5.2 Summary of state-of-the-art st-PSCs reported in the literature and by us

Table 5.3 Summary of device performance of four-terminal tandem solar cells and flexible st-PSCs.

Table 7.1. Photovoltaic characteristics of c-Si solar cells, OSCs and PSCs with and without BHF.

Table 7.2. Comparison of optical haze and transmittance for some typical haze materials reported previously.

Figure 2.1 Structure of OSCs and PSCs. (a) Structural illustration of OSC and PSC. (b) Illustration of three types of OSC and a P3HT:PCBM heterojunction. (c) Energy diagram of various perovskites and ETL/HTL materials.

Figure 2.2 Theories of solar cells. (a) Energy diagram of the *p-n* junction of a c-Si solar cell. (b) Chemical structure and energy diagram of poly(*p*-phenylene vinylene) (PPV):C₆₀ system for OSCs. (c) Equivalent circuit of a solar cell. (d) Illustration of *I-V* curves of a solar cell.

Figure 2.3 Mechanism and applications of BHJ OSCs. (a) Charge separation mechanism of BHJ OSCs. (b) Structure and energy diagram of a PCDTBT:PC₇₁BM based BHJ OSC. (c) Structure and optical image of a semitransparent OSC. (d) Structure and SEM cross-sectional image of a 2-terminal double-junction tandem OSC.

Figure 2.4 Chemical structure and physic properties of organolead halide perovskites. (a) Chemical structure of CH₃NH₃PbI₃. (b) Optical image (top) and XRD pattern (bottom) of CH₃NH₃PbI₃ single crystal. (c) Absorption coefficient of several photovoltaic active materials over near-UV to near-IR

spectrum. (d) Time-resolved photoluminescence spectrum of $\text{CH}_3\text{NH}_3\text{PbI}_{3-x}\text{Cl}_x$.

Figure 2.5 Perovskite materials for photovoltaic applications. (a) Several possible ABX_3 perovskite, and highest experimental PCE of ABX_3 perovskite-based PSCs. (b) Optical images of some mixed perovskites and their XRD patterns. (c) UV-visible absorption spectra, PL spectra, TEM image and XRD patterns of CsPbI_3 quantum dots.

Figure 2.6 Schematics of R2R processed organic solar modules. (a) to (d) Optical images of a 100 m organic solar foil. (e) Schematic illustration of a R2R process for the fabrication of organic solar modules.

Figure 2.7 Solution methods for organic active materials. (a) Illustration of distinct stages during spin-coating. (b) Illustration of slot-die coating process for the fabrication of OLED modules.

Figure 2.8 Perovskite active materials processed by different methods in liquid phase. (a) One-step spin-coating^{[1][1][1]}, (b) two-step dipping, (c) two-step “inter-diffusion”, (d) one-step anti-solvent dripping, (e) doctor-blading, (f) slot-die coating, and (g) pressure processing method.

Figure 2.9 Solution processed transparent electrodes for OSCs and PSCs. (a) Highly conductive PEDOT:PSS (hc-PEDOT:PSS) based OSC. The conductivity of the PEDOT:PSS is improved by solvent post-treatment. (b) Highly efficient flexible OSC based on printed Ag current collecting grids and hc-PEDOT:PSS electrode. (c) st-PSC based on embedded Ni mesh and PEDOT:PSS electrode. (d) ITO-free OSC based on AgNW electrode.

Figure 2.10 Solution processed metal back electrodes. (a) Comparison of flatbed screen-printed, rotary screen-printed, flexographic-printed, and inkjet-printed Ag back electrodes for flexible OSC modules. (b) Fully solution-processed flexible OSC based on Cu bottom electrode. The Cu electrode is deposited by PAMD.

Figure 2.11 Mechanics and design for TCO-based OSCs and PSCs. (a) Bending fatigue of ITO on PET substrate. (b) Flexible OSC based on ITO/AgNW/ITO electrode. (c) Flexible PSC based on low temperature

processed NiO_x HTL. (d) Comparison of flexible PSCs with PEDOT:PSS and PhNa-1T HTLs. (e) Highly efficient flexible PSC using PTAA as HTL.

Figure 2.12 TCO-free flexible OSCs and PSCs. (a) R2R fabrication of TCO-free organic tandem solar cell module on PET substrate. (b) TCO-free semitransparent PSC on flexible NOA63 substrate. (c) TCO-free flexible PSC based on Ag mesh/PEDOT:PSS hybrid electrode. (d) TCO-free OSC on ultrathin PET substrate. (e) Ultrathin high power-per-weight PSC on 1.4 μm-thick PET substrate. (f) TCO-free stretchable OSC on PDMS substrate.

Figure 3.1 Schematics of a PAMD process for the fabrication of Cu bottom electrodes of flexible OSCs.

Figure 3.2 Schematics of the fabrication process for BHF.

Figure 3.3 Illustration of the components and working mechanism of AFM.

Scheme 4.1 Schematic illustration of PAMD by two strategies. PCP: Metal pattern achieved by printing the catalytic precursor. PFP: Metal pattern achieved by printing the functional polymer.

Figure 4.1 Characterization of ELD Cu electrode. (a) XPS analysis of ELD Cu. (b) Optical image of 2.5 × 2.5 cm Cu patterns on glass (left), PET (middle) and PI (right). (c) Optical images of ELD Cu on multiple organic substrates. (d) schemes and optical images of ELD Cu patterns fabricated by PFP method: interdigitated Cu electrodes on cotton fabric by screen printing (top), Cu meshes on PET by soft lithography molding (middle), and Cu strips on PET by inkjet printing (bottom). Scale bars are 1 cm, 150 μm, and 2 cm, respectively. (e) AFM topographic image of ELD Cu surface fabricated by PCP method. Scale bar is 2.5 μm. (f) AFM lateral profiles of copolymer pattern and ELD Cu fabricated by PFP method.

Figure 5.1 Fabrication and solar cell structure (a) Schematic illustration of the fabrication steps of TCO-free st-PSC. (b) SEM cross-sectional image (left) and energy-level diagram (right) of the TCO-free st-PSC. Scale bar is 500 nm.

Figure 5.2 Physical properties of nitric acid treated PEDOT:PSS. (a) Profile diagram of a scratched edge of the PDEOT:PSS films measured by AFM. (b)

UV-Vis spectra of ITO, p-PEDOT:PSS, s-PEDOT:PSS and n-PEDOT:PSS on glass substrates. (c) UPS spectra ($\text{He-I}\alpha = 21.22 \text{ eV}$) showing the secondary electron onset (left side) and valance state region (right side) of the ITO reference sample, p-PEDOT:PSS, s-PEDOT:PSS and n-PEDOT:PSS.

Figure 5.3 (a) XPS spectra ($\text{Al-K}\alpha = 1253.6 \text{ eV}$) of the C $1s$, O $1s$ and S $2p$ core levels of the ITO, p-PEDOT:PSS, s-PEDOT:PSS and n-PEDOT:PSS. (b) Fitted XPS spectra corresponding to the C $1s$, O $1s$ and S $2p$ core levels of the p-PEDOT:PSS, s-PEDOT:PSS and n-PEDOT:PSS. (c) XPS N $1s$ core level of ITO, p-PEDOT:PSS, s-PEDOT:PSS and n-PEDOT:PSS. (d) Raman spectra of p-PEDOT:PSS, s-PEDOT:PSS and n-PEDOT:PSS.

Figure 5.4 Photovoltaic performance of semi-transparent solar cells. (a) J-V curves of reference devices with different annealing time of perovskite layer. (b) Transmittance spectra of ITO ref. and TCO-free semi-transparent devices over the wavelength range of 400 to 1300 nm. (c) and (d) J-V curves of opaque reference cell and ITO based semi-transparent reference cell, and TCO-free semi-transparent perovskite solar cell. (e) and (f) EQE spectra of ITO based and TCO-free semi-transparent perovskite solar cells.

Figure 5.5 Photovoltaic performance of tandem solar cells. (a) and (b) J-V curves of ITO ref./c-Si and TCO-free/c-Si four-terminal tandem devices. (c) and (d) EQE spectra of ITO ref./c-Si and TCO-free/c-Si four-terminal tandem devices.

Figure 5.6 (a) J-V curves of TCO-free@PET. (b) Normalized photovoltaic characteristics of TCO-free@PET during 1000 bending at a radius of 5 mm. (c) J-V curves of TCO-free@PI. (d) Photographs of ultrathin TCO-free@PI conformably attached on a 1 mL syringe (left), and crumbled by a tweezer (right).

Scheme 6.1 Schematics of the fabrication process. (1) Spin-coating PDMS on glass substrate, curing at $80 \text{ }^\circ\text{C}$ for 1h; (2) Spin-coating PI precursor solution on PDMS, curing at $180 \text{ }^\circ\text{C}$ for 2h; (3) Surface modification of PI by PMETAC; (4) Electroless deposition of Cu strips; (5) Spin-coating of PEI, curing at $100 \text{ }^\circ\text{C}$ for 10 min; (6) Spin-coating of P3HT:PCBM solution, curing

at 145 °C for 5 min; (7) Spin-coating of PEDOT:PSS, curing at 130 °C for 10 min; (8) Peeling-off the device for glass substrate.

Figure 6.1 (a) Schematic illustration of the ultrathin OSC (left), and optical image of an ultrathin OSC that is attached on the surface of a glove (right). Scale bar is 1 cm. (b) AFM topographic images of PI substrate, Cu electrode, and P3HT:PCBM active layer. Scale bar is 2 μm .

Figure 6.2 Photovoltaic performance of all-solution-processed OSCs. (a) J - V curve of the champion device. (b) Comparison of all-solution-processed OSC and reference OSC which uses vacuum-deposited Cu electrodes instead of ELD Cu electrodes. (c) Logarithmic J - V curves of all-solution-processed device and the reference device. The solid curves are J - V curves under illuminated state, while the dash curves are J - V curves under dark state.

Figure 6.3 (a) Optical image of the stretch-compress system. The shape change of a device during one stretch-compress cycle is demonstrated on the top. (b) I - V curves of a device at different compress strain. (c) Comparison of the J - V curves of the all-solution-processed OSC before and after stretch and compress. (d) Normalized PCE of all-solution-processed OSC and reference OSC during 1,000 stretch-compress cycles.

Figure 7.1 (a) Optical image of rose petal and BHF. SEM images of the top surface of rose petal (b) and textured surface of BHF (c). Scale bar is 30 μm for each graph. (d) SEM cross-sectional image of the BHF. Scale bar is 10 μm . (e) Illustration of the light-scattering and anti-reflection mechanism of the BHF. (f) Illustration of the haze effect of the BHF. As shown in the scheme, the BHF (thickness = 300 μm) was placed atop a paper printed with the word “Haze”, where h indicates the distance between the paper surface and BHF top surface (i.e., the textured surface).

Figure 7.2 (a) The experimental setup for diffusion and haze transmittance measurement (b) The UV-Vis absorption spectra of diffusion and absorption haze. (c) and (d) The schematic diagram of experimental setup for scattering light power angular distribution measurement, and the corresponding results tested between wavelength range of 400 ~ 800 nm, respectively. (e) Scattering

light power angular distribution of BHF at specific 3 wavelengths, 500nm, 600nm and 700nm. (f) The absorption spectra of bare Si wafer, flat PDMS film-covered Si wafer, and BHF-covered Si wafer.

Figure 7.3 The comparison of average haze and diffusion transmittance of reported haze films and BHF from 400 nm to 800 nm. Details are listed in Table 7.2.

Figure 7.4 (a) Structural illustration of BHF-enhanced PSC and OSC. The BHF can be attached and detached at any time. (b) *J-V* curves comparison of the best solar cells with and without BHF. (c) EQE spectra of solar cells w/ and w/o BHF. (d) The normalized photocurrent values of PSCs w/ and w/o BHF versus the complementary angle of the incident light (i.e., 0 means the incident angle is 90°).

LIST OF ABBREVIATIONS

AFM	Atomic force microscope
BHF	Biomimetic haze film
DMF	Dimethylformamide
DMSO	Dimethyl sulfoxide
DSSC	Dye-sensitized solar cell
ELD	Electroless deposition
EQE	External quantum efficiency
ETL	Electron transport layer
FTO	Fluorine-doped tin oxide
HOMO	Highest occupied molecular orbital
HTL	Hole transport layer
ITO	Indium tin oxide
LUMO	Lowest unoccupied molecular orbital
OSC	Organic solar cell
P3HT	Poly(3-hexylthiophene-2,5-diyl)
PAMD	Polymer-assisted metal deposition
PCBM	[6,6]-phenyl-C ₆₁ -butyric acid methyl ester
PCE	Power conversion efficiency
PDMS	Polydimethylsiloxane
PEDOT:PSS	Poly(3,4-ethylenedioxythiophene):polystyrene Sulfonate
PEG	Poly(ethylene glycol)
PET	Poly(ethylene terephthalate)
PI	Polyimide
PMETAC	Poly[2-(methacryloyloxy)ethyl-trimethylammonium chloride]
R2R	Roll-to-roll
SEM	Scanning electron microscopy
TCO	Transparent conducting oxide
UPS	Ultraviolet photoelectron spectroscopy
XPS	X-ray photoelectron spectroscopy
XRD	X-ray diffraction

CHAPTER 1. INTRODUCTION

1.1 Background and challenge

The emerging solar cells such as dye-sensitized solar cells (DSSCs)^[2-4], organic solar cells (OSCs)^[5-7] and perovskite solar cells (PSCs)^[8-11] have dominated the research field of photovoltaics for over 2 decades. The power conversion efficiency (PCE) of these types of solar cells boosts rapidly within the past years, especially for the PSC which firstly appeared in 2009 in a form of DSSC^[8]. Recently, the record efficiency of PSC has reached 22.7^[12], which is comparable with the best monocrystalline Si (c-Si) based solar cell^[13].

The advantages of these emerging solar cells not only come from the high efficiency, but also from the low manufacturing cost and potential applications on flexible and wearable electronics^[14-16]. Unlike traditional Si based solar cells which require very thick Si absorber because of low absorption coefficient^[17], the organic^[18] or perovskite^[19] absorber can be as thin as 10 to several hundred nanometers. Such characteristics enable thin-film solar cells with a total thickness of several micrometers. As a result, the entire device can be highly flexible when fabricated on thin polymeric substrates^[20-22]. However, such thin-film solar cells always suffer from mechanical failure under bending or stretching^[23]. To fulfill the requirement of flexible or wearable applications, this problem need to be solved.

One major issue that limits the flexibility is the transparent conducting oxide (TCO) layer, which is widely applied as the transparent electrode for solar cells^[24, 25]. Indium tin oxide (ITO), for example, is well known for high optical transmittance (>85% over visible light spectrum) and good electrical conductivity ($<15\Omega/\square$)^[26-28]. However, the brittle nature of ITO limits its applications for flexible and wearable electronics^[29, 30]. As a result, efforts are put on investigating substitutes for ITO, which show good mechanical flexibility while owning high optical transmittance and electrical conductivity.

These novel transparent electrodes such as graphene and graphene based electrodes^[31, 32], metal thin film^[33, 34], and metal oxide/metal/metal oxide electrodes^[35, 36] show comparable, or even better optical and electrical performance comparing with TCOs while exhibiting much better mechanical flexibility. The problem is that the fabrication of these electrodes requires high cost vacuum processes, which are not compatible with large area and high throughput roll-to-roll (R2R) process^[37-39].

On the contrary, transparent conducting polymers are highly flexible. A typical example is poly(3,4-ethylenedioxythiophene) polystyrene sulfonate (PEDOT:PSS), which is widely used as transparent electrode^[40, 41] or hole conductor^[42, 43] in OSCs, especially for flexible applications. Such polymers are soluble in water or common organic solvents, and thus are compatible with low cost and high throughput solution coating or printing techniques, such as spin coating^[44], slot-die coating^[45], doctor-blade coating^[46], inkjet printing^[47], and screen printing^[48]. However, the poor conductivity and stability of these polymers limit the efficiency of solar cells with polymer electrodes. As a result, most of the flexible OSCs which are available on market employ ITO electrodes. Although efforts are put on improving the conductivity of PEDOT:PSS by doping^[49] or combining with metal mesh^[50], the conductivity and transmittance can hardly be satisfactory at the same time.

To address these challenges, this thesis will focus on designing and manufacturing of highly flexible solar cells based on organic or perovskite active materials. A fully solution-processing strategy that incorporates polymer-assisted metal deposition (PAMD)^[51] and transfer printing techniques will be investigated in this study. On the one hand, the viability of employing PAMD or vacuum-deposited metal as bottom electrodes will be studied for both organic and perovskite solar cells. On the other hand, highly conductive PEDOT:PSS obtained by acid-annealing process will be employed as transparent electrodes for PSCs. A dry transfer-printing method will be applied when employing PEDOT:PSS as top electrodes to avoid the moisture-induced degradation of organolead halide perovskite material^[52].

Each interfacial layer in organic and perovskite solar cells will be carefully studied and optimized to obtain highly efficient solar cells without sacrificing the flexibility.

In addition, a biomimetic haze film (BHF) will be investigated as an anti-reflection and light-trapping layer to improve the light absorption efficiency of solar cells. Such enhancement in light absorption will result in higher short-circuit current density, and thus improve the power conversion efficiency (PCE) of solar cells correspondingly. The BHF will be manufactured by low cost soft-molding method with stretchable elastomer polydimethylsiloxane (PDMS), which is highly compatible with flexible solar cells.

1.2 Research Objectives

This study focuses on the methodologies of manufacturing TCO-free high performance solar cells with good flexibility. In details, the objectives are listed as follows:

1. To fabricate highly conductive and smooth Cu bottom electrodes by PAMD.
2. To fabricate high performance PEDOT:PSS transparent electrodes by acid-annealing method.
3. To characterize and optimize OSCs and PSCs based on the solution-processed electrodes listed above.
4. To incorporate BHF with OSCs and PSCs for light-harvesting enhancement.

1.3 Research Originality

This study reveals facile approaches to fabricating TCO-free flexible OSCs and PSCs by various of solution-based technologies.

First, high performance PSCs are fabricated by a fully solution-based approach that is free from TCOs and vacuum processes for the first time. Both cathode and anode of the PSC are made by nitric acid annealed PEDOT:PSS (n-PEDOT:PSS), which make the entire PSC semitransparent. Highly

efficient semitransparent PSC (st-PSC)/Si tandem solar cell is demonstrated based on our fully solution-processed st-PSC, showing a great potential for low cost solar energy harvesting in the future.

Second, the entire fabrication incorporates low cost and high throughput solution processes, and is completely high temperature-free. Such processes show good compatibility with polymeric substrates, which are essential for flexible OSCs and PSCs. As a proof-of-concept, highly flexible OSCs and PSCs are fabricated on flexible polyethylene terephthalate (PET) and ultrathin polyimide (PI) substrates. The PSCs on PET substrates show good retention under repeated bending, which results from our TCO-free solar cell configuration. More importantly, fully solution-processed stretchable OSCs on solution-processed PI substrates are realized for the first time, by attaching our ultrathin OSC on pre-stretched elastomers. Such highly flexible energy harvesting devices are promising for flexible and wearable electronics.

In addition, this study also contributes to the anti-reflection and light-trapping technologies for solar cells by designing and fabricating BHF based on the surface texture of natural rose petal. Such biomimetic strategy is simple and effective, which is significant for the further lowering of the electricity generated by the conversion of solar energy.

1.4 Outline of the Thesis

This thesis is organized as follows:

Chapter 1 briefly introduces the state-of-the-art of OSCs and PSCs, and the challenges in the field of flexible OSCs and PSCs. As a potential solution of these challenges, the purpose and significance of this study are stated.

Chapter 2 contains the detailed research background, including the development of solution-processed, and flexible OSCs/PSCs. Several aspects in solar cell fabrication, such as material choice and film deposition technologies, are discussed in detail.

Chapter 3 lists the methodology of this study for solar cell fabrication and characterization.

In Chapter 4, PAMD method is introduced for the fabrication of electrolessly plated Cu electrodes. Two patterning strategies are demonstrated and compared for the fabrication of Cu electrodes on multiple substrates.

In Chapter 5, a fully solution-based strategy is illustrated for the fabrication of TCO-free st-PSC. Transfer-printable n-PEDOT:PSS is employed as both anode and cathode for st-PSC. The optical and electrical of n-PEDOT:PSS is carefully characterized. Flexible st-PSCs are fabricated and characterized.

In Chapter 6, ultrathin OSCs based on our full solution strategy are studied in detail. The solar cells are fabricated on ultrathin PI substrates. Stretchable OSC is obtained by attaching the OSC on 50% pre-stretched elastomer, and its current density-voltage ($J-V$) retention is tested under repeated stretch and compress.

In Chapter 7, the fabrication and characterization of BHF are discussed. The BHF is applied to OSCs and PSCs to investigate the effectiveness of BHF on different types of solar cells.

In Chapter 8, the results of this work are summarized, and the outlook of flexible OSC and PSC is discussed.

CHAPTER 2. LITERATURE REVIEW

2.1 The Development of OSCs and PSCs

The configuration of typical planar OSCs and PSCs is similar. Typically, both OSC and PSC require two electrodes, one of which should be transparent (typically ITO or FTO) while the other is opaque metal electrode. Sometimes both electrodes are designed to be transparent for constructing semitransparent OSCs or PSCs for specific applications such as tandem solar cells^[53, 54] and energy harvesting curtain wall for buildings^[55]. Generally, it is necessary to insert ETL and HTL between active layer and electrodes for high efficient OSCs and PSCs. An ETL is a thin film of n-type semiconductors with a lowest unoccupied molecular orbital (LUMO)/conduction band (CB) of ~ -4.0 eV such as ZnO^[56] and TiO₂^[57], while an HTL is made by p-type semiconductors with a highest occupied molecular orbital (HOMO)/valence band (VB) of ~ -5.0 eV such as PEDOT:PSS^[58] and 2,2',7,7'-tetrakis(N,N-di-p-methoxyphenyl-amine)9,9'-spirobifluorene (spiro-OMeTAD)^[59]. Such ETL/HTL selectively inject electron/hole to each electrode after the generation of electron/hole pairs (or excitons) when illuminated. However, the solar cells can be ETL or HTL-free if the work-function of the electrodes are modified to certain level^[60, 61]. As illustrated in Figure 2.1, *p-i-n* type is customarily regarded as “normal structure” for OSC, while *n-i-p* type is called as “inverted structure”. Conversely, normal (or conventional) PSC usually refers to *n-i-p* type, because PSC is evolved from Grätzel Cell, a type of DSSC whose structure is TCO/TiO₂/Dye/Electrolyte/Counter Electrode^[3, 8].

Apart from the electrodes and ETLs/HTLs, the diverse active materials are always the emphasis of OSC and PSC research. Three generations of OSCs, namely single layer^[62], bilayer^[63] and bulk heterojunction^[64] (BHJ) have been developed in the past decades (Figure 2.1b). To date, bulk heterojunction absorber that blends polymer donor and fullerene acceptor is the most popular active layer for OSCs. Such BHJ OSCs boost the efficiency of OSC from $<1\%$

to >10%, and the record efficiency of a polymer donor/polymer acceptor based OSC has reached >13% very recently^[63, 65]. The most well-studied system is poly(3-hexylthiophene-2,5-diyl) (P3HT): [6,6]-phenyl-C61-butyric acid methyl ester (PCBM) blend based heterojunction^[66]. A post-annealing process is needed for improving the crystallinity of the polymer after film formation (Figure 2.1b)^[67]. Although the record efficiency of this system is not very high^[68], the P3HT:PCBM OSCs are easy to manufacture, and the photovoltaic performance of P3HT:PCBM OSCs is relatively stable in air^[69, 70]. Hence, this system is ideal for fundamental studies of flexible solar cells.

Comparing with organic active materials, the perovskite materials for photovoltaic applications are not diversified. Basically, the chemical formula of perovskite is ABX_3 , where A is Cs^+ , $CH_3NH_3^+$ (MA^+) or $H_2NCH(=NH)^+$ (FA^+), B is Pb^{2+} or Sn^{2+} , and C is I^- , Br^- or Cl^- . Sometimes it can be the combination of these ions, such as $MAPbI_{3-x}Cl_x$ ^[21] and $(FAPbI_3)_x(MAPbBr_3)_{1-x}$ ^[71]. It's worth noting that the bandgap of perovskites can be tuned easily by adjusting the ratio of $MA^+ : FA^+$ or $Br^- : I^-$ ^[54, 72, 73]. As shown in Figure 2.1c, the bandgap of perovskites ranges from 1.5 eV to 2.2 eV, which makes it very suitable for tandem solar cell applications with Si solar cell, copper indium gallium selenide (CIGS) solar cell, or even another PSC with different bandgap^[74-76].

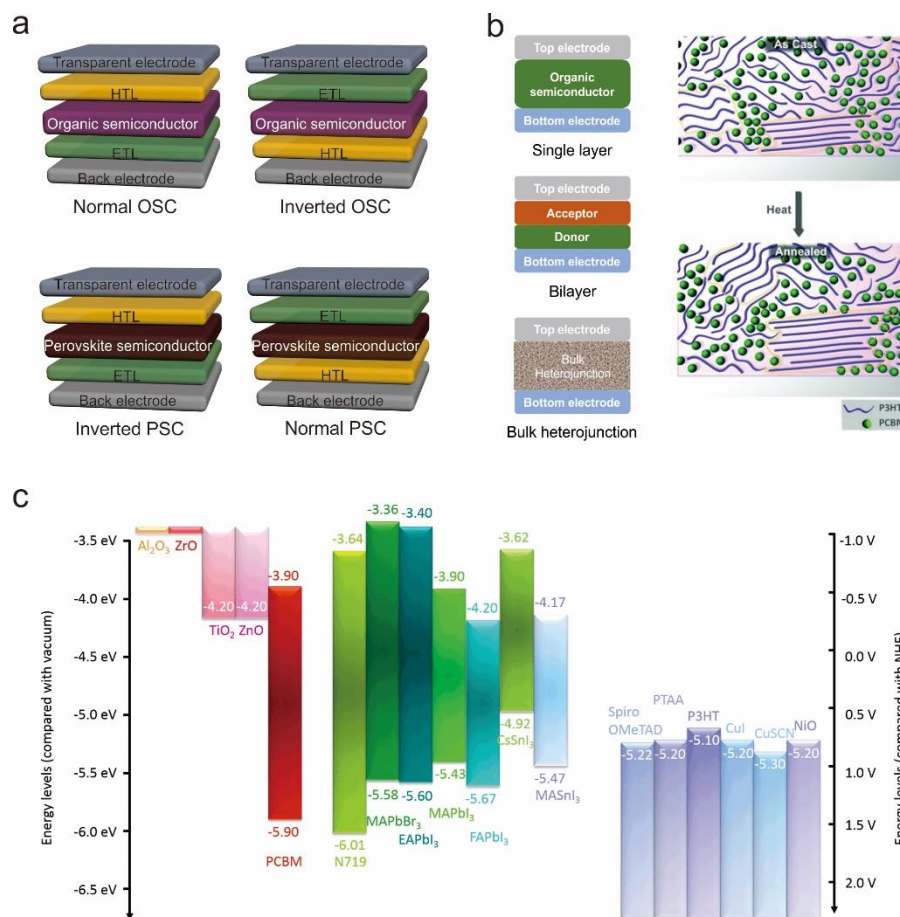


Figure 2.1 Structure of OSCs and PSCs. (a) Structural illustration of OSC and PSC. (b) Illustration of three types of OSC and a P3HT:PCBM heterojunction^[67]. (c) Energy diagram of various perovskites and ETL/HTL materials^[77].

2.1.1 Mechanism and Evolution of Solar Cells

Similar to the term photoelectric effect which means the emission of electrons/free carriers from a material under the illumination of light, photovoltaic effect refers to the generation of electric current/voltage in a material once exposed to light. The only distinction is that it will be defined as photovoltaic effect if the light generated charge carrier is still restricted in the material. The photovoltaic effect can be observed on many semiconductors. Once the energy of a photon is higher than the bandgap of the semiconductor, the photon can be absorbed by the semiconductor, and an electron-hole pair/exciton may generate in the semiconductor.

A solar cell is a device that converts solar energy to electricity by photovoltaic effect. To make use of the photovoltaic effect, the generated electron-hole pairs should be separated and led to an external load. The separation of the charge carrier is always realized by diffusion following a gradient formed by electrochemical potential. Diverse approaches such as the built-in voltage of a p - n junction between p -type Si and n -type Si^[78], or the pass of electron from the LUMO of an organic donor to the LUMO of an organic acceptor^[79] can be the driven force for charge carrier separation.

As a diode, the electronic characteristics of a solar cell can be analyzed by an equivalent circuit (Figure 2.2c). According to Shockley's diode equation^[80], the current that passes through the diode I_D is:

$$I_D = I_0 \left\{ e^{\frac{V_j}{nV_T}} - 1 \right\} \quad (1)$$

where I_0 is the reverse saturation current of the diode, V_j is the voltage across the diode (and shunt resistance R_{SH}), and V_T the thermal voltage which is equal to kT/q . For ideal solar cells, the shunt resistance is supposed to be high enough. Thus, the open circuit voltage (V_{OC} , the voltage across the solar cell when $I = 0$) is:

$$V_{OC} \approx \frac{nkT}{q} \ln \left(\frac{I_L}{I_0} + 1 \right) \quad (2)$$

When the solar cell is operated at short circuit state, the short circuit current I_{SC} is:

$$I_{SC} \approx I_L \quad (3)$$

considering that the series resistance R_S is low, and R_{SH} is high.

The V_{OC} and I_{SC} of a solar cell can be obtained by I - V characterization as illustrated in Figure 2.2d. The I - V curve of solar cell is measured under airmass 1.5 (AM1.5) solar spectra if there is no specific illustration. The current is 0 when the applied bias is equal to V_{OC} , and the photocurrent at 0 bias (i.e. at short circuit) is the I_{SC} . The PCE of a solar cell is:

$$PCE = \frac{P_{max}}{P_{solar}} = \frac{P_{max}}{100mW/cm^2 \times A} \quad (4)$$

where P_{max} is the maximum power output of the solar cell, P_{solar} is the power of the sunlight on device which is 100 mW/cm^2 times the active area (A) of the solar cell. The fill factor (FF) of the solar cell is defined as:

$$FF = \frac{P_{max}}{V_{OC} \times I_{SC}} = \frac{PCE \times 100 \text{ mW/cm}^2 \times A}{V_{OC} \times I_{SC}} = \frac{PCE \times 100 \text{ mW/cm}^2}{V_{OC} \times I_{SC}} \quad (5)$$

where I_{SC} stands for short circuit current density.

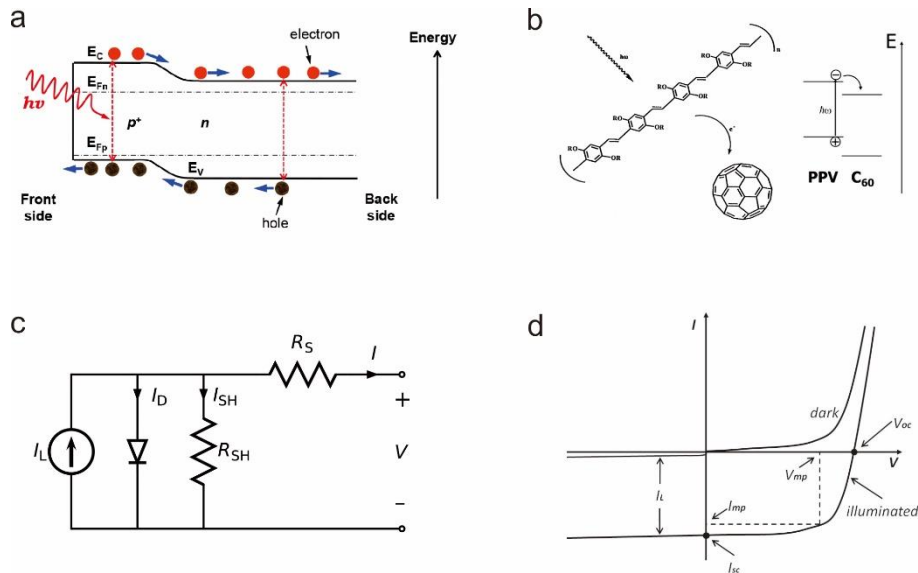


Figure 2.2 Theories of solar cells. (a) Energy diagram of the p - n junction of a c -Si solar cell. (b) Chemical structure and energy diagram of poly(p -phenylene vinylene) (PPV): C_{60} system for OSCs. (c) Equivalent circuit of a solar cell. (d) Illustration of I - V curves of a solar cell.

The first solar cell was based on Se-Au junction by Charles Fritts in 1883 after the discovery of light-generated current on Se semiconductor in 1873^[81]. The efficiency was only $\sim 1\%$ at that time. Although the photoelectric/photovoltaic effect has been studied for decades since then, the first commercial solar cell didn't appear until 1954^[82]. The Si based solar cell showed $\sim 6\%$ efficiency, which was significantly higher than all previous reports. Soon after that, Si solar cells were used for space applications in late 1950s, and then started to appear in daily life after 1970s. The record efficiency of c -Si solar cell has reached 26.7% very recently^[83], and the price of Si solar cell has decreased to $\sim \$0.20/W$, which is >300 times lower than that of 1970s^[84].

Three generations of solar cells have been developed during the past half a century^[85]. The 1st generation is Si wafer based solar cells. These devices show quite high efficiency and very long lifetime (>10 years), but the crystalline Si wafers are thick (~200 μm), rigid, and expensive in price. In addition, the fabrication process of c-Si solar cell is very complicated and time consuming. Starting from the 1970s, research interests have been transferred to the 2nd generation solar cells, which are based on thin-film technologies. Typical examples are amorphous Si (a-Si:H)^[86], CdTe^[87], and CIGS solar cells. Such active materials are thin (~1 μm), flexible and relatively low cost. However, the efficiency of such 2nd generation solar cells are not satisfactory. For example, the record efficiency of a-Si:H solar cell is 14.0%^[88], which is only half of c-Si efficiency record. The deposition of amorphous Si film requires plasma-enhanced chemical vapor deposition (PECVD)^[89]. Although it is much easier than the fabrication of c-Si wafer, the PECVD technology requires a chamber which limits the scalability.

To overcome these problems, the 3rd solar cells based on advanced thin-film technologies emerged in 1990s. Grätzel et al. developed the first highly efficient modern DSSC based on dye-sensitized high-surface-area TiO₂ anode and liquid electrolyte. Although the record efficiency is still inferior to the best 2nd generation solar cells, the DSSC is manufactured by cost efficient solution processes rather than traditional vacuum technologies. In addition, the TiO₂ anode and iodine based electrolyte are cheap and abundant. At the same time, break-through has been achieved on BHJ OSCs, which are significantly more efficient than the single junction and bilayer OSCs reported previously. The organic absorbers show extraordinary absorption coefficient comparing with traditional Si semiconductors. Hence, the thickness of these absorbers can be confined to hundreds of nanometers, and even <100 nm^[90]. The bandgap of the organic semiconductors ranges from 1.4 eV to 3 eV^[91], providing broad absorption spectra from near UV to near IR. As a result, many of them are designed for double-junction^[53], and even triple-junction^[92] tandem applications. More importantly, the OSCs are perfectly compatible with R2R process, which is low-cost, high-throughput

and scalable^[93, 94]. The OSCs are also compatible with flexible polymeric substrates because they are low temperature processable. Such R2R processed flexible OSCs are available in market recent years^[95]. Similar to the organic semiconductors, the quantum dot semiconductors (e.g., PbS quantum dot) show tunable bandgap and good solution processability^[96]. Hence, the research in quantum dot solar cells (QDSCs) is of great interests in recent years.

Evolved from the DSSCs, organolead halide perovskites have been regarded as one of the most promising materials for photovoltaic applications in the past few years^[97, 98]. At first, liquid electrolyte was used in perovskite-sensitized solar cell, resulting in only 3.8% PCE^[81]. In 2011, Im et al. employed perovskite quantum dots as sensitizer in perovskite sensitized solar cell, yielding an efficiency of 6.5%^[99]. The liquid electrolyte induced stability issue that the perovskite material will dissolve in it spontaneously. To solve this problem, Kim et al. demonstrated all-solid-state perovskite sensitized solar cell by using spiro-OMeTAD as HTL for the first time, and the efficiency was boosted to 9% in 2012^[59]. Later, Lee et al. reported 10.9% efficiency perovskite solar cell with insulating mesoporous Al₂O₃ scaffold instead of mesoporous TiO₂ semiconductor^[100]. This result indicated that the perovskite materials not only function as sensitizer, but also work as photoactive semiconductor in the solar cells. Solar cells based on perovskite active layers started to become the research focus, and diverse types of planar PSCs have been developed since then^[71, 101, 102].

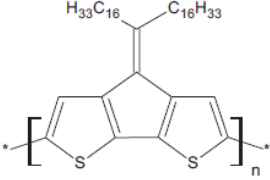
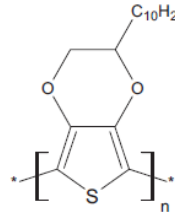
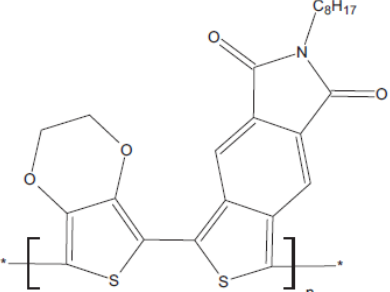
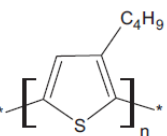
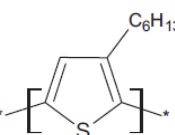
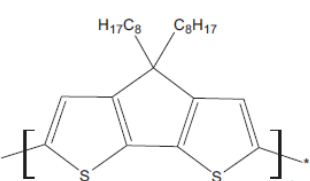
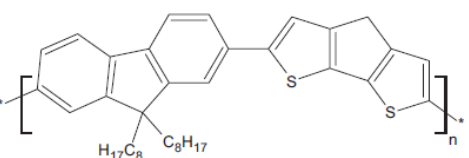
Table 2.1 Comparison of 3 generations of solar cells in efficiency and cost.

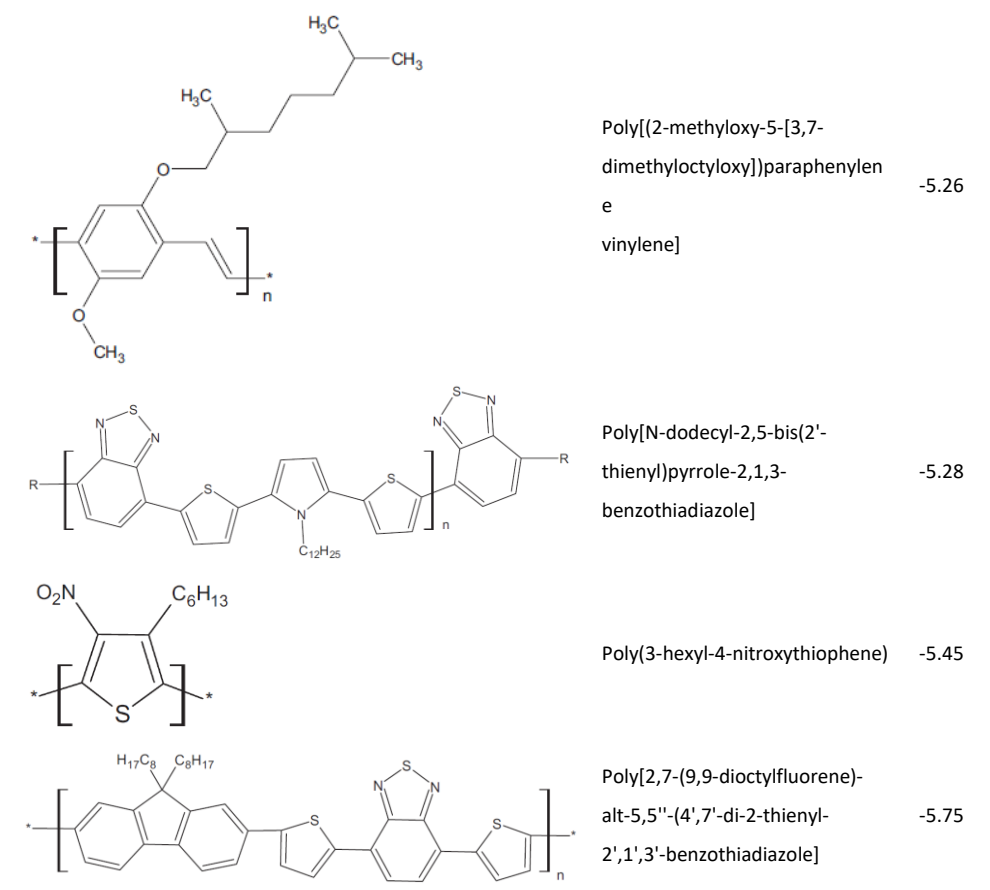
Generations	Efficiency	Cost	Flexibility	Examples
1 st (wafers)	High	High	Low	c-Si
2 nd (thin-films)	Low	Low	High	CIGS, CdTe, a- Si:H
3 rd (advanced thin-films)	High	Low	High	OSC, DSSC, QDSC, PSC

2.1.2 Solar Cells with Organic Absorbers

As discussed in previous sections, BHJ OSCs have dominated the research field for the past 2 decades. The BHJ consists of an electron donor which is usually conjugated polymer/copolymer, and an electron acceptor which is fullerene or its derivatives. Generally, the donor polymers belong to several categories, such as polythiophene and its derivatives, 2,1,3-benzothiadiazole based polymers, pyrrolo[3,4-c]pyrrole-1,4-dione (DPP) and benzo[1,2-b;4,5-b']dithiophene (DBT) based polymers^[103-106]. Table 2.2 listed the chemical structure and HOMO energy level of typical donor polymers for BHJ OSCs.

Table 2.2 Chemical structure and HOMO energy level of some donor polymers used in BHJ OSCs^[107].

Structure	Name	HOMO O (eV)
	Poly-[2,6-(4-dihexadecylmethylenecyclopentadithiophene)]	-4.82
	Poly-[(1'dodecyl)-3,4-ethylenoxythiophene]	-4.83
	Poly-[(3,4-ethylenedioxythiophene)-N-2'-ethyl-4,5-dicarboxylic-imidebenzo[c]thiophene]	-4.84
	Poly(3-butylthiophene)	-5.05
	Poly(3-hexylthiophene)	-5.1
	Poly[2,5-(7,7-dioctyl)-cyclopentadithiophene]	-5.15
	Poly[2,7-9,9-dioctylfluorene)-alt-2,6-cyclopentadithiophene]	-5.25



Under the illumination of sunlight, the photons are absorbed by the BHJ active material, generating bounded electron-hole pairs, a.k.a., excitons. The excitons then dissociate to electrons and holes at the interfaces of donor and acceptor inside the BHJ, and then diffuse to the LUMO energy level of acceptor and the HOMO energy level of the donor, respectively (Figure 2.3a). Afterwards, the electrons and holes are transferred to the cathode and anode respectively under the driven force of the built-in electric field.

To form an efficient BHJ, the energy level of the donor and acceptor should be tuned carefully. The energy level of the HOMO and LUMO of the donor material should be higher than that of the acceptor material for efficient charge separation, and this offset should be neither too large nor too small. On the one hand, there will be significant energy loss if the energy offset is too large because the V_{OC} of the solar cells is closely related to the energy gap between the LUMO of the acceptor and the HOMO of the donor^[107]. For example, for a poly({4,8-bis[(2-ethylhexyl)oxy]benzo[1,2-b:4,5-

b']dithiophene-2,6-diyl}{3-fluoro-2-[(2-ethylhexyl)carbonyl]thieno[3,4-b]thiophenediyl}) (PTB7):PC₇₁BM system based OSC, the HOMO of PTB7 is -5.15 eV, and the LUMO of PC₇₁BM is -4.3 eV. The $q \cdot V_{OC}$ is ~0.75 eV, which is smaller than the energy gap of 0.85 eV^[108]. On the other hand, the charge separation efficiency will be too low if the offset is too small. As a result, such an ideal offset is designed as 0.2 to 0.3 eV^[109]. However, traditional donor material such as P3HT has a HOMO energy level of ~-5 eV, which is 1 eV higher than that of PCBM. Hence the energy loss of such system is very obvious, and the efficiency of P3HT:PCBM based OSCs is always quite low (<4% for most reported P3HT:PCBM OSCs). More advanced systems employ lower HOMO polymers such as poly[N-9''-heptadecanyl-2,7-carbazole-alt-5,5-(4',7'-di-2-thienyl-2',1',3'-benzothiadiazole) (PCDTBT), yielding efficiency over 6% (Figure 2.3b).

Typically, a BHJ OSC employs one TCO electrode and one opaque metal electrode, thus the entire device is usually opaque. However, semitransparent OSCs are required for some specific applications such as photovoltaic windows and tandem solar cells^[110]. Comparing with other active materials, organic absorbers are highly compatible with semitransparent photovoltaic window and tandem applications because the absorbers are thin enough to transmit part of the visible light, and the color/absorption spectrum is tunable by adjusting the bandgap of the donor and acceptor materials. As a result, the entire solar cell will be semitransparent if both electrodes are transparent. The material for transparent electrodes is another research hotspot, which will be discussed in the following sections. Figure 2.3c is an example for semitransparent OSC based on ITO and graphene electrodes. Graphene is known for its high conductivity, high optical transmittance and good mechanical robustness^[32, 111]. Although the synthesis of high quality graphene film requires high temperature chemical vapor deposition (CVD) technique, the synthesized graphene film can be printed onto target substrates by various transfer-printing methods^[112, 113]. In this work, the authors obtained highly conductive graphene electrodes by chemical doping, and the OSCs showed 2.7% efficiency, which is comparable to opaque P3HT:PCBM OSCs.

One important application for semitransparent solar cell is multijunction tandem solar cell. For single-junction solar cells, the theoretical maximum PCE is ~33.7%, which is known as *Shockley–Queisser limit*^[114]. However, the theoretical limitation upgrades to 68% and 86% for infinite junctions of tandem solar cells under unconcentrated and concentrated sunlight, respectively^[115]. This is because the broader solar spectrum can be covered by stacking absorbers with different bandgaps, thus the conversion of sunlight to electricity will be more efficient. For example, the P3HT:PCBM hardly absorbs >650 nm wavelength light, thus the energy of red and near infrared light in the solar spectrum is wasted. Fortunately, poly[2,6-(4,4-bis-(2-ethylhexyl)-4H-cyclopenta[2,1-b;3,4-b']dithiophene)-alt-4,7-(2,1,3-benzothiadiazole)] (PCPDTBT):PCBM system has smaller bandgap, and the onset of this active material is >900 nm. Hence, an effective double-junction tandem system will be formed if the large bandgap P3HT:PCBM OSC is stacked on small bandgap PCPDTBT:PCBM OSC (Figure 2.3d). An efficient recombination layer which consists of a layer of high work function material and a layer of low work function materials is required between the two active materials^[116]. The high work function layer collects the holes from one active layer, and the low work function layer collects the electrons from the other active layer, so the two solar cells are connected in series. The recombination layer also must be transparent for the effective light absorption of the second solar cell. In this example, PEDOT:PSS/TiO₂ works as the recombination layer between P3HT:PCBM and PCPDTBT:PCBM. The efficiency of the tandem OSC was 6.5%, which was significantly higher than single junction P3HT:PCBM OSC (4.7%) or the single junction PCPDTBT:PCBM OSC (3.0%). Such result proves that building up tandem architecture is an effective approach to improving the PCE of solar cells. After 10 years development, the PCE of the state-of-the-art 2-terminal double-junction OSC has reached 13% in 2017^[65].

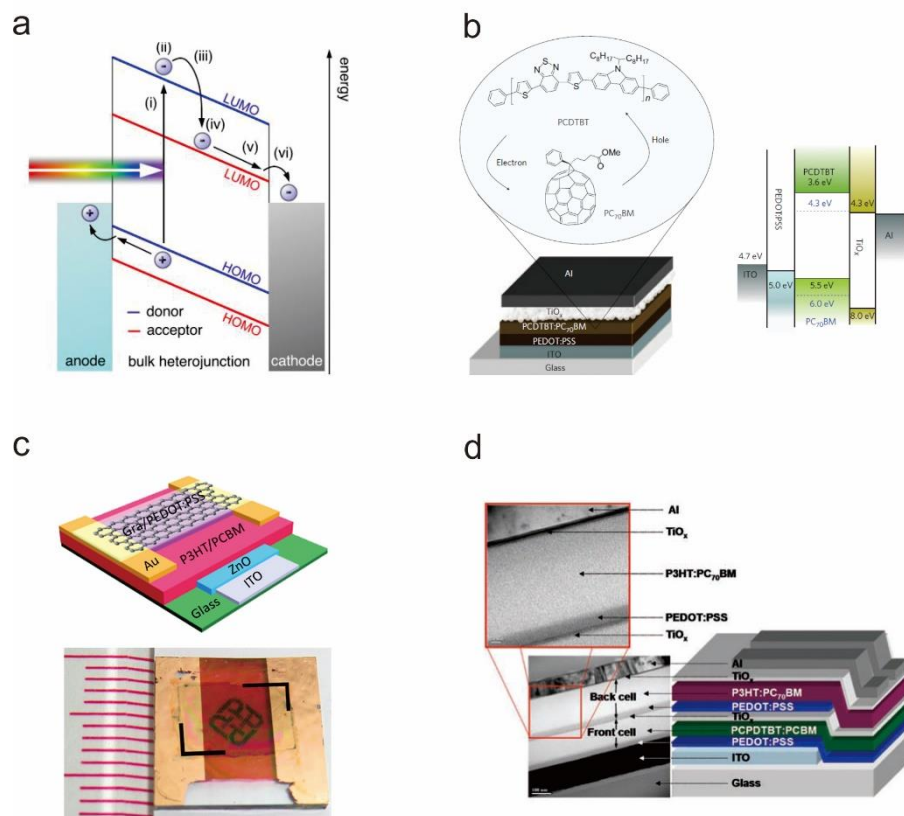


Figure 2.3 Mechanism and applications of BHJ OSCs. (a) Charge separation mechanism of BHJ OSCs^[117]. (b) Structure and energy diagram of a PCDTBT:PC₇₁BM based BHJ OSC^[118]. (c) Structure and optical image of a semitransparent OSC^[119]. (d) Structure and SEM cross-sectional image of a 2-terminal double-junction tandem OSC^[43].

2.1.3 Solar Cells with perovskite Absorbers

Perovskite materials are well known for their ferroelectric properties a long time ago^[120]. Perovskites refer to a category of chemicals with a general formula of ABX₃, which is same as CaTiO₃, and the crystal structure of CaTiO₃ belongs to orthorhombic crystal system at room temperature. For photovoltaic applications, a typical perovskite material is CH₃NH₃PbI₃ (Figure 2.4a). The CH₃NH₃PbI₃ crystal shows tetragonal structure under room temperature, and the crystal will transform to cubic structure when the temperature is above 330 K^[121]. An optical image of a CH₃NH₃PbI₃ single crystal is demonstrated in Figure 2.4b. The typical crystal habit of a body centered tetragonal lattice was observed, which was in agreement with the

space group I4/mcm. However, such single crystal $\text{CH}_3\text{NH}_3\text{PbI}_3$ is not suitable for photovoltaic application because the thickness of the crystal is significantly higher than the charge-carrier diffusion length of the material. In a typical PSC, the thickness of the perovskite film ranges from hundreds of nanometers to several micrometers^[101, 122].

Organolead halide perovskites are promising photovoltaic materials because of their excellent optical and electrical properties. One important parameter for photovoltaic materials is the absorption coefficient, which reveals the light absorption ability of the material at certain wavelength. The traditional Si and GaAs absorbers exhibit very high absorption coefficient over near-UV spectrum, but relatively poor absorption coefficient for visible light (400 ~ 800 nm). On the contrary, the perovskite materials ($\text{CH}_3\text{NH}_3\text{PbI}_3$ and $\text{CH}_3\text{NH}_3\text{PbI}_{3-x}\text{Cl}_x$ in Figure 2.4c) make use of the visible light very efficiently. Considering that the higher spectral irradiance of sunlight appears in the visible range, such material is especially compatible with the target of efficient solar energy conversion.

Another important parameter for photovoltaic materials is the charge-carrier diffusion length. A disadvantage of organic absorbers is the low charge-carrier diffusion length, which is less than 20 nm for most of the organic semiconductors^[79, 123]. Such disadvantage results in the low J_{SC} , which further limits the PCE of the OSCs. Organolead halide perovskites have much longer charge-carrier diffusion length/lifetime comparing with organic semiconductors. The diffusion length of $\text{CH}_3\text{NH}_3\text{PbI}_3$ can be hundreds of nanometers to several micrometers, and even $>175 \mu\text{m}$ for a single crystal^[19, 124, 125]. A recent research observed the photon recycling behavior of organolead halide perovskite, which is beneficial for the long charge-carrier lifetime and high V_{OC} of PSCs^[126]. The charge-carrier lifetime of perovskites is reflected by the time-resolved photoluminescence (PL). An ultralong lifetime $\tau_e = 272.7 \text{ ns}$ is observed on $\text{CH}_3\text{NH}_3\text{PbI}_{3-x}\text{Cl}_x$ as illustrated in Figure 2.4d. Such high charge-carrier lifetime is important for high performance solar cells.

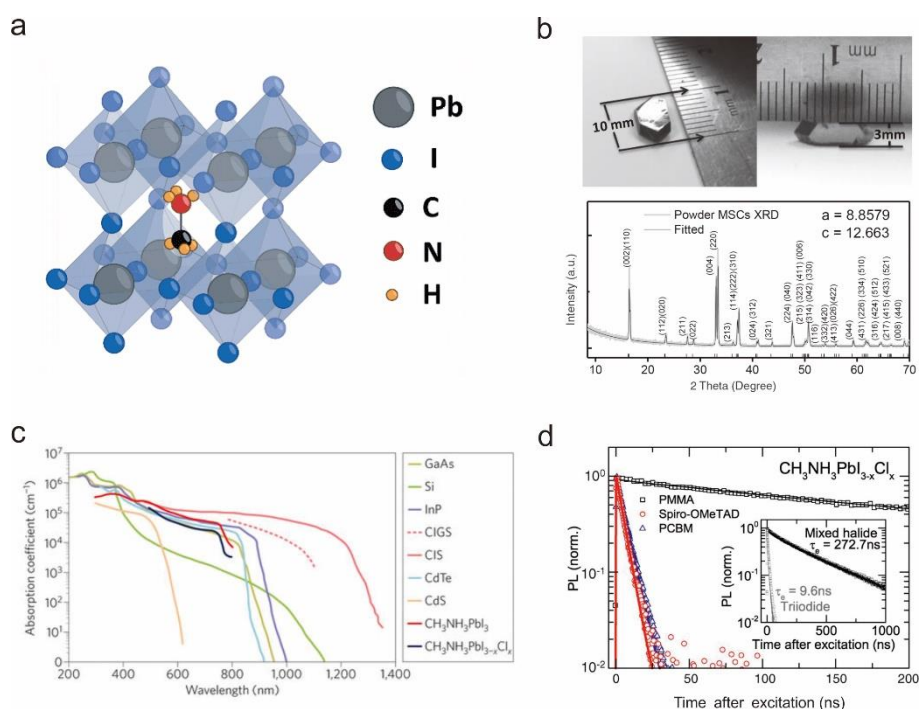


Figure 2.4 Chemical structure and physic properties of organolead halide perovskites. (a) Chemical structure of $\text{CH}_3\text{NH}_3\text{PbI}_3$ ^[127]. (b) Optical image (top) and XRD pattern (bottom) of $\text{CH}_3\text{NH}_3\text{PbI}_3$ single crystal^[124]. (c) Absorption coefficient of several photovoltaic active materials over near-UV to near-IR spectrum^[128]. (d) Time-resolved photoluminescence spectrum of $\text{CH}_3\text{NH}_3\text{PbI}_{3-x}\text{Cl}_x$ ^[19].

In recent years, many other perovskite materials are studied for photovoltaic applications apart from $\text{CH}_3\text{NH}_3\text{PbI}_3$ and $\text{CH}_3\text{NH}_3\text{PbI}_{3-x}\text{Cl}_x$, which are firstly applied in solar cells. In theory, stable perovskite can be formed with a tolerance factor t between 0.8 and 1, and an octahedral factor μ between 0.414 and 0.592 is required for the formation of $[\text{BI}_6]$ octahedra^[129]. However, most of the perovskite materials are not suitable for photovoltaic applications because of too large bandgap. The right diagram of Figure 2.5a listed some organolead iodide perovskite that are used for solar cells. Generally, in an ABX_3 perovskite active material, A is MA^+ , FA^+ , Cs^+ or their mixture, B is Pb^{2+} , Sn^{2+} or their mixture, and X is halide or pseudo-halide such as Cl^- , Br^- , I^- , SCN^- or their mixture. Figure 2.5b demonstrates some mixed perovskite materials for solar cells. Highly efficient PSC was reported by applying

(FAPbI₃)_{1-x}(MAPbBr₃)_x as the absorber, and the optimized device is obtained when $x = 0.15$, yielding high performance PSC with a 17.9% certified PCE^[71]. Although highly efficient mixed perovskite-based PSC with a PCE >22% has been reported, the stability problem of the PSCs remains to be unsolved. Multiple studies have proved that the inorganic-organic hybrid perovskites not only show poor thermal stability, but also decompose once exposed to moisture^[130]. On the contrary, inorganic perovskites such as CsPbI₃ show good durability. The problem is that it requires high temperature to convert CsPbI₃ from large bandgap orthorhombic (δ) phase to small bandgap tetragonal (α) phase. Figure 2.5d demonstrates α -CsPbI₃ quantum dots synthesized under room temperature. The bandgap of the quantum dots is tunable by adjusting the size of the quantum dots^[131].

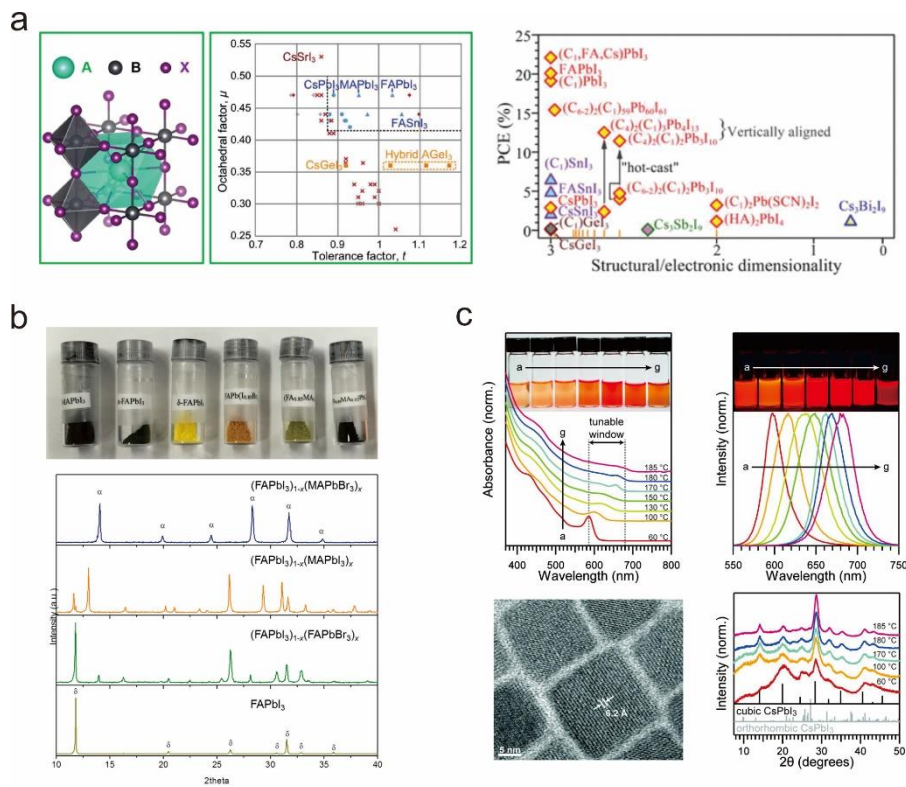


Figure 2.5 Perovskite materials for photovoltaic applications. (a) Several possible ABI₃ perovskites, and highest experimental PCE of ABI₃ perovskite-based PSCs^[129]. (b) Optical images of some mixed perovskites and their XRD patterns^[71]. (c) UV-visible absorption spectra, PL spectra, TEM image and XRD patterns of CsPbI₃ quantum dots^[131].

Besides, recent research revealed that the stability of PSCs can be improved significantly by inserting 2D perovskites in the 3D structure of perovskite active material^[132]. By improving the crystallinity of the 2D perovskite, 12.52% PCE PSC was obtained with very good stability under 65% humidity^[133].

2.2 Solution-processed OSCs and PSCs

One advantage of the organic and perovskite active materials is that these materials can be processed by multiple solution-based technologies. However, the rest functional layers especially the electrodes lack of effective solution processing technologies. The following section discusses the existed solution processing methods for each functional layer of OSCs and PSCs.

Figure 2.6a demonstrates a 100 m long solar foils fabricated by a R2R process. The solar foils consisted of 126,000 individual solar cells, owning a total active area of 88 m². The maximum power output of the solar foil was 1336 W, and the corresponding PCE of the device was 1.53%. The fabrication of such a large solar foil is completely free from high temperature or vacuum processes. To realize fully R2R strategy, flexographic-printed Ag grids and screen-printed PEDOT:PSS were adopted as front electrodes. A layer of slot-die coated ZnO served as the ETL, and the P3HT:PCBM active layer was coated by the same method. The top electrode was fabricated by screen-printing of Ag paste. The solar cells were fabricated on flexible PET substrate so that they can be rolled-up, and spread on target surfaces (Figure 2.6c and d)^[134]. Figure 2.6e is an example for a complete R2R process. The coating speed for ZnO, P3HT:PCBM and PEDOT:PSS was 54 m/h, 24 m/h and 12 m/h, respectively^[135]. Such processing speed is significantly higher than a traditional vacuum deposition process, which takes hours for wafer scale fabrication.

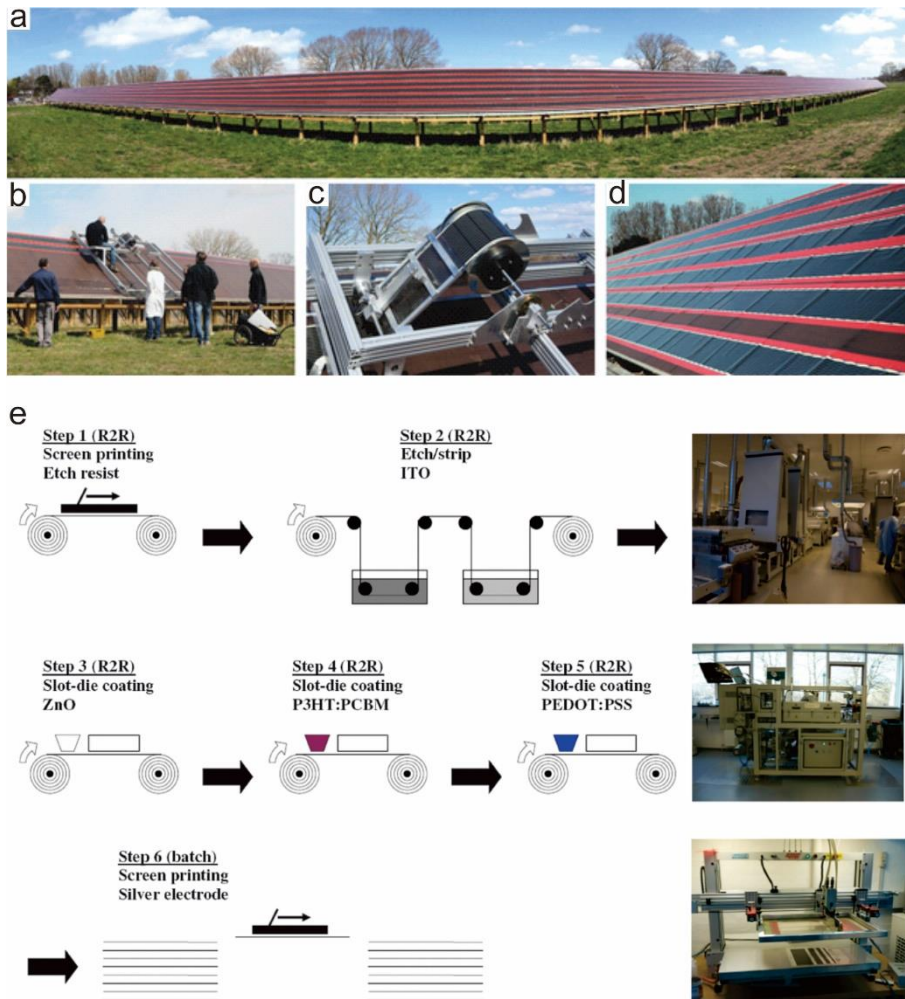


Figure 2.6 Schematics of R2R processed organic solar modules. (a) to (d) Optical images of a 100 m organic solar foil^[134]. (e) Schematic illustration of a R2R process for the fabrication of organic solar modules^[135].

2.2.1 Solution Process for Active Materials

There is not much diversity of the solution processes for BHJ OSC active materials. Spin-coating is the common method for devices on smaller substrates ($< 5 \times 5 \text{ cm}^2$), while slot-die coating is used for the fabrication of larger modules. Figure 2.7a illustrates the different stages of a spin-coating process. Spin-coating is a process to deposit a thin film on flat substrate by the aid of centrifugal force. The thickness of the film is determined by the accelerated speed and the angular speed of spinning, the viscosity of the solution, the volatility of the solvent, etc. For BHJ OSCs, the most frequently-used solvent is chlorobenzene (CB), because it has good solubility to most of

the polymer donors and fullerene acceptors. The high volatility of CB is also beneficial for the formation of smooth and uniform thin films.

However, spin-coating is not suitable for the fabrication of large area films. Instead of a continuous film that covers the entire substrate, the active material is required to be patterned as strips for solar modules. Slot-die coating is a non-contact solution process that can be used to deposit thin films with uniform thickness. The solution is pressed out of the slot coating die with controlled flow rate, and the coating speed is determined by the rotational speed of the roller (Figure 2.7b). The evaporation speed of the solvent can be accelerated by applying heat during coating. Comparing with screen printing and doctor-blading, slot-die coating is more ideal for the deposition thinner films with submicron scale to nanoscale thickness, and thus is suitable for the deposition of organic active material, ETL/HTL or PEDOT:PSS electrodes for OSCs or organic light-emitting diodes (OLEDs)^[45, 136].

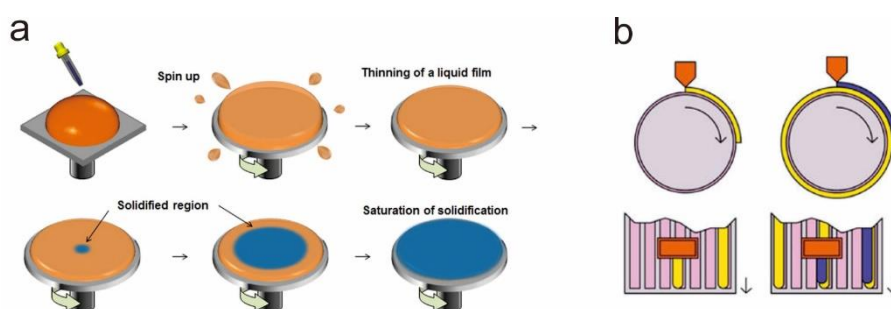


Figure 2.7 Solution methods for organic active materials. (a) Illustration of distinct stages during spin-coating^[137]. (b) Illustration of slot-die coating process for the fabrication of OLED modules^[45].

The situation is more complicated for perovskite active materials. The crystallization process of the perovskite layer is very important for high performance PSCs, so the deposition condition for perovskite layer should be controlled carefully. Figure 2.8 lists several solution/liquid-based methods for perovskite film deposition. The simplest way is the one-step spin-coating of the perovskite precursor solution (Figure 2.8a). However, this method doesn't work on most of the perovskite precursors, because the high boiling-point solvents dimethylformamide (DMF) or dimethyl sulfoxide (DMSO)

evaporate slowly during the annealing process, which induces discontinuous island-like perovskite crystallization^[138]. To achieve uniform perovskite film, the perovskite precursor consists of CH₃NH₃I and PbCl₂ with the molar ratio of 3:1 in DMF^[100]. Such method is simple and highly repeatable, but requires quite long post-annealing time (~ 1h) and low surface roughness of the substrate.

It has been found that the formation of a uniform PbI₂ film is much easier than CH₃NH₃PbI₃ film. Thus, two-step *in situ* reaction process is developed to deposit perovskite active materials. Figure 2.8b and c show two kinds of two-step methods. Firstly, a layer of PbI₂ was deposited by spin-coating, followed by a short post-annealing step to partly remove the residual solvent. For a dipping method, the entire substrate was dipped in a dilute solution of CH₃NH₃I (~ 10 mg/mL) for 2 min. For an inter-diffusion method, a CH₃NH₃I solution with higher concentration (~ 75 mg/mL) was spin-coated on PbI₂, followed by post-annealing at 100 °C to complete the reaction. The inter-diffusion method provides perovskite film with larger grain size, which usually yields higher solar cell PCE.

In 2014, Xiao et al. found that the crystallization of perovskite film can be accelerated when dropping anti-solvent on perovskite film during spin-coating^[139]. The anti-solvent should be poor solvent of the perovskite material, and it should have high volatility to accelerate the evaporation of the solvent. Such anti-solvent can be CB, diethyl ether or toluene, depending on the component of the perovskite solution (Figure 2.8d)^[140]. Since the anti-solvent dripping method is versatile for perovskites with different components, it has been widely accepted for small size PSC fabrication.

As mentioned above, spin-coating is not satisfactory for large scale fabrication. Fortunately, the thickness of perovskite films can be thicker than the organic semiconductors due to the longer diffusion length. Thus, the formation of perovskite active layer is compatible with multiple coating or printing techniques. Figure 2.8e shows the doctor-blading process for the

deposition of large area perovskite films. The perovskite precursor solution was dropped at the edge of the ITO/glass substrate, then the glass blade swiped the precursor solution over the substrate at 125 °C to form perovskite film. The thickness of the perovskite film ranged from 600 nm to 5.6 μm, and the optimum thickness was found to be 3.1 μm. The perovskite film maintained good uniformity over large area, which is promising for the fabrication of PSC modules. Slot-die coating works well for OSC fabrication, and it is also proved to be applicable on PSC recently (Figure 2.8f). However, the perovskite film quality is not satisfactory as the crystallization of perovskite film requires well controlled environment. The slot-die coating of perovskite film needs to be optimized in the future.

Chen et al. reported a solvent- and vacuum-free “pressure processing” method to deposit large area perovskite films (Figure 2.8g). In fact, it is not a kind of “solution” method because the liquid phase perovskite precursor is adopted rather than a solution precursor. The liquid precursor consisted of 1:1 molar ratio $\text{CH}_3\text{NH}_3\text{I}\cdot 3\text{CH}_3\text{NH}_2$ and $\text{PbI}_2\cdot\text{CH}_3\text{NH}_2$. The perovskite film was formed by applying pressure to the precursor, and this process was realized by the squeezing system shown in Figure 2.8g. This route is convenient for the fabrication of PSC modules, as the pressure processed perovskite film was uniform over the entire substrate. 12.1% PCE PSC module with an active area of 36.1 cm² was obtained by this approach. This result is comparable to the best spin-coating based PSC with a small active area of 1 cm².

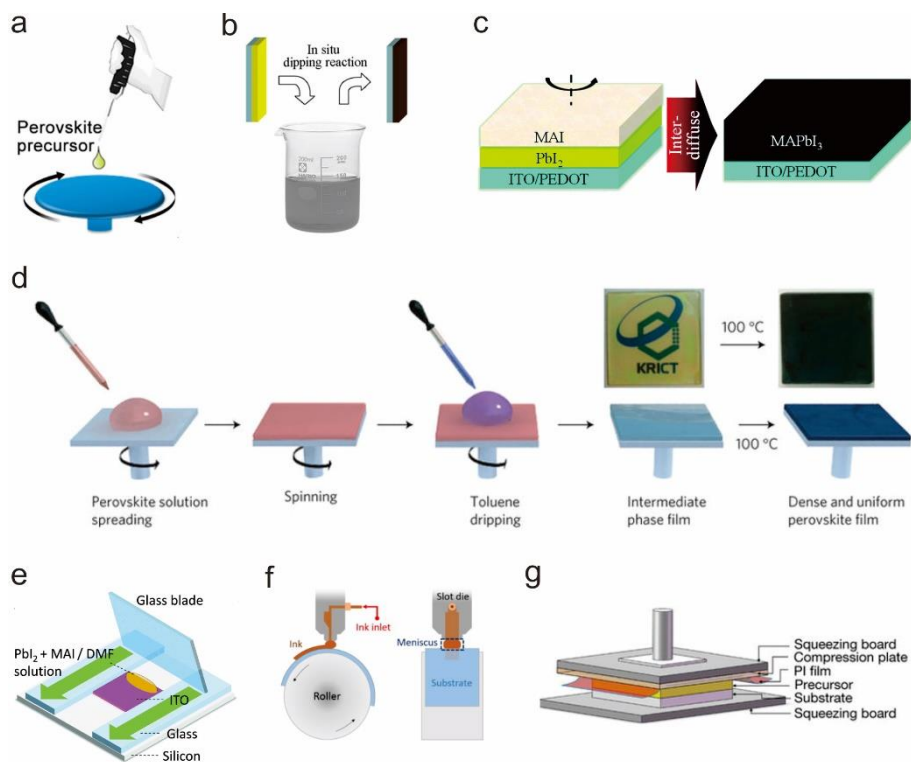


Figure 2.8 Perovskite active materials processed by different methods in liquid phase. (a) One-step spin-coating^[1], (b) two-step dipping^[141], (c) two-step “inter-diffusion”^[142], (d) one-step anti-solvent dripping^[143], (e) doctor-blading^[122], (f) slot-die coating^[144], and (g) pressure processing method^[145].

2.2.2 Solution Process for Electrodes

Conventional OSC and PSC adopt ITO transparent electrode and metal back electrode. The ITO film is deposited by sputtering, while the metal electrode is deposited by thermal evaporation. Efforts have been put on solution processed transparent electrodes and back electrodes to improve the fabrication throughput and to lower the manufacturing cost. Till now, the most successful solution processable transparent electrode is PEDOT:PSS based electrode, and the best solution processable back electrode is the Ag electrode based on printable Ag nanoparticle (AgNP) ink/paste.

PEDOT:PSS has been studied as HTL and transparent electrode in OSCs for over 20 years^[146]. Multiple PEDOT:PSS solutions are commercially available for different applications. For example, PH 1000 is a highly conductive type

for electrode applications, while PVP AI 4083 is a high work function type that can be used as hole transport material in solar cells^[147]. However, the conductivity of pristine PH 1000 (~ 1 S/cm) is far less than that of ITO ($\sim 10^4$ S/cm), thus is not eligible for electrode application. As a result, improving the conductivity of PDEOT:PSS is of great interests.

Multiple studies have proved that doping and post-treatment of PDEOT:PSS is effective for the improvement of conductivity. DMSO and ethyl glycol (EG) are the most commonly used additives in PEDOT:PSS solution^[148]. The conductivity of PEDOT:PSS film can be improved by 2 to 3 degrees of magnitude if such additive is doped in the PEDOT:PSS solution before spin-coating. Figure 2.9a illustrates an OSC that employs EG-doped and solvent post-treated PEDOT:PSS as transparent electrode. The conductivity of the PDEOT:PSS was as high as 1418 S/cm after the treatment. Beside the solvent post-treatment, DMSO, methanol, formic acid, sulfuric acid, etc. are reported for the efficient post treatment of PEDOT:PSS film^[149-151]. The best reported sulfuric acid-annealed PEDOT:PSS film reached a conductivity $>4,000$ S/cm, which is comparable with that of an ITO film^[152].

Another approach to improving PEDOT:PSS conductivity is applying highly conductive metal grid/mesh as current collector. The width and spacing of the metal grid line should be optimized carefully to provide good conductivity while maintaining high optical transmittance. A TCO-free OSC with honeycomb-structure Ag current collecting grid is illustrated in Figure 2.9b. The Ag grid was fabricated by screen-printing of AgNP ink. Whereas the Ag grid showed very low sheet resistance ($1 \Omega/\square$), the solar cell efficiency was not high due to the rough surface of the printed Ag grid.

Figure 2.9c demonstrates a semitransparent PSC (st-PSC) with embedded Ni mesh/PEDOT:PSS top electrode. The Ni mesh was laminated on top of the PSC, and the PEDOT:PSS/transparent conductive adhesive (TCA) served as the binder and electrode. Both the embedded Ni mesh and the TCA are commercially available. The lamination process avoids the direct coating of

PDEOT:PSS solution above perovskite layer, which may degrade the perovskite material. The st-PSC showed 13.3% high PCE when illuminated from the FTO side, but only 9.8% efficiency when illuminated from the Ni mesh/PEDOT:PSS/TCA side. This is mainly due to the light absorption of spiro-OMeTAD HTL.

Apart from PEDOT:PSS, other materials have been studied as the substitutes for TCOs. Figure 2.9d is an example of using Ag nanowires (AgNWs) as the transparent electrode. AgNWs are highly conductive, and they can be dispersed in water or organic solvents. However, previously reported AgNW films are always highly rough, thus are not suitable for bottom electrode application^[153]. In this work, AgNW was spin-coated on PET substrate, and a cold isostatic pressing method was adopted to form effective electrical junctions. The flexible OSC on PET substrate showed 8.56% high PCE, which is comparable with a rigid device on glass substrate.

The solution processing of metal back electrode is of great challenge because the applicable solvents are limited. On the one hand, the metal NP/precursor should be soluble in the solvent, and the viscosity of the solution should be appropriate for printing. On the other hand, the solvent should be poor solvent to the underneath layers of the solar cell. Whereas multiple metals can be deposited by thermal evaporation for solar cells, few of them are compatible with solution process.

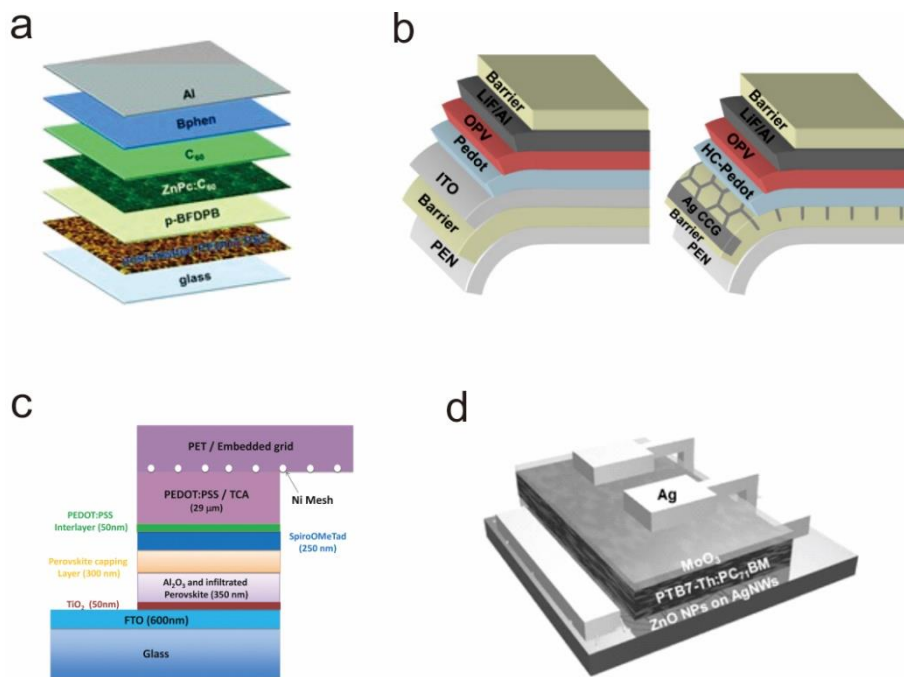


Figure 2.9 Solution processed transparent electrodes for OSCs and PSCs. (a) Highly conductive PEDOT:PSS (hc-PEDOT:PSS) based OSC. The conductivity of the PEDOT:PSS is improved by solvent post-treatment^[40]. (b) Highly efficient flexible OSC based on printed Ag current collecting grids and hc-PEDOT:PSS electrode^[154]. (c) st-PSC based on embedded Ni mesh and PEDOT:PSS electrode^[155]. (d) ITO-free OSC based on AgNW electrode^[156].

One approach to depositing metal through solution process is direct printing of metal NP ink/paste. AgNP is the most commonly adopted metal NP for printing, because it is easy to synthesize, and the cost of it is moderate. Figure 2.10a lists 4 different printed Ag top electrodes for OSC modules. The result indicates that flatbed screen-printing and rotary screen-printing are suitable for device fabrication, while flexographic-printing and inkjet-printing are not satisfactory. The lower viscosity of the ink for flexographic-printing and inkjet-printing causes non-uniform surface coverage problem, which leads to poor solar cell performance.

Another approach is the *in situ* deposition of metal thin film by solution process. Whereas electrodeposition is a widely used solution deposition

technique, it requires a conductive substrate. Since the glass or polymeric substrate for solar cells is non-conductive, electroless solution deposition method is preferred. Polymer-assisted metal deposition (PAMD) is a recently developed electroless deposition technique for metal thin films^[51]. It employs functional polymers to absorb reactive metal ions, and then the metal ions are chemically reduced to metal. The PAMD method is compatible with multiple solution coating and printing techniques such as spin-coating, screen-printing, inkjet-printing and soft lithography molding^[157]. The deposited metal thin film shows much better adhesion to substrate and mechanical durability comparing with vacuum-deposited metal thin film, because the functional polymer also serves as an adhesive layer as well as a mechanical buffer layer. Figure 2.10b demonstrates the fabrication process for a full-solution-processed OSC based on PAMD Cu bottom electrode. The OSC was constructed with an inverted configuration that the Cu back electrode was deposited at the bottom of the OSC. Thus, the PAMD solution would not damage the other functional materials of the OSC. The full-solution-processed OSC showed 2.7% PCE, which was the highest among all the full-solution-processed OSCs with the same active material. More importantly, the OSC exhibited excellent mechanical durability that 80% of its initial PCE was maintained after 1,000 cycles of repeated bending at a radius of 6.5 mm.

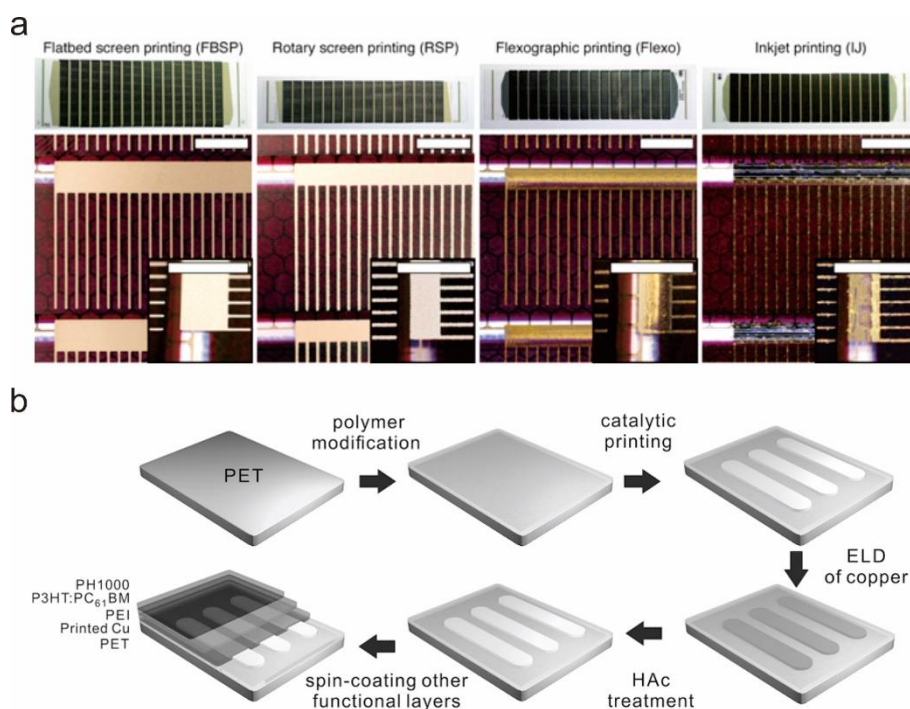


Figure 2.10 Solution processed metal back electrodes. (a) Comparison of flatbed screen-printed, rotary screen-printed, flexographic-printed, and inkjet-printed Ag back electrodes for flexible OSC modules^[158]. (b) Fully solution-processed flexible OSC based on Cu bottom electrode. The Cu electrode is deposited by PAMD^[159].

2.3 Flexible OSCs and PSCs

The potent flexibility is one of the most important advantages of OSCs and PSCs. Whereas the fabrication of OSCs and PSCs on rigid substrates is relatively mature, transferring OSCs and PSCs to flexible polymeric substrates is not a straightforward process. First, the application of mechanically brittle materials is limited for flexible solar cells. Second, high temperature processes should be avoided since the polymeric substrate will deform or decompose under such condition. For example, the FTO electrode which is commonly used as transparent electrode for PSCs is not applicable on flexible substrate because it requires 400 °C to obtain high quality FTO film during deposition^[160]. The similar problem also occurs on other TCOs

such as ITO: the conductivity of ITO/PET is always inferior to that of ITO/glass, whereas ITO is processable at lower temperature.

2.3.1 TCO-based Flexible OSCs and PSCs

Most of the reported flexible OSCs and PSCs are constructed on ITO/PET substrate. Such flexible solar cells always exhibit significantly lower efficiency comparing with rigid solar cells on ITO/glass majorly due to the poor conductivity and film smoothness of ITO/PET. What's worse, the ITO film on PET substrate shows very poor mechanical durability because of the brittle nature of ITO. As shown in Figure 2.11a, cracks were observed on the surface of ITO after repeated bending, and such crack led to a dramatic decrease of film conductivity.

To solve the conductivity and mechanical durability issues, researchers designed ITO/AgNW/ITO sandwiched electrode (Figure 2.11b). The embedded AgNW decreased the sheet resistance of the electrode to $11.58 \Omega/\square$, which is comparable to ITO/glass electrode. More importantly, the sandwiched electrode showed high mechanical robustness that the resistance remains almost unchanged after 8,000 cycles of dynamic outer bending test. Thanks to the better conductivity and mechanical durability of the ITO/AgNW/ITO electrode, the PCE of the OSC was improved for ~10% comparing with a control device using ITO/PET electrode.

Another challenge for flexible PSCs comes from the low temperature fabrication of ETL and HTL. The TiO_2 ETL which is widely used in normal-structured PSCs usually requires a 500 °C sintering process to improve the crystallinity. You et al. reported inverted flexible PSC using PEDOT:PSS as HTL and PCBM as ETL to address the high temperature issue^[21]. However, the application of PEDOT:PSS HTL in PSCs led to low V_{OC} , thus the solar cell efficiency is very limited. NiO_x is an ideal hole transport material for flexible PSCs because it can be deposited by low temperature solution process, and its valence band is perfectly aligned with perovskite active materials.

Figure 2.11c demonstrates a flexible PSC with the structure of ITO/NiO_x/CH₃NH₃PbI₃/C₆₀/Bis-C₆₀/Ag. The NiO_x film was deposited by spin-coating of a NiO_x nanocrystal solution at room temperature. The best flexible PSC showed 14.53% PCE, which was high than a rigid control device with PEDOT:PSS HTL. Besides, some organic hole transport materials with suitable HOMO energy level are studied as HTL for PSCs. For example, 1,4-bis(4-sulfonato-butoxy)benzene and thiophene moieties (PhNa-1T) was reported as high performance HTL for flexible PSCs by Jo et al (Figure 2.11d). The champion device showed a PCE of 14.7%, which was 75% higher than that of a PDEOT:PSS based control device. Poly[bis(4-phenyl)(2,4,6-trimethylphenyl)amine (PTAA) is another high performance HTL that is reported for highly efficient normal structure PSCs^[143]. Recently, it is also reported as HTL for high performance inverted PSCs^[161]. Figure 2.11e illustrates a flexible PSC with a structure of ITO/PTAA/perovskite/PCBM/bathocuproine (BCP)/Cu. By tailoring the perovskite component and other conditions, the optimized device reached a record-breaking PCE of 18.1%. Considering that a commercialized flexible OSC module only showed ~4% PCE, the flexible PSCs are promising for daily applications in the future.

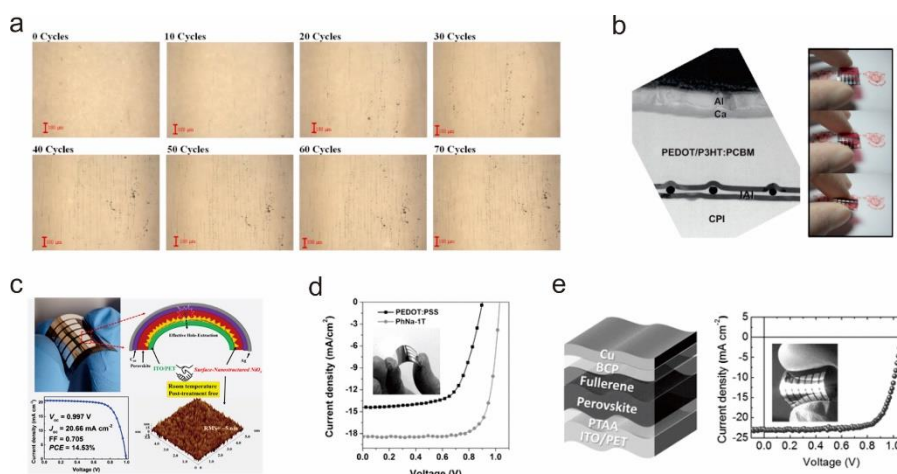


Figure 2.11 Mechanics and design for TCO-based OSCs and PSCs. (a) Bending fatigue of ITO on PET substrate^[29]. (b) Flexible OSC based on ITO/AgNW/ITO electrode^[162]. (c) Flexible PSC based on low temperature processed NiO_x HTL^[163]. (d) Comparison of flexible PSCs with PEDOT:PSS and PhNa-1T HTLs^[164]. (e) Highly efficient flexible PSC using PTAA as HTL^[22].

2.3.2 TCO-free Flexible OSCs and PSCs

For highly flexible OSCs and PSCs, the use of brittle TCOs should be avoided. In Chapter 2.2.2, solution-processed transparent electrode for OSCs and PSCs is reviewed. Comparing with vacuum-deposited TCOs, solution-processable transparent electrodes show good compatibility with R2R process, which is ideal for the fabrication of flexible OSC and PSC modules. Figure 2.2.2a demonstrates a TCO-free tandem OSC module fabricated by R2R process. The transparent electrode is a hybrid electrode of Ag current collecting grids and PEDOT:PSS, which has been introduced in previous sections. The R2R processed OSC modules show flat outlines on 130 μm -thick PET substrates, but buckled outlines on thinner (40 and 60 μm -thick) PET substrates. In other word, thicker polymeric substrates are preferred for R2R process from the manufacturing point of view. However, the increase of substrate thickness will sacrifice the flexibility of the entire device.

It is easier to apply thin substrates for small area fabrication. Figure 2.12b shows a flexible PSC fabricated on photopolymer NOA63. The NOA63 photopolymer was firstly spin-coated on flat Si wafer to ensure a smooth surface of the substrate. After the deposition of thin Au electrode, the NOA63 was peeled-off from the Si wafer. The thin (30 nm-thick) Au electrode was highly conductive, and the mechanical flexibility of Au film was better than that of ITO film. However, the optical transmittance of the Au electrode was significantly worse than that of ITO, resulting in low PCE when illuminated from the bottom side. The flexibility of PSC can also be improved by using thinner PET substrate. As illustrated in Figure 2.12c, inverted PSC was fabricated on a 57 μm -thick PET substrate, on which a thin layer of UV-resin was coated. The highly conductive embedded Ag mesh/PEDOT:PSS electrode ensured 14% high PCE, which was higher than that of an ITO based control PSC. More importantly, the mechanical flexibility of the PSC was so good that the PSC showed > 90% retention after 10,000 bending cycles at a radius of 5 mm.

The TCO-free OSCs and PSCs can even be designed for stretchable applications when using thinner substrates. Although the PET substrate and each layer of the solar cell are not intrinsically stretchable, the entire device can be stretchable by the “wavy” strategy^[16, 165]. This is because that the OSC and PSC can follow the motion of arbitrary curved surface once attached on it, if the substrate of the solar cell is thin enough. Thus, a stretchable solar cell is realized once attaching the ultrathin solar cell on a pre-stretched elastomer. Figure 2.12d demonstrates an ultrathin OSC fabricated on 1.4 μm -thick PET substrate. The stretchable OSC was achieved when attaching the OSC on a 100% pre-stretched 3M VHB 4905 elastomer. Buckles will be formed on the surface of elastomer once the strain is released. Since the buckles have micrometer scale radii, it is impossible to use TCOs as transparent electrode. Hence, the OSC adopted PEDOT:PSS as bottom transparent electrode. The compressed OSC can be recovered to its original length if the elastomer is stretched. However, the retention of the stretchable OSC was not very satisfactory: the PCE of the OSC decreased for $\sim 30\%$ after 22 cycles of stretch-compress cycles. In addition, the initial PCE of the OSC was only $\sim 4\%$ due to the limitation of the P3HT:PCBM active material. In 2015, stretchable PSC was reported with the similar strategy (Figure 2.12e). The PSC also employed PEDOT:PSS as transparent electrode, and the substrate was 1.4 μm -thick PET. The major difference is that the ultrathin PSCs are attached on both uniaxial and biaxial pre-stretched elastomers. The PSC showed $> 12\%$ initial PCE thanks to the high-performance perovskite active material, and the PCE remained 70% after 100 cycles of stretch and compress. The decay of solar cell performance after bending/stretch-compress was due to the mechanical stress-induced cracks on the functional layers of the solar cell, especially on the vacuum-deposited metal back electrodes.

As a proof of concept, Lipomi et al. reported an intrinsically stretchable OSC in 2011 (Figure 2.12f). Pre-stretched PDMS elastomer was used as the substrate directly, and vacuum-deposited metal back electrode was replaced by liquid alloy droplet to avoid mechanical failure. The solar cell performance

was quite poor due to the absence of ETL and HTL, and the work function of the liquid alloy did not match with the P3HT:PCBM active material. This study proved that submicron scale buckling doesn't cause cracks on PEDOT:PSS film and P3HT:PCBM film.

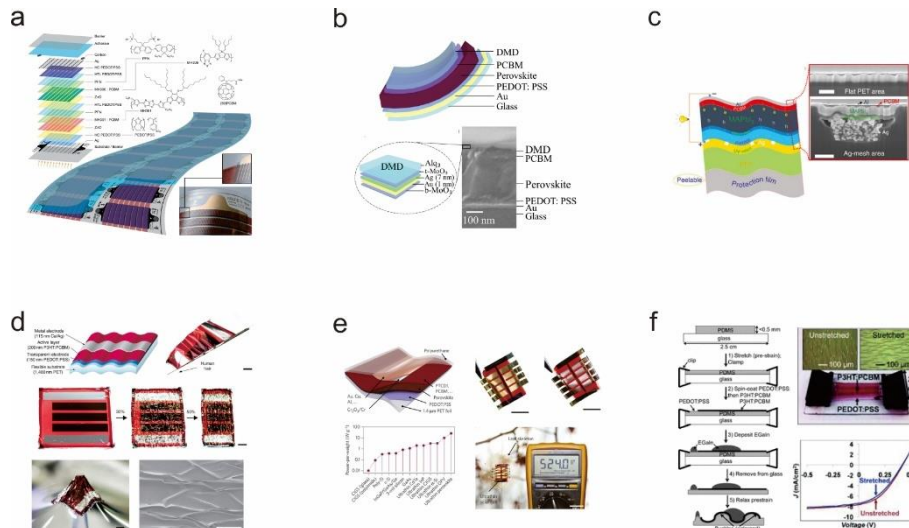


Figure 2.12 TCO-free flexible OSCs and PSCs. (a) R2R fabrication of TCO-free organic tandem solar cell module on PET substrate^[93]. (b) TCO-free semitransparent PSC on flexible NOA63 substrate^[166]. (c) TCO-free flexible PSC based on Ag mesh/PEDOT:PSS hybrid electrode^[167]. (d) TCO-free OSC on ultrathin PET substrate^[168]. (e) Ultrathin high power-per-weight PSC on 1.4 μm-thick PET substrate^[169]. (f) TCO-free stretchable OSC on PDMS substrate^[170].

2.4 Conclusions and Summary of Research Gaps

In conclusion, OSCs and PSCs are promising candidates for future low cost and highly efficient solar energy harvesting applications. Multiple organic and perovskite active materials have been developed for photovoltaic applications. Their bandgaps can be tuned by componential adjustment and chemical modification. As a result, they are versatile for tandem applications with dozens of solar cells. The OSCs and PSCs are intrinsically flexible, and they are compatible with low cost and scalable R2R process. However, there is a dilemma between mechanical flexibility and solar cell efficiency. On the

one hand, the TCO/vacuum-deposited metal electrodes based solar cells show satisfactory PCE, but relatively poor mechanical flexibility. On the other hand, the TCO-free or vacuum-free solar cells are highly flexible but low efficient. The fabrication of fully solution-processed OSCs and PSCs with good flexibility and high PCE remains to be challenging. The research gaps of the OSC and PSC fields are listed as follow:

1. The fabrication of highly efficient OSCs and PSCs require vacuum deposition technologies. Such technologies are not suitable for high throughput large area fabrication of solar modules. Although efforts have been put to integrate vacuum-free solution process into the fabrication processes, the study of fully solution-processed OSCs and PSCs is almost blank.

2. Highly efficient OSCs and PSCs employ TCOs as transparent electrodes. The fabrication of highly conductive TCOs require high temperature thermal annealing, which is not compatible with flexible polymeric substrates. Whereas TCO-free OSCs and PSCs have attracted more and more research interests in recent years, the PCE of TCO-free OSCs and PSCs is still unsatisfactory. A facile vacuum-free and high temperature-free strategy that can be used to fabricate highly efficient TCO-free OSCs and PSCs is in need.

3. The PEDOT:PSS based OSCs and PSCs show potential applications for flexible electronics, but the poor conductivity of PEDOT:PSS limits its application for large area solar modules. Although compose electrode of metal grids and PEDOT:PSS partly solves the conductivity issue, the metal grids decrease the optical transmittance and increase the surface roughness, which may also lead to poor solar cell efficiency. Besides, it is hard to deposit PEDOT:PSS film atop the PSC because the perovskite active materials are sensitive to moisture. Developing highly conductive PEDOT:PSS electrodes that are versatile for PSCs is of necessity.

4. The printable metal electrodes show great potent for large scale R2R fabrication of OSCs and PSCs. However, the printed metal electrodes always show high surface roughness, which makes them not suitable for bottom electrode application. Besides, the printed metal electrodes lack of flexibility

because the poor adhesion to substrates. A solution process that can be used to fabricate high quality metal electrodes is demanded.

5. The flexible substrates are less transparent than rigid glass substrates. Moreover, the absorbers of OSCs and PSCs are always too thin for fully absorption of the transmitted light. Anti-reflection and light-trapping designs are preferred for flexible OSCs and PSCs. However, most of the existed anti-reflection and light-trapping strategies are not compatible with flexible substrates. There are few reports on enhancing the light absorption for OSCs and PSCs through light-trapping strategy.

CHAPTER 3. METHODOLOGY

The general methodology for this thesis is introduced in this chapter. The PAMD method that is used to prepare metal bottom electrodes for solar cells is illustrated. The one-step replica molding of rose petal for biomimetic haze film (BHF) is also introduced in this chapter. In addition, the equipment and methods that are used for the characterization of materials and devices is elaborated.

3.1 Materials Preparation

3.1.1 PAMD Fabrication of Bottom Electrodes

The PAMD method is used to fabricate bottom metal electrodes for flexible OSCs to overcome the problem of vacuum-deposited metal electrodes and printed metal electrodes based on metal nanoparticle inks. The key steps of a typical PAMD fabrication is demonstrated in Figure 3.1. First, the substrate is grafted with functional polymer such as poly[2-(methacryloyloxy)ethyl] trimethylammonium chloride (PMETAC). The functional polymer can be grafted on the substrate by free-radical polymerization, atom transfer radical polymerization (ATRP), or photo-induced crosslinking, depending on the substrate type and component of the polymer precursor. The functional polymer has very strong electrostatic interaction with PdCl_4^{2-} catalytic precursor. As a result, the catalytic precursor can be patterned on the polymer-modified substrate through ion exchange. Then, metal thin films are deposited on the selected areas by immersing the entire substrate in the metal plating bath. Typically, the plating bath consists of the complexed metal salt and the reductant. For example, the solution A of Cu plating bath contains copper sulfate, potassium sodium tartrate, and sodium hydroxide. The solution B of the plating bath is the reductant solution, which is usually diluted formaldehyde. The PdCl_4^{2-} is reduced to Pd nanoparticles by the reductant during plating, and then the Pd nanoparticles catalyze the reduction of Cu^{2+} . To serve as the bottom electrode for OSCs, the Cu film requires a post acid-treatment to remove the oxides that are formed during plating.

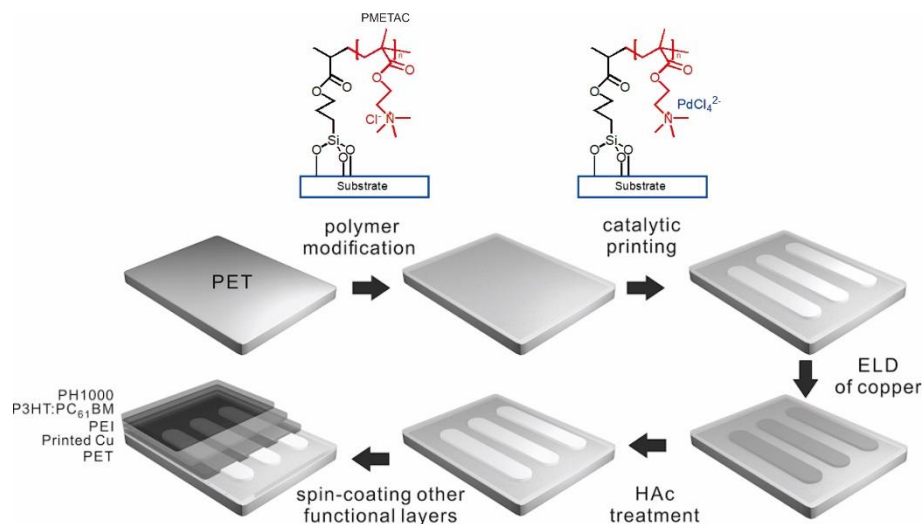


Figure 3.1 Schematics of a PAMD process for the fabrication of Cu bottom electrodes of flexible OSCs.

3.1.2 Replica Molding of Rose Petals for BHF

The BHF is obtained by the replication of the surface topography of rose petal using PDMS. First, PDMS is mixed with the crosslinking agent with the weight ratio of 10:1. The mixture is then casted on top of the rose petal, followed by a degassing process to remove the bubbles among the mixture liquid. The PDMS turns to a piece of solid elastomer after 48 h curing at room temperature. Although curing at higher temperature will accelerate the crosslinking process, it will also damage the surface structure of rose petal, which may lead to unsuccessful replication. Finally, the PDMS elastomer is peeled-off from the rose petal, and then attached on the transparent substrate of the solar cells.



Figure 3.2 Schematics of the fabrication process for BHF.

3.2 Characterization

3.2.1 Optical Microscopy

An optical microscope uses groups of lenses to magnify the optical image of the materials. The magnification of the optical microscope usually ranges from 50× to 2,000×, thus is used to obtain optical image of samples with microscale or larger structures.

3.2.2 Atomic Force Microscopy (AFM)

AFM is a type of high-resolution scanning probe microscope (SPM), which gathers the information of sample surface by probe-sample interaction. The tip is made by very sharp (nanoscale radius) silicon nitride to ensure precise detection, and it is fixed on one end of the cantilever. The Z-scanner controls the vertical motion of the cantilever, and the XY-scanner controls the horizontal motion of the sample. Once the tip approaches the surface of the sample, the tip and cantilever will be pulled by the sample due to the atomic attractive force. However, the repulsive force will increase dramatically when the tip becomes closer, and such force will push the tip and cantilever away. The deflection of the cantilever is recorded by the motion of the laser light spot on the photodetector as demonstrated in Figure 3.3. The laser is focused on the cantilever, and reflected to the position-sensitive photodetector. When the cantilever moves due to the tip-sample interaction, the position of the light spot is changed. As a result, the surface topography of the sample can be translated from the data recorded by the photodetector. Contact, non-contact and tapping are three modes for the topographical characterization. The tip directly contacts with the sample when operating with contact mode. Non-contact mode is used for those “soft” samples which may be damaged by the scratch of the tip. The photodetector records the vibration of the cantilever caused by the attractive force between tip and sample. Tapping mode is similar to non-contact mode, but with higher oscillation amplitude to avoid the contamination of tip by sample surface.

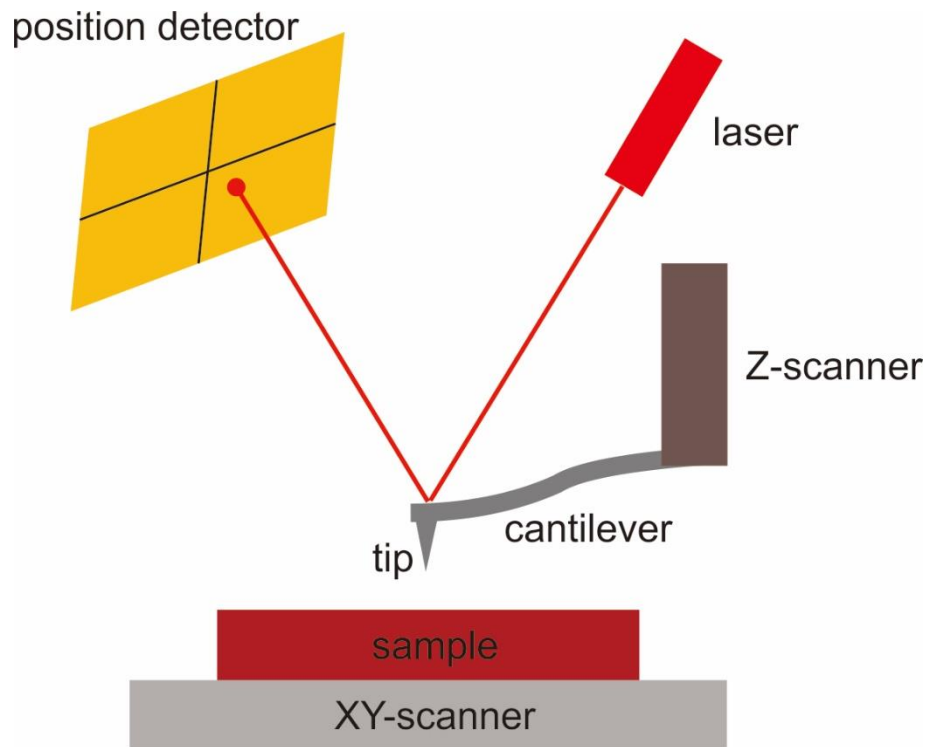


Figure 3.3 Illustration of the components and working mechanism of AFM.

3.2.3 Scanning Electron Microscopy (SEM)

Multiple interactions may happen when electrons hit atoms. SEM reveals the topography and composition of the samples by using accelerated electron beam to scan on the surface of the samples. Various signals such as secondary electrons, back-scattered electrons and characteristic X-rays can be generated under the irradiation of the electron beam, and then recorded by the SEM. Most of the SEMs are equipped with secondary electron detector. The secondary electrons are low energy electrons that are ejected from the K-shell of the sample atoms by the inelastic scattering interactions between the sample atoms and the injected electrons. The number of generated secondary electrons is closely related to the incident angle of electron beam, so the surface profile of the sample can be determined by counting the collected secondary electrons. The resolution of the image can be as small as 0.5 nm for a SEM equipped with secondary electron detector. Apart from topographical characterization, the SEM is capable to map the elemental distribution on the surface of samples by energy-dispersive X-ray

spectroscopy (EDX), since different elements exhibit different characteristic X-ray under electron beam irradiation. The characteristic X-ray is generated by the energy difference between the ejected electrons from inner shell and the filled-in electrons from the outer shell.

3.2.4 Raman Spectroscopy

Raman spectroscopy is widely used in chemistry to identify the specific structures of molecules by inelastic scattering of Raman scattering. The vibrational, rotational and other low-frequency modes are revealed under the excitation of monochromatic light, by observing the energy shift of the laser photons. Raman spectroscopy is a non-destructive and non-contact characterization method, and there is no need for sample preparation before characterization.

3.2.5 X-ray Photoelectron Spectroscopy (XPS) and Ultraviolet Photoelectron Spectroscopy (UPS)

XPS and UPS are photoemission spectroscopy (PES), which measures the emitted electrons from materials by photoelectric effect. XPS is a quantitative surface analysis technique for elemental identification. The chemical state and the valence band structure of the elements can also be characterized by XPS. When the surface of a material is irradiated by light such as X-ray beam, there will generate photoejected electrons, which is known as photoelectric effect. XPS reveals the chemical information of materials by analyzing the kinetic energy and the number of the ejected electrons. The binding energy of the ejected electrons $E_{binding}$ can be determined as:

$$E_{binding} = E_{photon} - (E_{kinetic} + \varphi) \quad (6)$$

where E_{photon} is the energy of the irradiated X-ray, $E_{kinetic}$ is the kinetic energy of the ejected electrons, and φ is the work function. XPS analysis is very sensitive that the detection limits are in the parts per thousand range. The mechanism of UPS is very similar to XPS, but using ultraviolet light as the irradiation source. The detection range of UPS is shorter than XPS, but with

more accuracy. UPS is usually used to determine the work function of materials.

3.2.6 Ultraviolet-Visible Spectroscopy (UV-Vis)

UV-Vis refers to the absorption or reflectance spectroscopy of the samples in UV-Vis range. UV-Vis is widely used in analytic chemistry to determine the concentration of solutions, the optical transmittance of materials, and characteristic transition metal ions or conjugated organic compounds. The UV-Vis spectrometer compares the intensity of the light passing through the reference and the light passing through the sample to calculate the transmittance of the sample.

3.2.7 Current-Voltage (*I-V*) Characterization of Solar Cells

The *I-V* curve of solar cells reflect the photovoltaic performance of solar cells under the irradiation of light, or the diode characteristics of solar cells under dark state. A solar simulator equipped with airmass 1.5 (AM 1.5) filter is commonly used as the standard light source for solar cell characterization, and the areal power rate of the simulated sunlight is 100 mW/cm^2 . The solar cells are connected to a sourcemeter to measure the *I-V* curves. The sourcemeter applies a swept bias either from negative to positive or a reversed scan on the solar cells, and the current that passes through the solar cells is recorded. The open-circuit voltage (V_{OC}) and short-circuit current (I_{SC}) of the solar cells can be observed directly on the *I-V* curves, and the short-circuit current density (J_{SC}) of the solar cells can be calculated by dividing the I_{SC} with the active area of the solar cells.

3.2.8 External Quantum Efficiency (EQE)

The quantum efficiency (QE) of solar cells refer to the ratio of converted electrons to incident photons. This ratio is defined as EQE if all incident

photons are counted. The electron to photon ratio is defined as internal quantum efficiency (IQE) when the number of photons is restricted to those who are absorbed by the solar cells. In other word, the transmitted and reflected photons are excluded for IQE calculation. EQE measurement system consists of solar simulator, monochromator and photodetector. The monochromator produces monochromatic light from the simulated sunlight, and the wavelength of the monochromatic light can be adjusted over visible and adjacent ranges. The photodetector is used to detect and calibrate the intensity of the monochromatic light. The EQE spectrum is obtained by recording the photocurrent of the solar cell at each single wavelength, followed by calculation with the equation:

$$EQE = \frac{\text{photocurrent}/(\text{charge of one electron})}{(\text{total power of photons})/(\text{energy of one photon})} \quad (7)$$

CHAPTER 4. FABRICATION OF METAL ELECTRODES VIA ELECTROLESS DEPOSITION

The shortcomings of vacuum-deposited metal electrodes have been discussed in Chapter 2. In this chapter, high quality metal electrodes fabricated by PAMD method are demonstrated. Well-controlled metal patterns are obtained through several approaches. The polymer and metal are characterized in detail, and the advantages of PAMD method is discussed.

4.1 Introduction

Metal electrodes are critical for electronic devices, because they are highly conductive over a wide range of temperature. Vacuum-based techniques are commonly used for the deposition of metal electrodes to lower down the melting point of metals. However, the disadvantages of vacuum-deposited metal electrodes are obvious. First, the vacuum-deposited metal films usually show poor adhesion to the substrate, which increases risk of mechanical failure, especially for flexible electronic devices^[171]. Second, the request of vacuum chamber limits the scalability of devices, so the fabrication of large area devices is time consuming and high cost^[172]. As a result, developing vacuum-free metal deposition techniques is of great interest^[173]. Solution-based metal deposition is ideal for large area and high throughput fabrication of metal electrodes. In general, there are two strategies for solution deposition of metal electrodes. One approach is the direct printing of noble metal nanoparticle/nanowire ink on the substrate^[174]. The other method is the *in-situ* deposition of metal thin films by chemical or electrochemical reactions^[175, 176]. Although the directly printing of AgNP ink has been used for the fabrication of vacuum-free OSC modules^[37], the printed Ag electrodes show quite high surface roughness and poor mechanical stability. Besides, most of the printed Ag electrodes require high temperature post-annealing process to improve the conductivity, which is not good for flexible substrates^[177]. Electrodeposition is a way to fabricate high quality metal electrodes, but it requires conductive substrate for the successful deposition

of metal. Comparing with these two approaches, the electroless deposition (ELD) of metal is low cost, facile, and versatile for various of substrates^[178]. For electroless deposition, catalytic “seed” on the surface of the substrate is always required for the selective plating of metal^[176]. However, the seed is always deposited by physical or chemical adhesion on the entire substrate, which makes it impossible for the deposition of patterned metal electrodes. As a result, an additional photolithography process is required to pattern the metal electrodes^[179]. The time consuming and complicated photolithography process limits the scalability of the metal electrodes fabricated by this approach.

In this work, a facile electroless deposition strategy is developed and studied. Patterned Cu thin films are deposited on multiple types of substrates through PAMD, and the entire deposition is free from high vacuum, high temperature or photolithography. The functional polymer not only serves as the anchor for catalytic precursor, but also works as an adhesive layer between Cu electrodes and the substrate. Two printing strategies are developed to achieve designed patterns the Cu electrodes. The first method is modifying the entire substrate with the functional polymer by radical polymerization, and then printing the catalytic precursor by screen printing. Such method is named “patterning the catalytic precursor” (PCP) for short. The second method is printing a copolymer ink on the substrate, and then crosslinking the copolymer with substrate under UV irradiation. Correspondingly, this method is called “patterning the functional polymer” (PFP) for short. Both methods have been proved to be effective for the fabrication of high quality patterned Cu electrodes. The deposited electrodes show low surface roughness, good adhesion to substrate, and excellent mechanical stability under bending test. Such PAMD Cu electrodes will be demonstrated as bottom electrodes for stretchable OSCs in Chapter 6.

4.2 Experimental Section

4.2.1 Preparation of Cu Plating Bath

The Cu plating bath consisted of a 1:1 mixture of newly prepared solution A and B. Solution A included 12g/L NaOH (Uni-Chem), 13 g/L CuSO₄·5H₂O (Uni-Chem), and 27 g/L potassium sodium tartrate (Uni-Chem) in DI water. Solution B was a diluted HCHO (9.5 mL/L, Uni-Chem) aqueous solution. The solution was filtered by 0.45 μm PTFE filter before use.

4.2.2 PAMD of Cu Electrodes by Patterning the Catalyst

PET substrates were cleaned in ultrasonic bath of acetone, isopropanol, and deionized (DI) water, respectively. After cleaning, PET substrates were dried by compressed air, and then treated with oxygen plasma for 5 min. Afterwards, the substrates were immersed into a 0.5% [3-(methacryloyloxy)propyl] trimethoxysilane (MPTS) solution with 95% ethanol, 1% acetic acid and balanced DI water for 1 h. Then these substrates were immersed into an aqueous solution of 20 wt% 2-(methacryloyloxy)ethyl-trimethylammonium chloride (METAC) and 0.25 wt% potassium persulfate and heated at 80 °C for 60 min. The catalytic precursor ink consisted of 20 mg (NH₄)₂PdCl₄, 5 g poly(ethylene glycol) (PEG, M_w = 4,000) and 2 mL DI water. The precursor ink was printed on the substrates by screen-printing. Then, the substrates were stored in dark environment for 30 min, followed a plasma-treatment for 2 min. The substrates were rinsed with DI water to remove the excess catalytic precursor. Finally, the ELD of Cu was performed in a plating bath consisting of a 1:1 mixture of freshly prepared solution A and B. The PET substrates were obtained from DuPont company, and all other chemicals were obtained from Sigma-Aldrich. All chemicals were used as received.

4.2.3 Synthesis of Photoreactive Copolymer

The photoreactive copolymer poly(4-methacryloyl benzophenone-co-2-methacryloyloxy ethyltrimethylammonium chloride) (P(MBP-co-METAC))

was synthesized by a two-step reaction, including the nucleophilic substitution of methacryloyl chloride with 4-hydroxybenzophenone to obtain 4-methacryloyl benzophenone (MBP), and the free-radical polymerization of MBP and METAC. In the first step, 5.5 g 4-hydroxybenzophenone and 5 mL triethylamine were dissolved into 200 mL anhydrous CH_2Cl_2 , then 4 mL anhydrous CH_2Cl_2 solution of methacryloyl chloride was added into the mixture solution dropwise under ice bath. The mixture solution was kept under stirring for 24 h. The mixture was then washed with 10 wt% HCl solution, saturated NaHCO_3 , and water respectively for three times. Next, the solution was dried by anhydrous Na_2SO_4 , and the solvent was evaporated by rotary evaporation at 60 °C. Finally, the light yellow or white needle-like MBP monomer was obtained by recrystallization in hexane. The second step is the polymerization of MBP and METAC. 4.4 g of as-prepared MBP and 13.3 g METAC were added in 100 mL anhydrous 2-methoxyethanol. The solution was kept under inert atmosphere by bubbling with N_2 gas for about 30 min. Afterward, 0.14 g 2,2'-azobis-isobutyronitrile (AIBN) was added in the solution. The reaction was kept at to 65 °C for over 24 h under stirring. Finally, the yellowish copolymer solid was obtained by precipitation with acetone.

4.2.4 Preparation of Copolymer Patterns by Printing Techniques

For soft lithography molding method, a patterned PDMS stamp was attached on the PET substrate. Then, 10 μL 2 wt% ethanol solution of P(MBP-co-METAC) was dropped at the interface between the stamp and the substrate. The solution passed through the channels between the stamp and the substrate due to capillary force. Afterwards, the copolymer was crosslinked with the substrate under UV irradiation for 10 min, and the stamp was then peeled-off from the substrate gently.

For the inkjet printing method, 0.5 wt% copolymer solution in 2-methoxyethanol was filtered with 0.45 μm PTFE filter before use. A commercially available household inkjet printer (Canon PIXMA iP4980) was

used for the inkjet-printing of copolymer patterns. The copolymer solution was filled in the ink cartridges of the printer before printing. The patterns were designed in a PC with CorelDraw X5 software. The PET substrates were cut into A4 size, and filled in the printer as papers. The printed copolymer patterns were dried in an oven at 70 °C, and then cured under UV light for 10 min.

For screen printing method, 40 g PEG, 10 mL DI water and 5 mL 10 wt% copolymer solution in 2-methoxyethanol were mixed together, and then heated at 80 °C for 2 h under severe stirring. A white gel-like copolymer paste was obtained after cooling-down of the mixture. The copolymer paste was printed on cotton or polyester fabrics through a silk screen, and the catalytic precursor ink (same as the one introduced in 4.2.2) was screen-printed on the same areas sequentially. Next, the patterns were cured under UV irradiation for 10 min. The fabrics were washed with DI water carefully to remove the excess copolymer and catalytic precursor.

4.2.5 PAMD of Cu Electrodes by Patterning the Polymer

For soft lithography and inkjet printing methods, the copolymer-patterned substrates were immersed into a 1 mg/mL solution of $(\text{NH}_4)_2\text{PdCl}_4$ for 10 min. Then, they were rinsed with DI water, and immersed in Cu plating bath for 5 min to finish the deposition.

For screen printing method, the ion exchange process has been done after the printing of catalytic precursor paste. As a result, the cleaned substrates were immersed in Cu plating bath directly. The plating process took about 30 min to obtain highly conductive ($1 \Omega/\square$) Cu electrode on cotton or polyester fabrics.

4.2.6 Characterization

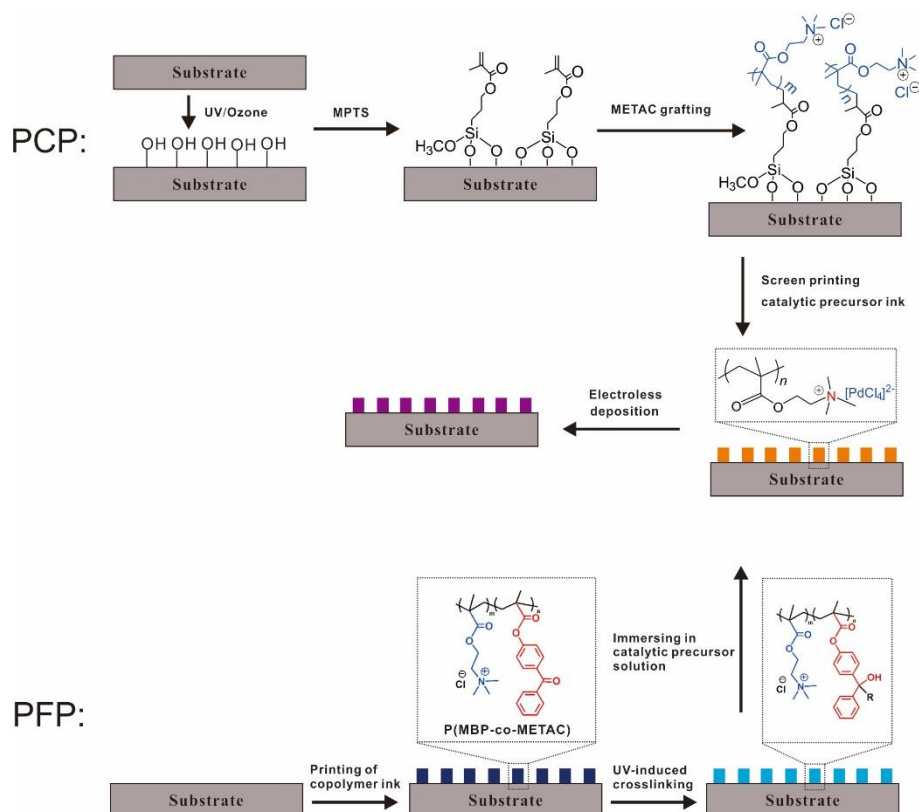
Optical images were taken by a Nikon Eclipse 80i optical microscope (Nikon, Tokyo, Japan). AFM topographic images were measured by an XE-100 AFM (Park Systems, Suwon, South Korea) with noncontact mode under ambient conditions. The sheet resistance was measured by a 4-point probe system (RTS-9, 4 PROBES TECH).

4.3 Results and Discussions

Two PAMD strategies based on different polymer grafting methods are studied in this chapter. The first method (i.e., PCP method) is modifying the entire substrate with the functional polymer by radical polymerization, and then patterning the catalyst on the polymer-modified substrate by screen-printing (Scheme 4.1). By the aid of simple plasma treatment, the anchoring molecule MPTS can be grafted on various organic or inorganic substrates, where carboxyl or hydroxyl groups are formed. The α,β -unsaturated carbonyl group in MPTS serves as the anchor for the radical polymerization with METAC. During the polymerization, most MTEAC monomers react with each other to form PMETAC polymers in the solution, while some of them are grafted on the substrate after reacting with radicalized MPTS. The selective plating of Cu is realized by patterning $(\text{NH}_4)_2\text{PdCl}_4$ catalytic precursor through screen printing. The PdCl_4^{2-} ions replace the Cl^- ions in PMETAC through ionic exchange. Such electrostatic interaction between PdCl_4^{2-} and the quaternary ammonium group in PMETAC is so strong that the absorbed PdCl_4^{2-} can hardly be removed by continuous rinsing. After screen printing, post plasma treatment is needed to destroy the PMETAC on the non-patterned area in order to avoid the diffusion of $(\text{NH}_4)_2\text{PdCl}_4$ when rinsing. The electroless metal plating bath usually consists of oxidative solution A and reductive solution B. Solution A is a mixed solution of metal salt, complexing agent and stabilizer (if needed), while solution B contains reducing agent that is more electronegative comparing with the metal ion. During electroless plating, the PdCl_4^{2-} ions are reduced to Pd nanoparticles by the reducing agent HCHO. Then, Cu nanoparticles are selectively deposited on the catalytic Pd

particles by chemical reduction. The reduction is a self-catalytic process that the generated Cu particles serve as the catalyst for the continuous electroless plating process. The PAMD Cu has stronger adhesion to substrates than vacuum deposited Cu, and it is not easy to tear the PAMD Cu off even if attached on tapes.

The second method (i.e., PFP method) is modifying selected parts of the substrate by printing techniques, and then immobilizing the catalytic precursor on the polymer modified areas (Scheme 4.1). To realize selective patterning of the functional polymer, a photoreactive copolymer that can bond with organic substrates by UV-induced crosslinking is synthesized. As illustrated in Scheme 4.1, P(MBP-co-METAC) consists of 2 kinds of monomers. One is METAC which functions the anchor for catalytic precursor, the other is MBP which crosslinks with substrate under UV irradiation. The reactivity of MBP comes from the benzophenone group, because the ketone will transform to biradical under UV excitation. The biradical is highly reactive that it can crosslink with the C-H bond of organic compounds.



Scheme 4.1 Schematic illustration of PAMD by two strategies. PCP: Metal pattern achieved by printing the catalytic precursor. PFP: Metal pattern achieved by printing the functional polymer.

The as-made Cu electrodes are characterized by multiple approaches. The components of the PAMD product is analyzed by XPS as illustrated in Figure 4.1a. The two spin-orbit peaks ($2p_{3/2}$ and $2p_{1/2}$) of Cu $2p$ indicate that the major product is pure Cu metal. However, the weak satellites around 944.4 eV indicate the existence of Cu_2O , which is not as conductive as Cu metal. The generation of Cu_2O is not due to the oxidation of Cu metal in air, but because of the side reaction during the electroless plating process^[180]. Fortunately, the amount of Cu_2O is very small that its negative impact on conductivity is limited. The resistivity of the PAMD Cu is $\sim 5 \mu\Omega\cdot\text{cm}$, which is about 3 folds of the bulk pure Cu. Such result is extraordinary among all reported metal electrodes fabricated by solution process^[181, 182]. The resolution of the Cu patterns is determined by the printing technique. For PCP method, the Cu electrodes are usually patterned by low resolution screen

printing. However, delicate patterns that are eligible for photovoltaic applications can still be obtained by screen printing, as shown in Figure 4.1b. For PFP method, the resolution of the patterns can be improved dramatically, because other high-resolution printing techniques such as soft lithography molding and inkjet printing are available (Figure 4.1d). The modification of the polymer/copolymer is versatile on multiple substrates as mentioned above. For example, Figure 4.1c demonstrates ELD Cu on PET, polystyrene (PS), PI, cotton, filter paper, and weighing paper. The results indicate that the ELD Cu is uniform and conformable on these substrates.

Apart from the conductivity, the surface topography is important for solar cell bottom electrodes. Figure 4.1e is the $10 \times 10 \mu\text{m}$ AFM topographic image of the ELD Cu electrode on PET substrate fabricated by PCP method. The root-mean-square roughness (R_{rms}) of the Cu surface is $\sim 4 \text{ nm}$, which is smoother with that of commercial ITO bottom electrodes^[183]. However, the R_{rms} of the ELD Cu fabricated by PFP method is $> 11 \text{ nm}$, which is significantly larger than the Cu electrodes fabricated by PCP method. This is because the inkjet-printed copolymer films show high surface roughness. The thickness of the Cu electrode is another key factor for bottom electrode application, since too high thickness/step height may lead to non-uniform coverage of the upper layers. The thickness of ELD Cu prepared by the first and second method is 100 nm and $> 400 \text{ nm}$, respectively. The reason is that inkjet-printed copolymer film (180 nm) is thicker than the polymer film prepared by radical polymerization (20 nm). Hence, the step height between Cu surface and the substrate is $> 400 \text{ nm}$ for the Cu electrodes fabricated by PFP method (Figure 4.1f).

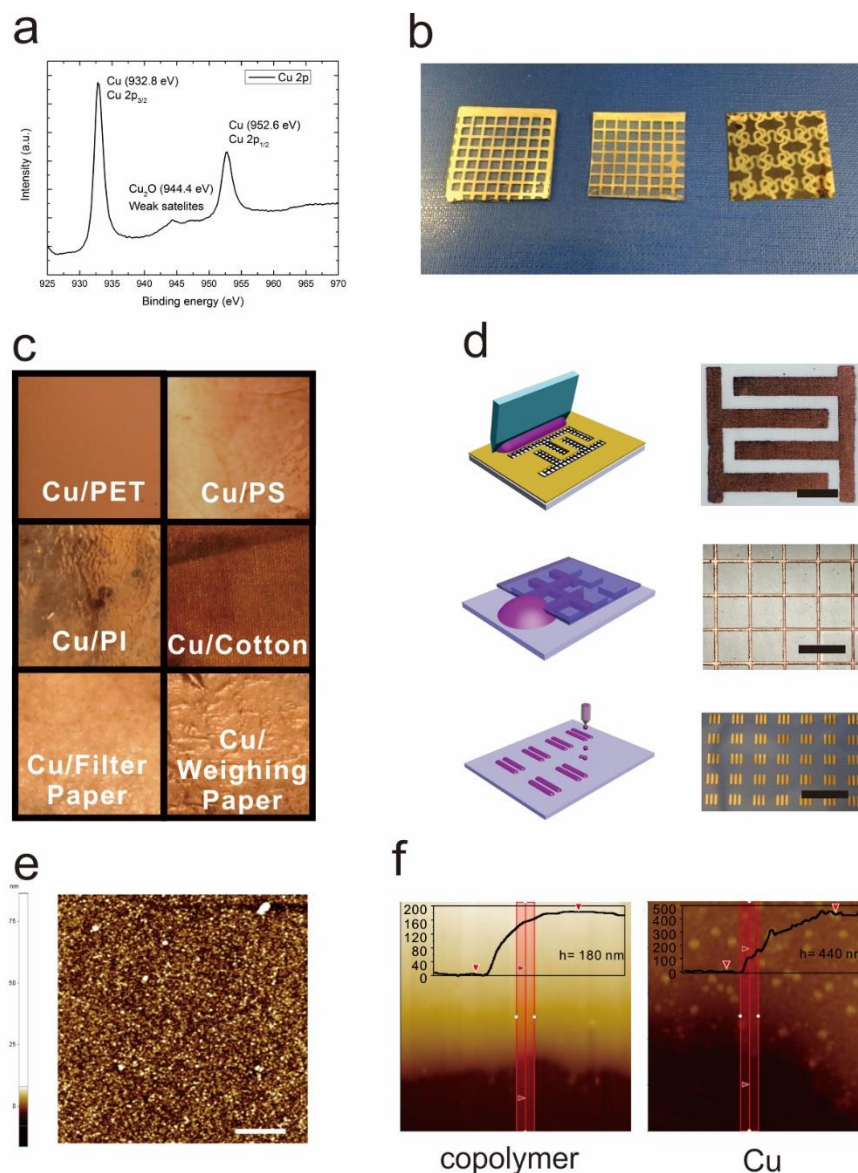


Figure 4.1 Characterization of ELD Cu electrode. (a) XPS analysis of ELD Cu. (b) Optical image of 2.5×2.5 cm Cu patterns on glass (left), PET (middle) and PI (right). (c) Optical images of ELD Cu on multiple organic substrates. (d) schemes and optical images of ELD Cu patterns fabricated by PFP method: interdigitated Cu electrodes on cotton fabric by screen printing (top), Cu meshes on PET by soft lithography molding (middle), and Cu strips on PET by inkjet printing (bottom). Scale bars are 1 cm, 150 μ m, and 2 cm, respectively. (e) AFM topographic image of ELD Cu surface fabricated by PCP method. Scale bar is 2.5 μ m. (f) AFM lateral profiles of copolymer pattern and ELD Cu fabricated by PFP method.

4.4 Conclusions

Solution-processed Cu electrodes on flexible substrates are obtained by ELD with PAMD technology. Two strategies are developed for achieving patterned Cu electrode by patterning either functional polymer or catalytic precursor. The advantage of PCP method is the low surface roughness of the obtained Cu film, while PFP method is more suitable for printing of high-resolution and complicated Cu patterns.

CHAPTER 5. SOLUTION-PROCESSED TCO-FREE SEMI-TRANSPARENT PEROVSKITE SOLAR CELLS FOR FLEXIBLE AND TANDEM APPLICATIONS

Transparent electrodes are indispensable components for OSCs and PSCs. Traditional OSCs and PSCs employ TCOs as transparent electrodes, which are high performance but mechanically brittle. In this chapter, highly conductive n-PEDOT:PSS will be studied as transparent electrodes for PSCs. The n-PEDOT:PSS electrodes will be used as both top and bottom electrodes for PSCs, and the device performance will be investigated by the characterization of tandem solar cells and flexible solar cells based on the n-PEDOT:PSS electrodes.

5.1 Introduction

Semi-transparent solar cells have drawn unprecedented attention for their applications in recent years. By optical engineering such as tuning the bandgap of the active material^[184, 185], or engineering on the transparent electrodes^[186, 187], the color and transmittance of the semi-transparent solar cells is adjustable, which reveals potential applications on buildings^[110, 188], wearable electronics, and fashion. More importantly, semi-transparent property also enables the viability of tandem solar cells, which may further improve the PCE value by utilizing two or more types of absorbers^[43, 53, 92]. Among the several kinds of solar materials suitable for making semi-transparent solar cells, organolead halide perovskites (typically $\text{CH}_3\text{NH}_3\text{PbI}_3$) have showed great advantage owing to the low-cost, high charge-carrier mobility, high absorption coefficient, and good solution-processability of perovskite materials^[19, 55, 169, 189-197]. Impressively, the power conversion efficiency (PCE) of opaque perovskite solar cells has reached >20%, a milestone which can compete with Si-based solar technology^[198]. For perovskite materials, the tunable band gap by cation or anion doping makes it suitable for tandem cells with highly efficient solar cells, such as copper

indium gallium selenide (CIGS), crystalline Si (c-Si) or another layer of perovskite^[54, 74, 199, 200].

Key comes back to transparent electrodes with low cost and solution processing ability, both top and bottom ones. To establish a trade-off between conductivity and transmittance, the transparent electrodes are crucial components in a semi-transparent solar cell. Although the state-of-the-art semi-transparent perovskite solar cells (st-PSCs) recently reached a power conversion efficiency over 16%, they required using transparent conducting oxides (TCOs) as transparent electrodes^[201]. Whereas traditional transparent conducting oxides (TCOs) such as indium tin oxide (ITO), fluorine-doped tin oxide (FTO) and aluminum-doped zinc oxide (AZO) show high transmittance (~85%) and low resistance (~15 Ω/\square), their costs are high^[202]. For example, the estimated cost of TCO electrode accounts for ~75% of the total cost of a perovskite solar module^[203]. Besides the cost issue, these TCOs are mechanically brittle and therefore their applications on flexible and wearable electronics are restricted^[204, 205]. As a result, developing TCO-free PSC is of great interest^[167, 206, 207].

Another solution to reduce the fabrication cost is fabricating the device through low-temperature solution methods, which are compatible with low cost, large area and high throughput roll-to-roll (R2R) process^[37, 38]. Traditional vacuum deposition technology is not ideal when integrated to R2R process because the size of vacuum chamber limits the area of the substrate. Apart from the TCOs that require vacuum technology, challenge comes from the TiO₂ film, which commonly serves as the electron transport layer (ETL) in conventional highly efficient PSCs^[208, 209]. High temperature annealing (> 500 °C) is usually required for such TiO₂ layer to eliminate the defects, and to improve the conductivity. Most of the transparent electrode materials can barely survive from such high temperature except FTO, and all flexible substrates based on organic materials which have better compatibility with R2R process will decompose under such temperature.

Currently, all the reported semi-transparent PSC employs vacuum-deposited materials to serve as at least one of the transparent electrodes due to the challenges mentioned above. As far as we know, there is no report on TCO-free semi-transparent PSC that can be fabricated by low-temperature solution way.

Here, we demonstrate a facile full-solution strategy to fabricate TCO-free high performance st-PSC. To the best of our knowledge, this is the first report of TCO-free, fully solution processed st-PSCs. Each functional layer in the PSCs is processed by simple and fast solution coating or printing method, which are compatible with fast and scalable R2R process. We use a facile transfer printing method to fabricate both transparent electrodes with solution-processed PEDOT:PSS. We also make use of low temperature processed ZnO as the ETL instead of TiO₂. The whole fabrication process is under low temperature (<130 °C), which provides sufficient viability to realize flexible devices based on this strategy. The champion st-PSC fabricated by this approach shows very high efficiency (~13.9%), while the four-terminal PSC/Si tandem solar cell exhibiting an overall PCE of 19.2%. In addition, we obtain high flexible semi-transparent PSCs based on 125 μm thick polyethylene terephthalate (PET) and ~1 μm thick polyimide (PI) substrates. We believe that our results are beneficial for realizing R2R fabrication of high performance and low-cost PSCs, which is promising for large area tandem solar cells and wearable electronics in the future.

5.2 Experimental Section

5.2.1 Materials and synthesis

Patterned ITO/glass slides were obtained from Zhuhai Kaivo Optoelectronic Technology Co., Ltd.) Polydimethylsiloxane (PDMS) prepolymer and the curing agent (Sylgard 184) were obtained from Dow Corning. The two reagents were mixed at a ratio of 10:1 (w/w), degassed and heated at 70 °C for about 2h to prepare crosslinked PDMS mold. Lead (II) iodide (99.999%), lead (II) bromide (99.999%), formamidinium iodide (FAI, >98%),

methylammonium bromide (MABr, 98%), bis(trifluoromethane)sulfonimide lithium salt (Li-TFSI, 99.95%), tris(2-(1H-pyrazol-1-yl)-4-tert-butylpyridine) cobalt(III) tri[bis(trifluoromethane)sulfonimide] (FK 209 Co (III) TFSI salt, 98%), and 4-tert-butylpyridine (tBP, 96%) were obtained from Sigma-Aldrich. 2,2',7,7'-tetrakis(N,N-di-p-methoxyphenylamine)-9,9'-spirobifluorene (Spiro-OMeTAD, 99.5%) was obtained from Derthon Optoelectronic Materials Science Technology Co., Ltd. Highly conductive PEDOT:PSS solution (Clevios PH 1000, 1.0 ~ 1.3 wt% in water) was obtained from Heraeus. The ZnO precursor was prepared by a simple hydrolysis method reported elsewhere. Briefly, 0.1g zinc acetate dehydrate was dissolved in a mixture of 27.5 μ L ethanolamine and 1 mL 2-methoxyethanol. The solution was kept in ambient environment under severe stirring for 12 h. The perovskite precursor solution consists of 2.645 g PbI₂, 0.372 g PbBr₂, 0.940 g FAI, 0.113 g MABr, 4 mL dimethylformamide (DMF), and 1 ml dimethyl sulfoxide (DMSO). The solution was ready for use after stirring for 30 min at room temperature. All these solutions were filtered by 0.45 μ m PTFE filter before every use.

5.2.2 Device fabrication

For ITO ref. device, ITO/glass was cleaned by ultrasonic bath of acetone, isopropanol and deionized (DI) water for 30 min each. The ITO slide was then treated with plasma to improve the wettability. For TCO-free device, nitric acid-annealed PEDOT:PSS was used as bottom electrode instead of ITO. A glass slide was firstly treated by piranha solution (H₂SO₄: H₂O = 3:1, volume ratio) for 10 min and then rinsed with DI water. Then PEDOT:PSS solution was spin-coated on the glass slide at 500 rpm for 5 s and 1000 rpm for 1 min, followed by 125 °C annealing for 10 min. The PEDOT:PSS film was then immersed in 70% nitric acid bath for 10 min. Afterwards the slide was rinsed and dried on a hot plate at 120 °C. A thin layer of ZnO electron transport layer was formed on both types of bottom electrodes by spin-coating of ZnO precursor solution at 4000 rpm for 1 min. The electron transport layer was then annealed at 130 °C for 30 min. For TCO-free device, a diluted ZnO precursor solution (volume ratio 1 : 1 with isopropanol) was spin-coated on

PEDOT:PSS film at 5000 rpm for 30s and then annealed at 130 °C for 5 min to serve as compact layer before the spin-coating of the ZnO precursor solution. The slide was then transferred to a N₂-filled glovebox, and 40 μL perovskite precursor solution was spin-coated on ZnO at 6000 rpm for 30 s. 150 μL chlorobenzene was dropped atop the spinning slides at 20 s of the spin-coating step. After coating of the perovskite layer, the slide was annealed at 100 °C for 2 to 30 min. Then, 40 μL spiro-OMeTAD solution was spin-coated atop the perovskite layer at 5000 rpm for 20 s. The solution contains 70 mg spiro-OMeTAD, 25 μL Li-TFSI solution (520 mg/mL in acetonitrile), 32 μL tBP, and 6 mg FK 209 TFSI salt in 1 mL chlorobenzene. Finally, n-PEDOT:PSS film was transfer-printed atop the spiro-OMeTAD layer as described in main body above. For the opaque reference device, 100 nm of Au was deposited on the spiro-OMeTAD layer at 0.3 nm/s by thermal evaporation. Au bars were also deposited along one edge of both bottom and top n-PEDOT:PSS electrodes to improve the contact between the electrodes and testing wires. The c-Si solar cells were provided by Dr. Jixiang Zhou and Prof. Hui Shen in Sun Yat-Sen University.

5.2.3 Characterizations

The optical transmittance was measured by Agilent Cary 7000 UV-Vis spectrometer. The AFM topographic images were obtained by an XE-100 AFM (Park Systems, Suwon, South Korea) in non-contact mode. The ITO reference, pristine and treated PEDOT:PSS were characterized by ultraviolet photoelectron spectroscopy (Kratos AXIS ULTRA HAS, He-I α = 21.22 eV) and X-ray photoelectron spectroscopy (XPS, Kratos AXIS ULTRA HAS, monochromated Al K α = 1486.6 eV). The SEM images were measured by a CARL ZEISS ULTRA 55 scanning electron microscope. The J-V characteristics of the devices were characterized by a Keithley 2400 sourcemeter. To simulate standard sunlight, a solar simulator with AM 1.5 filter (91160, Newport, 100 mW/cm²) was used as the light source. The solar simulator was calibrated by a standard Si solar cell before use. To determine the active area of the device, a shadow mask (0.06 cm²) was attach on the device before testing. The EQE of the devices were measured with a standard

system consists of a xenon lamp (Oriel 66902, 300 W), a monochromator (Newport 66902), a Si detector (Oriel 76175_71580) and a dual channel power meter (Newport 2931_C).

5.3 Results and Discussions

5.3.1 Fabrication and Solar Cell Structure

Among all the substitutes of TCOs, conducting polymer poly(3,4-ethylenedioxythiophene) polystyrene sulfonate (PEDOT:PSS) is one of the most promising candidate because of its solution processability, which shows good compatibility with R2R processes^[47, 135, 210]. However, direct application of this water-based solution onto PSCs will significantly degrade the device due to the high sensitivity of the perovskite layer to moisture^[211, 212]. Recently, You et al. combine PEDOT:PSS with graphene to obtain composite transferable transparent electrode^[197]. Indeed, the strategy of graphene/PEDOT:PSS electrode was quite successful that their best device shows an extraordinary PCE value of ~12%. However, the fabrication of their graphene based electrodes requires multiple time-consuming etching and transfer process, which will probably limit the mass production of devices based on this technique. As illustrated in Figure 5.1a, the fabrication of one device started with nitric acid-annealed PEDOT:PSS film on glass substrate. A recent study of Kim et al. discovered that a sulfuric acid treatment of PEDOT:PSS film not only improves its conductivity but also makes it transferable by removing most of the non-conductive PSS components^[152]. Previous studies have proved that nitric acid treatment also improves the conductivity of PEDOT:PSS significantly by partly removing the PSS component^[213]. In this study, we found that the nitric treatment will also make the PEDOT:PSS film transferable, which is similar to the effect of sulfuric acid treatment mentioned before. Thus, the fully solution-processed device was realized by replacing traditional TCO-based bottom and top electrodes with ~50 nm highly conductive nitric acid-annealed PEDOT:PSS (n-PEDOT:PSS) films. Since the PEDOT:PSS electrode will decompose under ~500 °C high temperature, which is required as the conventional post-treatment of TiO₂ compact film to remove the organic residues, a low-

temperature (130 °C) processed ZnO thin layer is applied as a blocking layer to avoid the direct contact between 2,2',7,7'-tetrakis(N,N'-di-p-methoxyphenylamine)-9,9'-spirobifluorene (spiro-OMeTAD) layer and bottom n-PEDOT:PSS electrode. The ZnO precursor solution is spin-coated on n-PEDOT:PSS film or ITO, followed by annealing to remove the solvent. It is worth noting that the ZnO solution reveals wetting problem on n-PEDOT:PSS film, thus the coated ZnO film exhibits pinholes and aggregations which will lead to device failure. As a result, the ZnO solution is diluted in isopropanol to improve the wettability when coating on n-PEDOT:PSS film. Then, the perovskite layer is deposited through a one-step method, by spin coating a mixed cation perovskite precursor solution and then annealing at 100 °C for 2 min^[214]. After the dark brown perovskite film has been formed, ~200 nm spiro-OMeTAD is deposited by spin coating its chlorobenzene solution. Here, the spiro-OMeTAD layer not only serves as HTL but also works as a smoother to reduce the surface roughness. Such an interfacial layer is crucial for the successful transfer of n-PEDOT:PSS top electrode. Meanwhile, a flat PDMS stamp is attached onto the Si/n-PEDOT:PSS film for the transfer printing process. Afterwards, the n-PEDOT:PSS film is peeled off from the Si wafer and then attached onto the spiro-OMeTAD layer. A fast plasma treatment (~ 3s) of the n-PEDOT:PSS film before attaching to the target HTL surface is necessary for the successful transfer printing. Finally, the n-PEDOT:PSS film is attached with the spiro-OMeTAD layer after a quick thermal treatment (~60 °C), and the PDMS stamp is lifted up without causing any damage to the PEDOT:PSS film. The whole fabrication process, including the deposition of both electrodes, is free from high vacuum and high temperature treatment. The SEM cross-sectional image indicates an intimate contact between the spiro-OMeTAD layer and the top n-PEDOT:PSS electrode (Figure 5.1b).

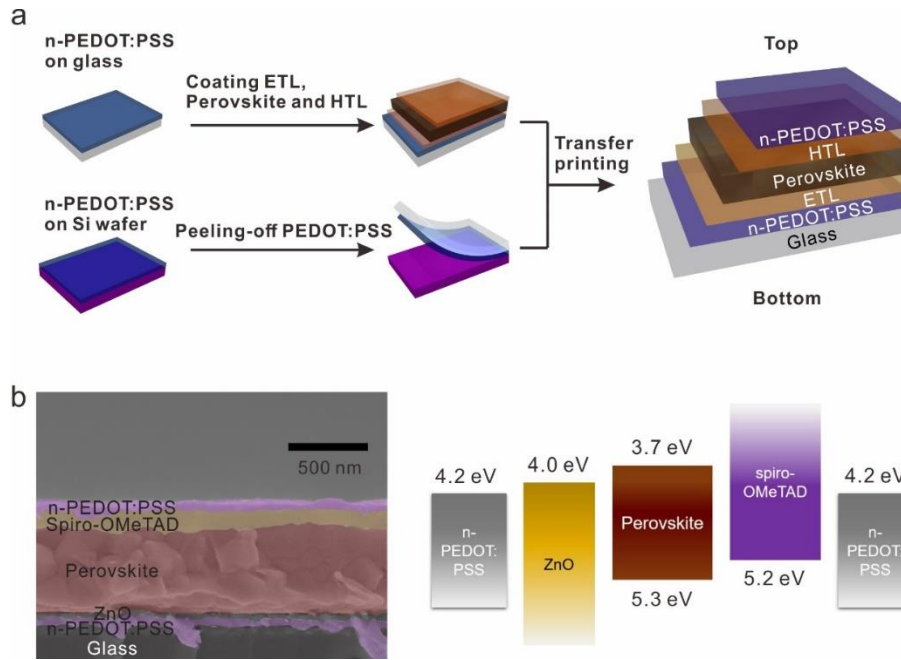


Figure 5.1 Fabrication and solar cell structure (a) Schematic illustration of the fabrication steps of TCO-free st-PSC. (b) SEM cross-sectional image (left) and energy-level diagram (right) of the TCO-free st-PSC. Scale bar is 500 nm.

5.3.2 Nitric Acid-annealed PEDOT:PSS

To investigate whether the n-PEDOT:PSS film is eligible for transparent electrode application, the surface morphology, conductivity and transmittance of the treated film were measured, and then compared with those of the pristine PEDOT:PSS (p-PEDOT:PSS) and sulfuric acid-annealed PEDOT:PSS (s-PEDOT:PSS) film. Briefly, PEDOT:PSS solution is spin-coated on 3 glass slides at same spinning speed and annealed to evaporate the solvent. Then one of them is reserved as reference, while the other 2 are treated with sulfuric acid and nitric acid, respectively. While p-PEDOT:PSS exhibits a very large sheet resistance of $\sim 1 \text{ M}\Omega/\square$, the sheet resistance of s-PEDOT:PSS and n-PEDOT:PSS are $50 \text{ }\Omega/\square$ and $38 \text{ }\Omega/\square$, respectively. The significant boost of conductivity by acid treatment is attributed to the removal of PSS component. As a result, the thickness of PEDOT:PSS film decreased dramatically after the acid treatment (Figure 5.2a). The higher conductivity and transmittance of n-PEDOT:PSS makes it a better transparent electrode comparing with s-PEDOT:PSS. The surface morphology of the film is very

important for bottom transparent electrode. The root mean square roughness R_q of n-PEDOT:PSS was ~ 1.5 nm, which was similar to that of p-PEDOT:PSS and s-PEDOT:PSS according to AFM characterization. The optical transmittance of the treated PEDOT:PSS are slightly lower than the untreated one as shown in Figure 5.2b. All the PEDOT:PSS films show $>80\%$ transmittance at 550 nm, which is comparable to that of ITO. The PEDOT:PSS electrodes are further investigated by ultraviolet photoelectron spectroscopy (UPS), X-ray photoelectron spectroscopy (XPS) and Raman spectroscopy to study the effect of acid treatment. As shown in Figure 5.2c, the work function of PEDOT:PSS decreased significantly after the acid treatment. Both the H_2SO_4 and HNO_3 treated PEDOT:PSS samples show a similar work function of ~ 4.2 eV, which is ~ 0.4 eV lower than that of the pristine PEDOT:PSS film.

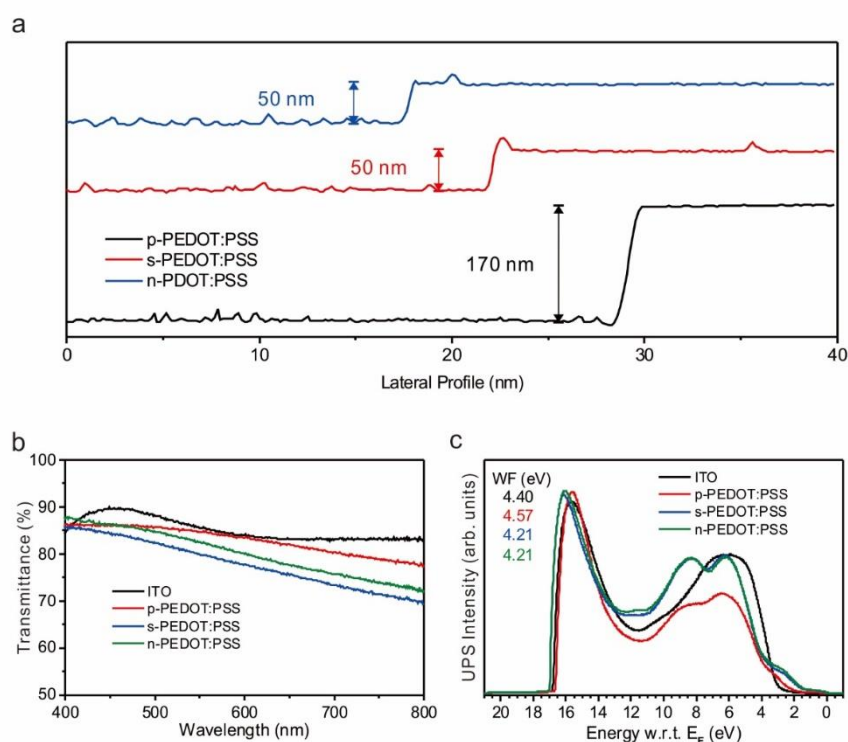


Figure 5.2 Physical properties of nitric acid treated PEDOT:PSS. (a) Profile diagram of a scratched edge of the PEDOT:PSS films measured by AFM. (b) UV-Vis spectra of ITO, p-PEDOT:PSS, s-PEDOT:PSS and n-PEDOT:PSS on glass substrates. (c) UPS spectra ($\text{He-I}\alpha = 21.22$ eV) showing the secondary

electron onset (left side) and valance state region (right side) of the ITO reference sample, p-PEDOT:PSS, s-PEDOT:PSS and n-PEDOT:PSS.

By XPS analysis, a dramatic decrease of S and O characteristic peaks of PSS component is found in acid-annealed PEDOT:PSS (Figure 5.3a), indicating the removal of PSS component by acid treatment, which is consistent with previous reports.^[152] To study the componential change in detail, the XPS results of S $2p$ core-level spectra are fitted. Apparently, there are two types of S atoms in PEDOT:PSS. One is from the thiophenic S in PEDOT (binding energy 163~166 eV), while the other comes from the sulfonate S in PSS (binding energy 167~171 eV). According to the XPS results, the PSS component in pristine PEDOT:PSS consists of 1:2 molar ratio of $\text{PSS}^- \text{H}^+$ and $\text{PSS}^- \text{Na}^+$, among which the Na^+ originates from the oxidizing process during the polymerization of PEDOT. For pristine PEDOT:PSS, the PEDOT to PSS ratio is determined to be 0.94. This value changes dramatically in acid-annealed PEDOT:PSS, as expected. The PEDOT to PSS ratio increases to 4.4 and 4.9, for s-PEDOT:PSS and n-PEDOT:PSS respectively (Figure 5.3b). Such variation further proves the selective removal of PSS component during acid treatment. As the n-PEDOT:PSS shows higher PEDOT to PSS ratio comparing with s-PEDOT:PSS, it is reasonable that n-PEDOT:PSS possesses a lower sheet resistance. No peak shift is observed after acid treatment of PEDOT:PSS according to Raman spectrometry, indicating that neither sulfuric acid nor nitric acid will oxidize PEDOT:PSS during the treatment. This is also proved by the XPS analysis on N $1s$ orbital (Figure 5.3c). However, the Raman signal of n-PEDOT:PSS is stronger than that of s-PEDOT:PSS and p-PEDOT:PSS, indicating the more thorough removal of PSS component which has very Raman signal due to the lack of symmetry chemical bonds (Figure 5.3d). This result is consistent with what we have observed from the XPS analysis.

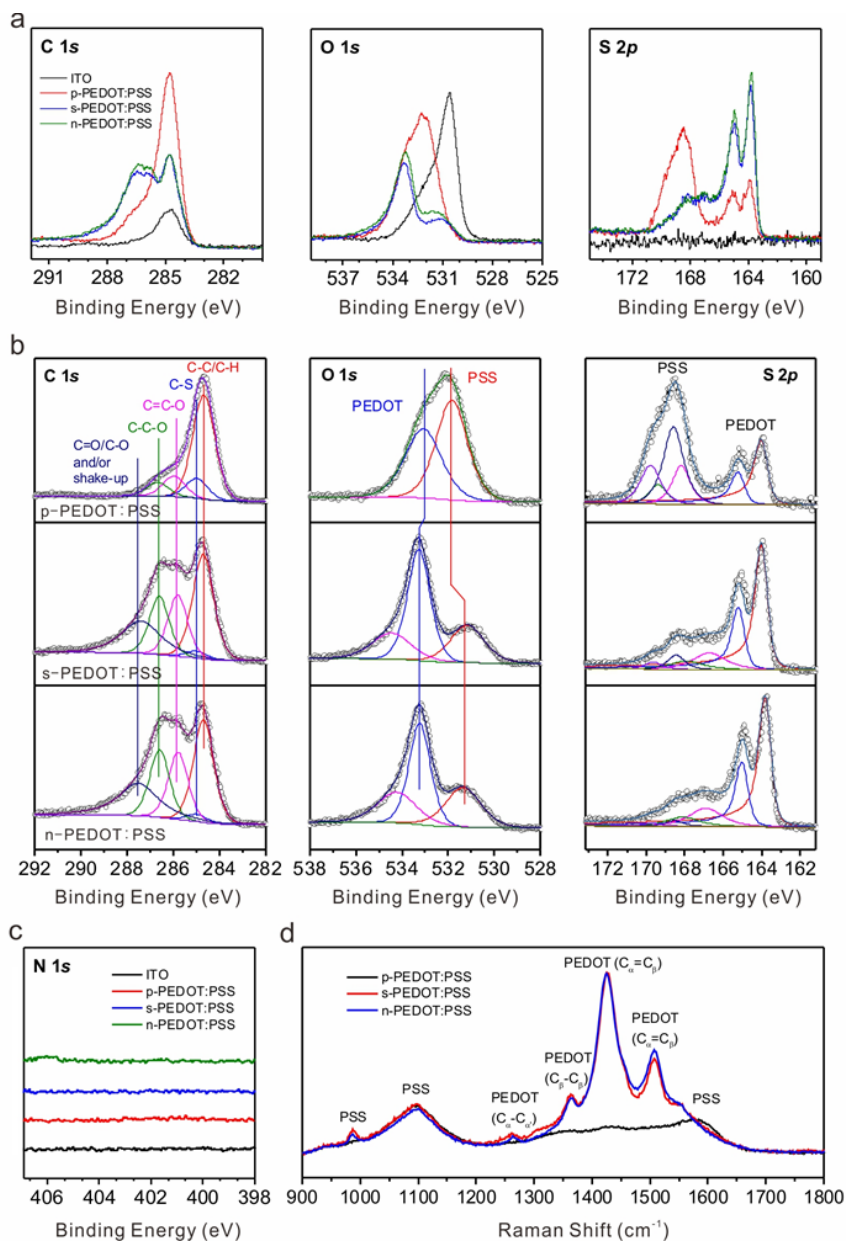


Figure 5.3 (a) XPS spectra ($Al-K\alpha = 1253.6$ eV) of the C 1s, O 1s and S 2p core levels of the ITO, p-PEDOT:PSS, s-PEDOT:PSS and n-PEDOT:PSS. (b) Fitted XPS spectra corresponding to the C 1s, O 1s and S 2p core levels of the p-PEDOT:PSS, s-PEDOT:PSS and n-PEDOT:PSS. (c) XPS N 1s core level of ITO, p-PEDOT:PSS, s-PEDOT:PSS and n-PEDOT:PSS. (d) Raman spectra of p-PEDOT:PSS, s-PEDOT:PSS and n-PEDOT:PSS.

5.3.3 Solar Cell Performance

According to our study and literature^[215], the basic nature of ZnO will lead to the degradation of perovskite during annealing. Hence the annealing time of perovskite layer should be as short as possible. However, sufficient annealing is needed to evaporate the solvent and to turn the perovskite layer to a “black” phase. Thus, the optimum annealing time of perovskite layer is studied. As illustrated in Figure 5.4a, 2 min annealing at 100 °C of the perovskite layer results in satisfactory device performance. However, longer annealing time leads to a dramatic decrease of solar cell efficiency. The photovoltaic effect completely extinguished as the annealing time goes up to 30 min. Resulting from the optical discrepancy between ITO and n-PEDOT:PSS, the average optical transmittance of the TCO-free semi-transparent solar cell (41.0%) is slightly lower than that of ITO ref. device (49.4%) between 400 nm and 1300 nm. As illustrated in Figure 5.2b, the ITO ref. device absorbs less light at 500 ~ 1200 nm, while the TCO-free device transmits more light at 1200 ~ 1300 nm. Figure 5.4c shows the J - V curves of reference cells and the TCO-free semi-transparent solar cell, the detailed parameters are listed in Table 5.1. The ITO ref. device shows a V_{OC} of 1.14 V, a J_{SC} of 21.5 mA/cm², and an FF of 67%, resulting in a PCE of 16.4% when illuminated from the bottom side. This result is one of the highest among all the reported semi-transparent perovskite solar cells in literature (Table 5.2). Correspondingly, the TCO-free device shows a V_{OC} of 1.06 V, a J_{SC} of 19.3 mA/cm², and an FF of 68%, resulting in a PCE of 13.9% when illuminated from the top side. Considering that previously reported TCO-free perovskite solar cells usually show very limited PCE value, our result is extraordinary even if compared with those opaque TCO-free devices based on highly conductive metal electrodes. When illuminated from top side, the PCE of both types of devices is lower mainly due to decreased short-circuit current density. Figure 5.4c and d demonstrates the external quantum efficiency (EQE) spectra of two types of semi-transparent devices. When illuminated from bottom side, the EQE of both types of devices reached a maximum value at wavelength of ~500 nm. The EQE of TCO-free device shows a higher slope after the peak probably due to the lower transmittance of PEDOT:PSS at longer wavelength. Thus, the EQE

results indicate lower current density of TCO-free device, which is coherent with the J-V characterization. The EQE spectra also indicate the side dependence of the short-circuit current density for the semi-transparent devices. There is an obvious gap from 400 to 450 nm in EQE spectra when illuminated from top side. This is probably due to the light absorption of spiro-OMeTAD. The ZnO layer shows obvious absorption at 400 to 500 nm, while spiro-OMeTAD absorbs UV and near-infrared light. Such difference in transmittance may result in a different output current density of the device when illuminated from corresponding side.

Table 5.1. Summary of photovoltaic characteristics of PSCs fabricated on glass.

Device type		V_{oc} (V)	J_{sc} (mA/cm ²)	FF (%)	PCE (%)
ITO ref.	(bottom illumination)	1.14	21.5	67	16.4
ITO	ref. (top illumination)	1.13	18.2	69	14.2
TCO-free	(bottom illumination)	1.06	19.3	68	13.9
TCO-free	(top illumination)	1.06	17.8	67	12.6
Opaque ref.		1.06	23.1	74	18.1

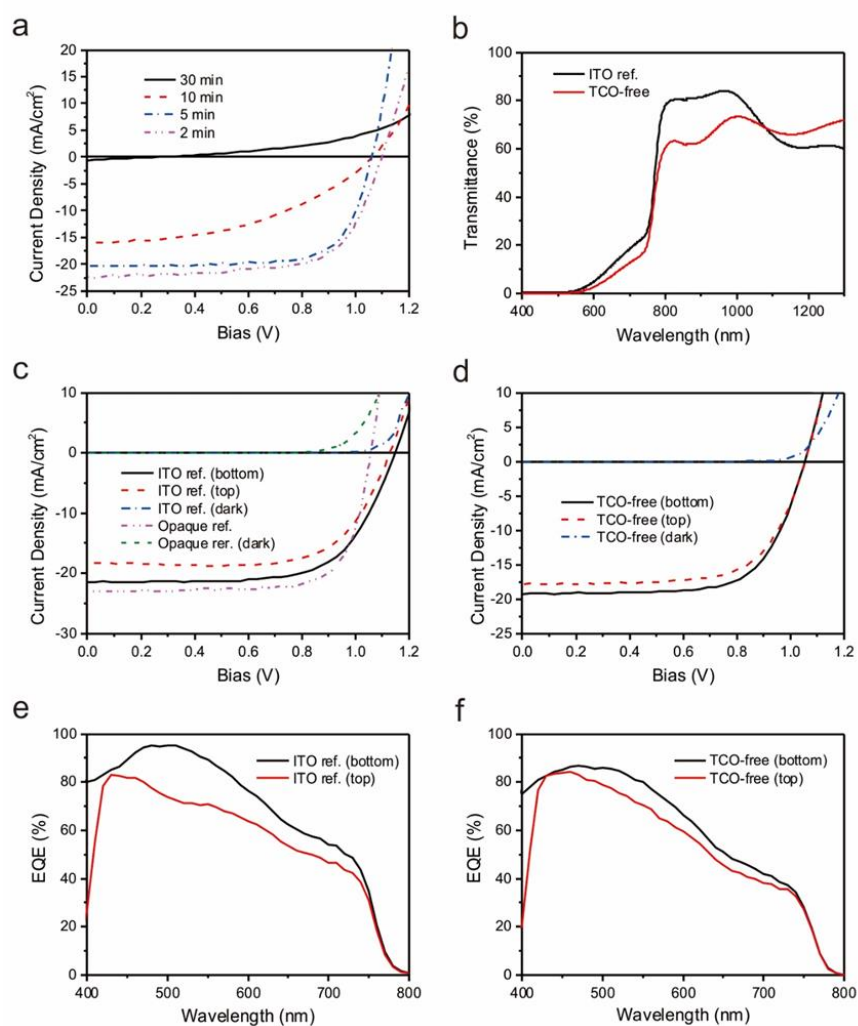


Figure 5.4 Photovoltaic performance of semi-transparent solar cells. (a) J-V curves of reference devices with different annealing time of perovskite layer. (b) Transmittance spectra of ITO ref. and TCO-free semi-transparent devices over the wavelength range of 400 to 1300 nm. (c) and (d) J-V curves of opaque reference cell and ITO based semi-transparent reference cell, and TCO-free semi-transparent perovskite solar cell. (e) and (f) EQE spectra of ITO based and TCO-free semi-transparent perovskite solar cells.

Table 5.2 Summary of state-of-the-art st-PSCs reported in the literature and by us.

top//bottom electrodes	T _{max} (°C)	TCO -free	Vacuum -free	V _{oc} (V)	J _{sc} (mA/cm ²)	FF (%)	PCE (%)	active area (cm ²)	Source
FTO//AgNW	450	×	√	1.025	17.5	71	12.7	0.39	Energy & Environmental Science 8, 956-963 (2015)
FTO//ITO	185	×	×	1.1	19.9	70.7	15.1	/	Science 351, 151-155 (2016)
FTO//graphene	500	×	×	0.960	19.17	67.22	12.37	0.24	Advanced Materials 27, 3632-3638 (2015)
ITO//ITO	120	×	×	0.97	20.3	79	15.7	0.20	Science 354, 861-865 (2016)
ITO//ITO	350	×	×	1.08	16.69	75	13.52	0.10	Advanced Materials 28, 8990-8997 (2016)
ITO//AZO	200	×	×	1.116	19.1	75.4	16.1	0.29	Nature Energy 2, 16190 (2016)
ITO//PEDOT:PSS	130	×	√	1.14	21.5	67	16.4	0.11	This work
PEDOT:PSS//PEDOT:PSS	130	√	√	1.06	19.3	68	13.9	0.11	

The application of our semi-transparent solar cells in tandem devices was further studied. ~17% efficiency monocrystalline Si (c-Si) solar cell with an active area of 0.11 cm² is used as the bottom cell. Either ITO ref. or TCO-free semi-transparent device is combined with the c-Si solar cell respectively for the J-V measurement as shown in Figure 5.5a and b, and the detailed parameters are listed in Table 5.3. The c-Si solar cell adopts anti-reflection design with pyramidal surface texture and Si₃N₄ coating to make full use of the transmitted light through top perovskite solar cell. Such anti-reflection treatment results in a large short-circuit current density of 39.3 mA/cm² and high external quantum efficiency for the standalone c-Si solar cell. Combined with the 16.4% ITO ref. cell and 13.9% TCO-free cell, the overall efficiency of the four-terminal tandem devices is 22.8% and 19.3%, respectively. While a typical perovskite solar cell converts near-UV and visible light (300 ~ 800 nm) to electricity, almost half of the photocurrent of c-Si solar cell results from the absorption of near infrared light (800 ~ 1200 nm). The remarkable transmittance of our semi-transparent solar cells at near-infrared region is critical for high performance tandem cells based on c-Si bottom cells.

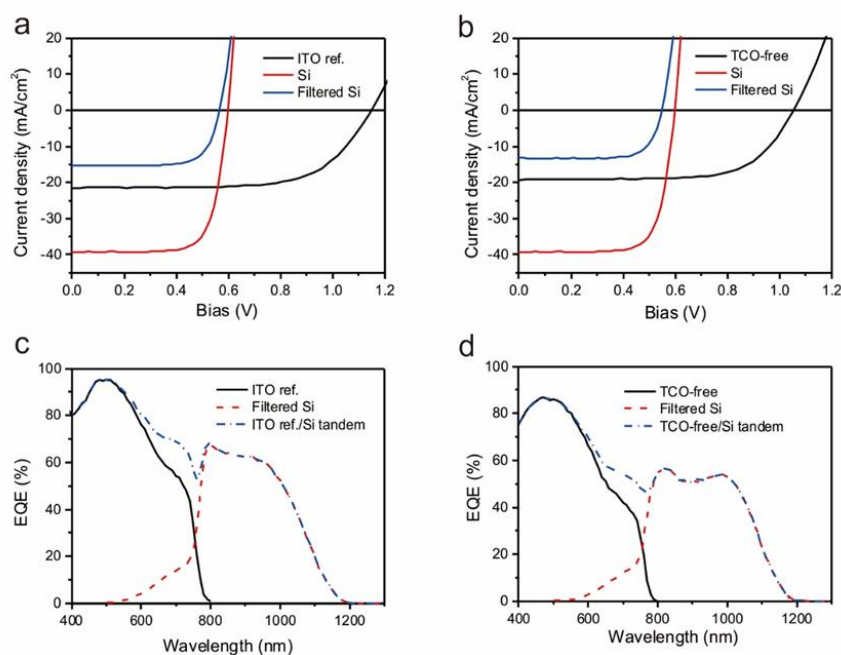


Figure 5.5 Photovoltaic performance of tandem solar cells. (a) and (b) J-V curves of ITO ref./c-Si and TCO-free/c-Si four-terminal tandem devices. (c) and (d) EQE spectra of ITO ref./c-Si and TCO-free/c-Si four-terminal tandem devices.

To demonstrate versatility of our full-solution fabrication strategy, TCO-free st-PSCs on thin PET (125 μm) and ultrathin PI ($\sim 1.5 \mu\text{m}$) substrates was fabricated. As the nitric acid treatment causes damage to these organic substrates, the bottom PEDOT:PSS electrode is prepared by transfer-printing of n-PEDOT:PSS film. The rest steps are same as the ones for TCO-free t-PSC on glass substrate. As listed in Table 5.3, the PCEs of TCO-free st-PSC on PET substrate (TCO-free@PET) and the device on PI substrate (TCO-free@PI) are 10.3% and 7.73%, respectively. The TCO-free st-PSC on PET substrate TCO-free@PET is bendable, while TCO-free@PI is conformable to arbitrary curved surface due to the ultrahigh flexibility of the thin PI. As demonstrated in Figure 5.6b, the TCO-free@PET device remained $>90\%$ of its initial efficiency after 1,000 cycles of bending at a radius of 5 mm. This is one of the best among all reported flexible PSCs. Meanwhile, the ultrathin

TCO-free@PI is highly flexible that it can be conformably attached on arbitrary curved surface (Figure 5.6d).

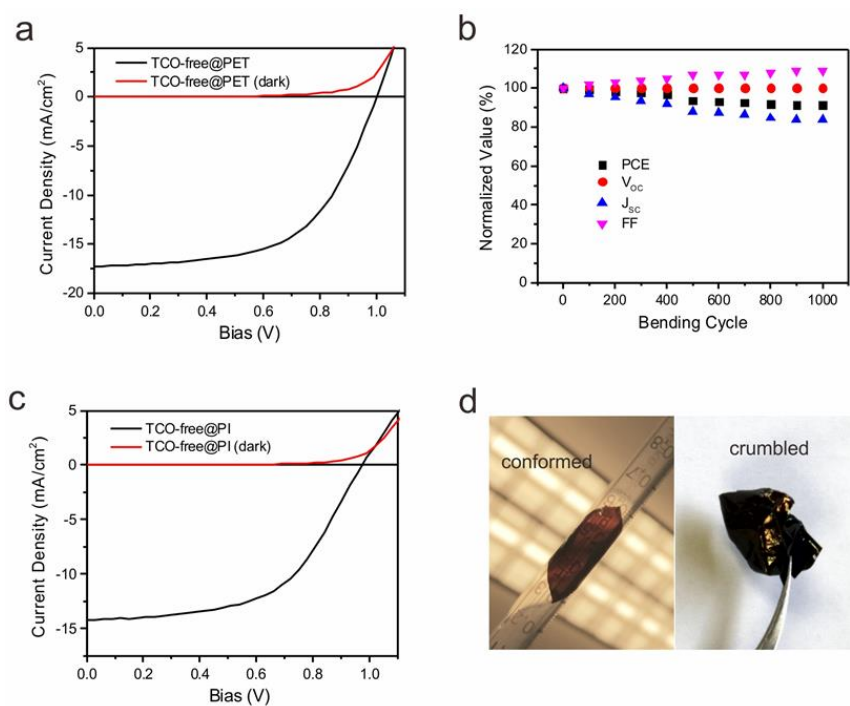


Figure 5.6 (a) J-V curves of TCO-free@PET. (b) Normalized photovoltaic characteristics of TCO-free@PET during 1000 bending at a radius of 5 mm. (c) J-V curves of TCO-free@PI. (d) Photographs of ultrathin TCO-free@PI conformably attached on a 1 mL syringe (left), and crumbled by a tweezer (right).

Table 5.3 Summary of device performance of four-terminal tandem solar cells and flexible st-PSCs.

Device type	V_{oc} (V)	J_{sc} (mA/cm ²)	FF (%)	PCE (%)
TCO-free	1.06	19.3	68	13.9
c-Si	0.59	39.3	75	17.4
Filtered c-Si	0.54	13.2	75	5.3
TCO-free/c-Si Tandem				19.2
TCO-free@PET	0.99	17.3	60	10.3
TCO-free@PI	0.99	14.2	55	7.73

5.4 Conclusions

We have developed a facile strategy to fabricate full-solution processable semi-transparent solar cells. The ITO-based device shows a maximum PCE of >16%, which is one of the highest among all the reported st-PSCs. More importantly, for the first time, TCO-free st-PSC is realized by employing n-PEDOT:PSS as both bottom and top electrodes. The TCO-free devices show a maximum PCE of ~14%, which is the one of highest among all the TCO-free PSCs. Note that our approach is totally vacuum-free and solution-processable, it is highly compatible with low cost scalable processes such as R2R process. In addition, the entire fabrication is conducted under low temperature, which provides the viability of realizing flexible perovskite solar cells based on it. Highly flexible TCO-free@PET and TCO-free@PI devices are fabricated as proof-of-concept, and the TCO-free@PET device exhibited >90% retention of PCE after 1,000 cycles of bending at a radius of 5 mm. Such results indicate that the fully-solution-based strategy is promising for the fabrication of low cost, highly flexible and highly efficient PSCs.

CHAPTER 6. ALL-SOLUTION PROCESSED ULTRATHIN ORGANIC SOLAR CELLS WITH EXTRA-HIGH MECHANICAL FLEXIBILITY AND DURABILITY

Solution-processed Cu electrodes and PEDOT:PSS electrodes have been studied in previous chapters. In this chapter, these two electrodes will be combined together for all-solution-processed ultrathin OSCs. The flexibility of the OSCs will be investigated by repeated stretch-compress test based on a “pre-stretch” strategy.

6.1 Introduction

Stretchable electronics that possess unstinted conformability to highly flexible surfaces, such as the surfaces of clothes, skin and biological tissues, are of increasing interests^[216-221]. Owing to the congenital flexibility of polymer-based active layers, organic solar cells (OSCs) are promising candidates therein. Based on the well-known “wavy” strategy^[222], for example, a thin polymer active layer consists of poly(3-hexylthiophene) (P3HT) and (6,6)-phenyl-C₆₁-butyric acid methyl ester (PC₆₁BM) can sustain considerable strain without suffering from mechanical failure^[170, 223]. Apart from excellent mechanical properties, polymer active materials are low cost and solution-processable, which conform to the requirements of high throughput and large area production methods, such as roll-to-roll (R2R) process^[37, 134, 224].

Unlike soft polymer active materials, the electrode materials are always obstacles that limit the flexibility of OSCs. The indium tin oxide (ITO) transparent electrodes are extremely brittle^[225, 226], while vacuum-deposited metal back electrodes usually show poor adhesion to underneath layers^[227]. Although conductive polymer blend poly(3,4-ethylenedioxythiophene):poly(styrene sulfonate) (PEDOT:PSS) has been developed to replace ITO in some circumstances^[40, 228], exploiting the

substitute for vacuum-deposited metal electrodes is still challenging. Yet several kinds of printing techniques have been developed to fabricate metal electrodes for organic solar cells^[158, 229, 230]. The printing processes are generally fast and scalable comparing with vacuum-deposition, and the printed metal films show eligible mechanical durability and adhesiveness after sintering. However, the requirement of high temperature (>150 °C) sintering process severely limited their application on flexible organic substrates^[231, 232].

Previously, there has been some constructive works on stretchable solar cells. Kaltenbrunner et al. reported stretchable solar cells on ultrathin PET (thickness ~1.4 μm) substrates^[168]. The device showed high power conversion efficiency (PCE) and power-per-weight, but unsatisfactory mechanical durability under cyclic stretching and compressing. Very recently, high power-per-weight (23 W/g) ultrathin perovskite solar cell has been reported^[233]. Whereas the high PCE value (~12%) is impressive, the decrease of the efficiency after cyclic stretch-compress test is quite obvious even though an encapsulation layer has been applied to neutralize the surface tension.

Here, we demonstrate an all-solution strategy to fabricate organic solar cells with an inverted structure. Each layer of the device, including the polyimide (PI) substrate, is prepared by solution method, which accommodates to low-cost and scalable R2R processes. The P3HT:PC₆₁BM based device shows a PCE value of 3.2%, which we believe is the highest among all the all-solution processed solar cells based on the same active material. More significantly, the device is mechanically durable that only a slight drop (~10%) in PCE is observed after 1,000 stretch-compress cycles with a large strain of 50%.

6.2 Experimental Section

6.2.1 Materials

Polydimethylsiloxane (PDMS) Sylgard 184 was obtained from Dow Corning. A ~1% water solution of highly conductive poly(3,4-ethylenedioxythiophene):poly(styrenesulfonate) (PEDOT:PSS), Clevios PH 1000 was obtained from Heraeus Clevios. Poly(3-hexylthiophene) (P3HT) was obtained from Rieke Metals, Inc. 1-(3-methoxycarbonyl) propyl-1-phenyl[6,6]C₆₁ (PC₆₁BM) was obtained from American Dye Source, Inc. Polyimide (PI) solution was obtained from the Institute of Polymer Materials, Shanghai Jiao Tong University. Copper sulfate pentahydrate (CuSO₄·5H₂O, 99.0%) and poly(ethylene glycol) (PEG, Mw = 4000) were obtained from Uni-Chem. Potassium sodium tartrate (98%) was obtained from VWR-BDH. Potassium persulfate (K₂S₂O₈, 99.5%), ammonium tetrachloropalladate ((NH₄)₂PdCl₄, 98%), [3-(methacryloyloxy)propyl] trimethoxysilane (MPTS, 98%), 2-(methacryloyloxy)ethyl-trimethylammonium chloride (METAC, 80 wt% water solution), polyethylenimine (PEI, Mw ~ 25,000), Dimethyl sulfoxide (DMSO, 99.8%) and all other chemicals were obtained from Sigma-Aldrich. All chemicals were used as received without further purification.

6.2.2 Fabrication of Cu Bottom Electrodes

Firstly, a thin layer of PDMS (10:1 ratio) was spin-coated onto a glass slide at 3000 rpm for 1 min, then cured at 80 °C for 2 h. Afterwards, the PDMS was treated by air plasma for 30 s. A thin layer of PI (~1 μm) was formed by spin-coating the PI solution onto PDMS at 2000 rpm for 1 min, followed by curing at 200 °C for 2 h in a vacuum oven. For the reference cells, 100 nm Cu was deposited on PI by vacuum deposition to serve as bottom electrodes. For all-solution processed devices, the Cu electrodes were deposited through polymer-assisted metal deposition (PAMD). The deposition process of Cu has been reported elsewhere. Briefly, the siloxane modified methacrylate MPTS was chemically modified on PI surface by immersing the plasma-treated PI substrate into a solution that consists of 95% ethanol, 4% H₂O, 1%

acetic acid and 1% MPTS for 1 h. Then, the substrate was rinsed and immersed into a water solution containing 20 wt% METAC and 0.5 wt% $K_2S_2O_8$. The solution was heated at 80 °C for 1 h in an oven to graft 20 nm thick PMETAC by free radical polymerization. A gel-like ink containing $(NH_4)_2PdCl_4$, H_2O and PEG (weight ratio 1 : 100 : 250) was screen-printed on PMETAC-grafted PI substrate. The $PdCl_4^{2-}$ anions were immobilized by PMETAC through the electrostatic interaction with quaternary ammonium cations. Finally, the substrate was plasma-treated and rinsed, and then immersed into Cu plating bath, which consists of $CuSO_4 \cdot 5H_2O$ (6 g/L), NaOH (6 g/L), potassium sodium tartrate (14 g/L) and formaldehyde (~1 wt%). The substrate was dried by air flow and then transferred into N_2 -filled glove box once the deposition has finished. The thickness of the Cu electrodes was ~100 nm according to AFM characterization.

6.2.3 Fabrication of OSCs

The fabrication of ultrathin OSC began with modifying the Cu electrodes with a thin layer of PEI. To form a 15 nm thick PEI layer, a solution of PEI (0.5 wt% in 2-methoxyethanol) was spin-coated on the substrate at 5000 rpm for 30 s. After annealing at 100 °C for 10 min, 400 nm thick P3HT:PCBM active layer was coated atop PEI by spin-coating a chlorobenzene solution of P3HT (20 mg/mL) and $PC_{61}BM$ (16 mg/mL) at 800 rpm for 30 s. The film was then annealed at 145 °C for 5 min in N_2 -filled glove box. Finally, ~170 nm thick PEDOT:PSS film was coated on top of the active layer by spin-coating PH 1000 solution (doped with 5 wt% DMSO and 0.5 wt% Zonyl FS-300 fluorocarbon surfactant) at 1000 rpm for 60 s in air, then the substrate was transferred into glove box and annealed at 130 °C for 10 min. The fabricated device can be peeled-off from glass slide by thermal release tape (REVALPHA, Nitto Denko), which will release the attached device when heated at 120 °C for 10 s. PDMS stamps were used as temporary receiving substrates when transferring the device onto pre-stretched tape (3M VHB 4905) or other substrates that cannot be heated.

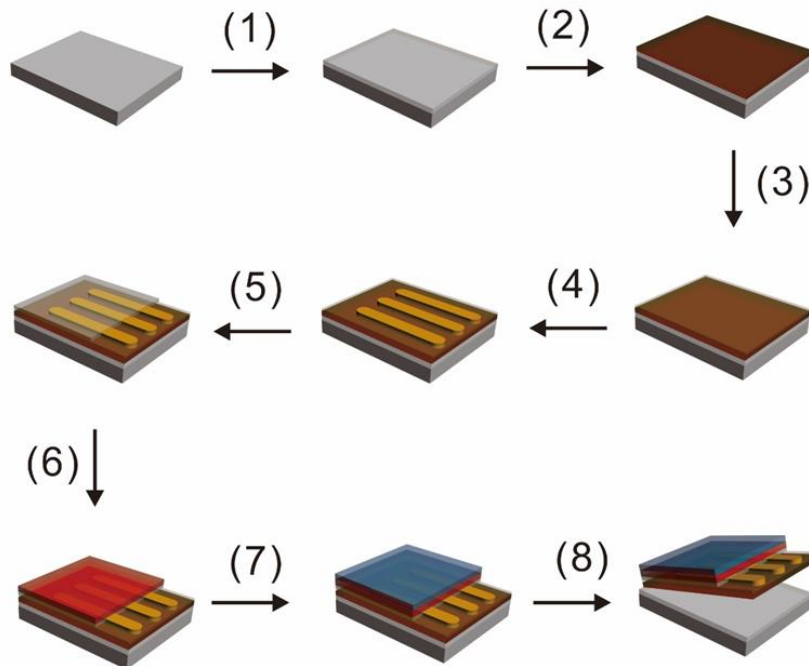
6.2.4 Characterization

AFM measurement was carried out by XE-100 atomic force microscope (Park System) using non-contact mode. I-V characteristics of the devices were recorded by a Keithley 2400 source meter, and a 100 W Oriel solar simulator (94011A, Newport, 100 mW/cm² AM 1.5 solar spectrum calibrated by a standard silicon reference cell) was used as light source.

6.3 Results and Discussions

6.3.1 Structure of All-solution-processed Organic Solar Cell

The detailed procedures for the fabrication of all-solution processed solar cells are described in Scheme 6.1. Glass slide serves as a rigid support to facilitate with the device fabrication, and a thin polydimethylsiloxane (PDMS) layer serves as interlayer between glass and PI so that the fabricated device can be peeled off from glass slide^[234]. An inverted device structure which is similar to the one in our previous work^[159] is constructed atop the PI substrate.



Scheme 6.1 Schematics of the fabrication process. (1) Spin-coating PDMS on glass substrate, curing at 80 °C for 1h; (2) Spin-coating PI precursor solution on PDMS, curing at 180 °C for 2h; (3) Surface modification of PI by PMETAC; (4) Electroless deposition of Cu strips; (5) Spin-coating of PEI, curing at 100 °C for 10 min; (6) Spin-coating of P3HT:PCBM solution, curing at 145 °C for 5 min; (7) Spin-coating of PEDOT:PSS, curing at 130 °C for 10 min; (8) Peeling-off the device for glass substrate.

The device is highly flexible since it is ultrathin ($< 2 \mu\text{m}$) and lightweight ($\sim 2 \text{ mg/cm}^2$). Hence, it is conformable to arbitrary curved surfaces, such as the surface of a glove (Figure 6.1a). PI owns the properties of good mechanical flexibility, high mechanical strength and excellent the thermal stability, and thus is considered as an ideal substrate material for flexible electronic devices^[235, 236]. Meanwhile, the solution processability of polyamic acid, which is the precursor of PI, provides a feasible way to obtain thin and smooth PI films. A smooth substrate is especially crucial for high performance devices since the overlying layers will amplify the surface roughness and

finally lead to fatal defects if the substrate is too rough^[237]. Comparing with previous work which employed ultrathin PET foils as substrates, the spin-coated PI films show lower root mean square roughness (R_q). The atomic force microscopy (AFM) characterization of the PI substrate in this work indicates an R_q of ~ 1.5 nm (Figure 6.1b), which is much smaller than that of an ultrathin PET foil (~ 12 nm)^[168].

Based on the inverted device design, ~ 100 nm Cu electrodes are deposited atop the substrate through polymer-assisted metal deposition (PAMD), which has been introduced in Chapter 4. Briefly, polyelectrolyte poly[2-(methacryloyloxy)ethyltrimethylammonium chloride] (PMETAC) is modified on PI as an anchoring polymer for PdCl_4^{2-} ion, the precursor for electroless metal deposition. Then the catalytic precursor is patterned on polymer-modified area and immobilized by the polyelectrolyte through electrostatic interaction. Finally, Cu electrodes are obtained by simply immersing the substrate into a Cu plating bath for several minutes. An HAc post-treatment was applied to etch away the oxides on the surface of the Cu electrodes^[159]. AFM characterization indicates an R_q of ~ 8.3 nm for the surface of a typical Cu strip deposited on PI through this method (Figure 6.1b). Although this result is inferior to that of a Cu strip deposited on glass slide by the same method, the Cu strip on PI is sufficiently smooth as a bottom electrode. The surface roughness is further reduced to ~ 4.5 nm after a ~ 15 nm thin layer of polyethylenimine (PEI) which not only serves as an electron transport layer (ETL) but also a surface modifier has been coated atop the Cu. The active layer consists of ~ 350 nm P3HT:PC₆₁BM, and ~ 170 nm PEDOT:PSS acts as top transparent electrode.

The PI substrate exhibits good adhesion to the underneath PDMS layer during the whole fabrication process. Neither immersing in the plating bath nor annealing at ~ 150 °C will induce buckling or shrinking of the PI film. Thus, all the steps in this fabrication are standard procedures for the fabrication of normal lab-scale thin-film devices, which are facile and reproducible. Once the fabrication has been done, the device can be detached from the rigid

support completely without causing mechanical damage.

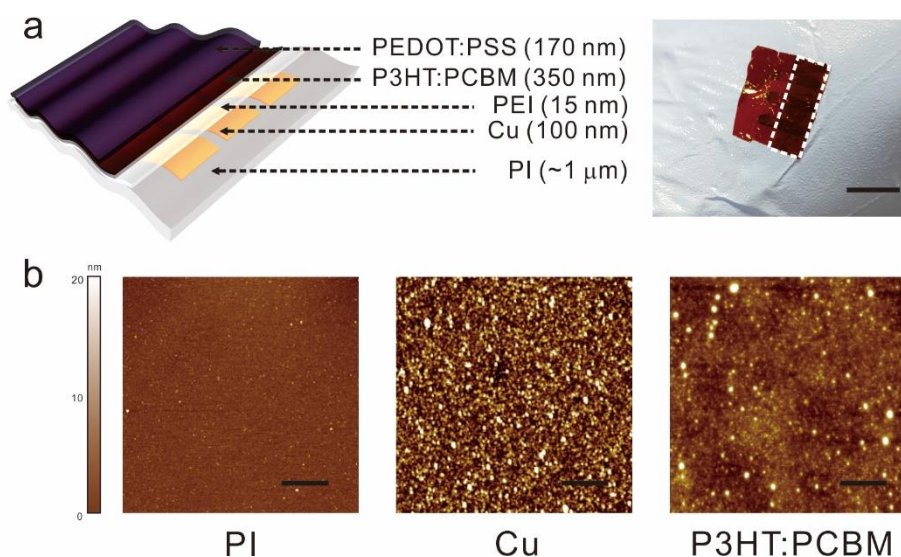


Figure 6.1 (a) Schematic illustration of the ultrathin OSC (left), and optical image of an ultrathin OSC that is attached on the surface of a glove (right). Scale bar is 1 cm. (b) AFM topographic images of PI substrate, Cu electrode, and P3HT:PCBM active layer. Scale bar is 2 μm .

6.3.2 Photovoltaic Characteristics of the All-solution Processed OSCs

The J - V characteristics of the all-solution-processed OSCs were tested before peeling-off from the rigid glass support. Figure 6.2a is the J - V curve of the champion solar cell, and the photovoltaic parameters are listed on the graph. The all-solution-processed OSC showed a V_{OC} of 0.58V, a J_{SC} of 10.0 mA/cm^2 , a FF of 52%, and a PCE of 3.02%. Such efficiency is high even comparing with other reported P3HT:PCBM OSCs based on ITO and vacuum-deposited metal electrodes. The OSC performance is also compared with a reference solar cell based on vacuum-deposited Cu electrodes with a same structure of Cu/PEI/P3HT:PCBM/PEDOT:PSS (Figure 6.2b). The reference OSC showed a V_{OC} of 0.58V, a J_{SC} of 8.45 mA/cm^2 , a FF of 54%, and a PCE of 2.65%. The all-solution-processed OSC exhibited higher PCE majorly due to the larger short-circuit current density. Apart from the photovoltaic performance, the dark current of the solar cell is also very important because it reveals the diode characteristics of the solar cell. Figure 6.2c is the logarithmic J - V curves of

all-solution-processed OSC and the reference OSC. A larger leakage current under dark state was observed from the reference OSC, indicating that the reference OSC showed inferior diode characteristics than the all-solution-processed OSC. This result proved that the interface between ELD Cu/PEI and the active layer is satisfactory.

To investigate the flexibility of the all-solution-processed ultrathin OSC, the J - V characteristics of the OSC was tested under repeated stretch and compress. A “pre-stretch” strategy is employed because the ultrathin OSC is not intrinsically stretchable. As illustrated in Figure 6.3a, the ultrathin OSC was attached on 50% pre-stretched 3M VHB 4905 tape before the test. Once the strain is released, the tape recovered to its original length, and the OSC was under 50% compress strain, accordingly. Figure 6.3b listed the current-voltage (I - V) curves of the all-solution-processed ultrathin OSC under different compress strain. The short-circuit current of the solar cell was reduced under compression, because the effective area of the solar cell is decreased. The photocurrent decreased to ~77% of the original value at 0 strain when the device was compressed to 50%. Such compression generated buckles on the surface of the solar cell rather than cracks, so the decrease in photocurrent is recoverable. To prove this, the J - V of the OSC was tested during 1,000 cycles of repeated stretch and compress, and the maximum strain was 50% for each cycle. The J - V curves of the OSC at intimal state, after 100 cycles and 1,000 cycles of stretch-compress were plotted in Figure 6.3c. The initial PCE of the all-solution-processed ultrathin OSC was 2.61%, and this value remained unchanged after 100 cycles of stretch and compress. The PCE decreased to 2.30% after 1,000 cycles of stretch and compress, which is only ~12% drop comparing with the initial efficiency. We further compare the result with that of a same-structure reference OSC based on vacuum-deposited Cu bottom electrodes (Figure 6.3d). The PCE of the reference OSC decreased dramatically after 20 cycles of stretch and compress, and lost most of the PCE after 30 cycles of stretch and compress. Such results proved that the all-solution-processed ultrathin OSC is much more robust than traditional OSC based on vacuum-deposited metal electrodes. Comparing

with previously reported stretchable OSCs, our all-solution-processed OSC showed highest retention under repeated stretch and compress^[168, 170].

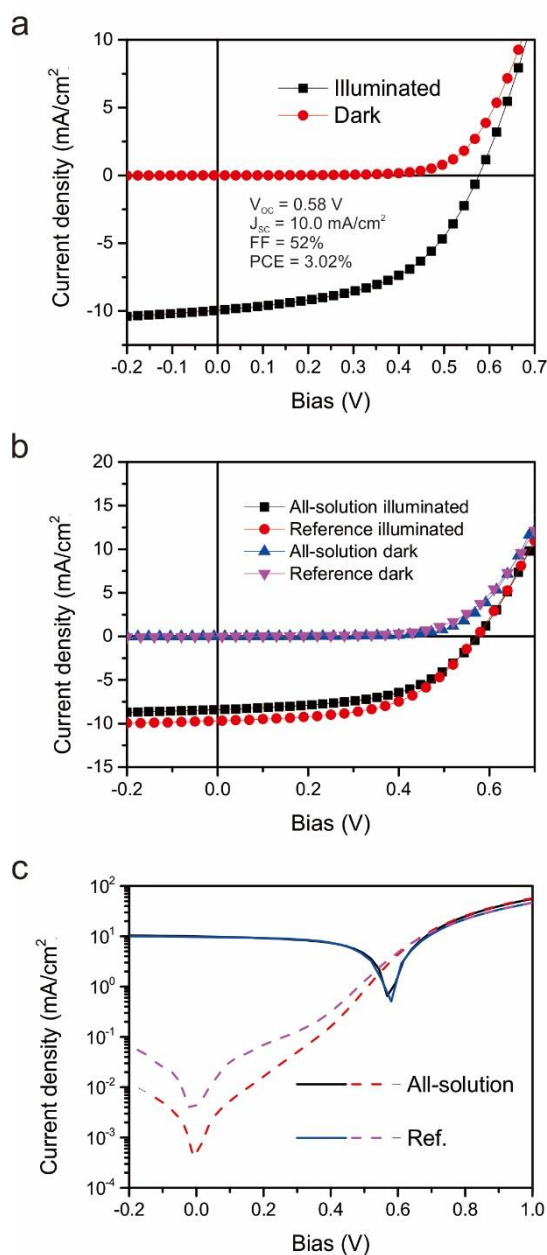


Figure 6.2 Photovoltaic performance of all-solution-processed OSCs. (a) $J-V$ curve of the champion device. (b) Comparison of all-solution-processed OSC and reference OSC which uses vacuum-deposited Cu electrodes instead of ELD Cu electrodes. (c) Logarithmic $J-V$ curves of all-solution-processed device and the reference device. The solid curves are $J-V$ curves under illuminated state, while the dash curves are $J-V$ curves under dark state.

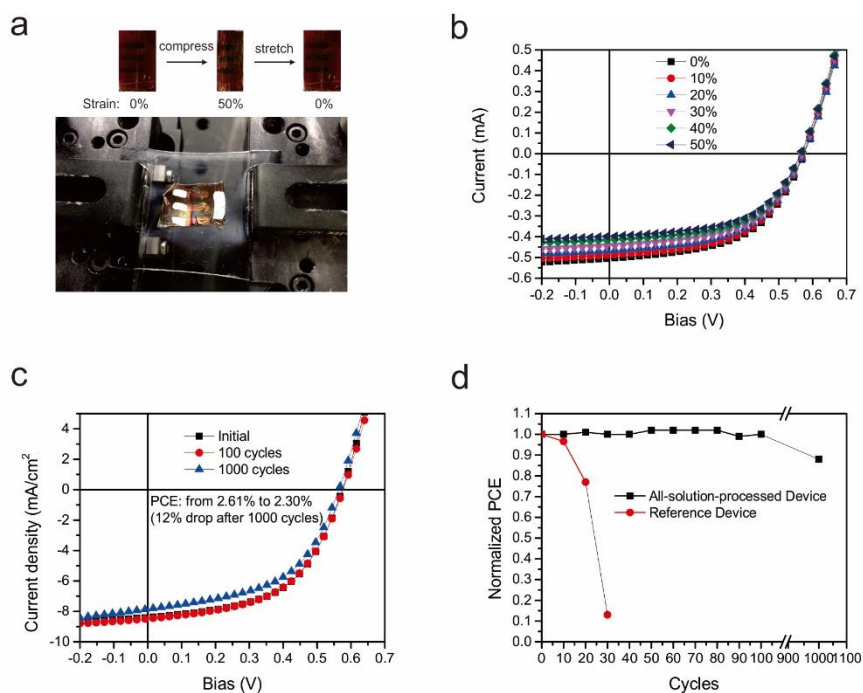


Figure 6.3 (a) Optical image of the stretch-compress system. The shape change of a device during one stretch-compress cycle is demonstrated on the top. (b) I - V curves of a device at different compress strain. (c) Comparison of the J - V curves of the all-solution-processed OSC before and after stretch and compress. (d) Normalized PCE of all-solution-processed OSC and reference OSC during 1,000 stretch-compress cycles.

6.4 Conclusions

All-solution-processed ultrathin OSC has been designed and fabricated for the first time. The substrate of the OSC is solution-processed PI film, which is ultrathin ($\sim 1\mu\text{m}$) but robust. The OSC employed ELD Cu bottom electrodes which were fabricated by PAMD method. Such solution-processed metal electrodes showed good electrical conductivity, low surface roughness, and excellent mechanical flexibility. The ultrathin OSC is lightweight and can be attached on arbitrary curved surfaces. As a proof-of-concept, stretchable OSC was demonstrated by a “pre-stretch” strategy. The all-solution-processed ultrathin OSC showed excellent PCE retention during repeated stretch-compress cycles with a maximum compress strain of 50%. The OSC remained 88% of initial PCE after 1,000 stretch-compress cycles, which is

the best among all reported stretchable OSCs. We believe that such solution-based strategy is promising for the low-cost fabrication of OSCs for flexible and wearable applications. In addition, such strategy may be versatile for the fabrication of other thin-film electronic devices such as perovskite solar cells (PSCs), dye-sensitized solar cells (DSSCs), organic light-emitting diodes (OLEDs), etc.

CHAPTER 7. BIOMIMETIC HAZE FILMS FOR EFFICIENCY ENHANCEMENT OF ORGANIC AND PEROVSKITE SOLAR CELLS

Apart from the engineering of materials and interfaces, anti-reflection and light-trapping strategies are widely employed for photovoltaic devices to improve the efficiency. In this chapter, biomimetic haze films will be investigated as both anti-reflection and light-trapping layer for OSCs and PSCs.

7.1 Introduction

Solution-processed photovoltaic devices such as organic solar cells (OSCs) and perovskite solar cells (PSCs) are promising for efficient harvesting of solar energy. In order to improve the power conversion efficiency (PCE) of these solar cells to meet the request of commercial applications, multiple approaches including optical engineering, interfacial engineering, bandgap engineering, and new material synthesis have been reported in the literature^[5, 11, 54, 192, 238, 239]. In particular, using light trapping strategies to improve the optical absorption of these solar cells has received tremendous attention recently. This is because, limited by the short carrier diffusion length, the active layer of OSCs and PSCs is often very thin^[128, 240, 241]. Such a thin active layer may lead to insufficient absorption of the incident light and lower PCE of the solar cell.

Trapping the incident light in the active layer of OSCs and PSCs can effectively improve the power conversion efficiency. This can be obtained by manufacturing light trapping structures directly in the solar cells, such as coating an anti-reflection layer^[242-244], fabricating cone-shape or V-shape device architecture^[245, 246], optimizing light-scattering texture in the transparent electrode^[247-249], and introducing plasmonic enhancement with nanostructured metal thin layer or metal nanoparticles^[250-253]. Although these

methods can improve the PCE of the solar cells effectively, they exhibit drawbacks in introducing impurity in the solar cell that is difficult to eliminate, requiring sophisticated and specialized fabrication steps, or limiting to very specifically designed active materials.

On the other hand, attaching an additional haze film on top of the light incident side of the solar cells is a very simple and effective approach to improving the light absorption over the entire optical spectrum without affecting the device fabrication process. The haze film scatters the incident light that passes through and extends its optical pathway inside the active material, which results in more efficient light absorption of the device. In addition, the haze layer enables significant decrement of the light loss when illuminated at small incident angles. For example, state-of-the-art ultrahigh haze films including nanostructured cellulose papers and thin films made of self-aggregated alumina nanowire bundles rendered 10% increase in PCE of OSCs^[254, 255]. However, the fabrication of these haze films still required tedious procedures and the use of a large amount of hazardous solvents or etchants. In addition, both cellulose papers and alumina nanowires show potential instability issues to weathering such as acid rain.

Herein, for the first time, a novel biomimetic haze film (BHF) which is manufactured by simple one-step polydimethylsiloxane (PDMS) soft lithography replication from natural rose petal's epidermal texture is introduced. The BHF integrated the advantages of high optical transmittance of PDMS and high light-diffracting ability of the semi-spherical topography of rose pedals. As a result, it exhibits ultrahigh diffusion transmittance of 97% and very high haze transmittance of 75% over the entire visible spectrum. When attached atop the OSCs and PSCs, the BHF significantly improves the PCE of OSCs and PSCs by >12% and >15%, respectively. More importantly, the BHF reduces the dependence of solar cell PCE on the incident angle of the illuminated light and thus greatly enhances the light harvesting capability of the solar cells. For example, the photocurrent of PSCs can be increased by

2.7 folds at a very small incident angle of 10°. In addition, BHF's show remarkable resistance to strong acid, which is beneficial for real solar panel application.

7.2 Experimental Section

7.2.1 Materials

Polydimethylsiloxane (PDMS) prepolymer and the curing agent (Sylgard 184) were obtained from Dow Corning. The two components were mixed under severe stirring at a mass ratio of 10:1. Then the mixture was degassed under vacuum for 10 min, and then casted atop the rose petals. Titanium (IV) isopropoxide (99.999%), niobium (V) ethoxide (99.95%), Yttrium (III) chloride (99.99%), lead (II) chloride (99.999%), methylamine solution (MAI, 33% in ethanol), hydroiodic acid (57% in water), bis(trifluoromethane)sulfonimide lithium salt (Li-TFSI, 98%), 1,8-diiodooctane (DIO, >97%) and 4-tert-butylpyridine (*t*BP, 96%) were obtained from Sigma-aldrich. Poly[$\{2,5\text{-bis(2-hexyldecyl)-2,3,5,6-tetrahydro-3,6-dioxopyrrolo[3,4-c]pyrrole-1,4-diyl}\}$ -alt- $\{2,2',5',2''\text{-terthiophene}\}$ -5,5''-diyl](PDPP3T) was obtained from Organtec Materials, Inc. 1-(3-methoxycarbonyl) propyl-1-phenyl[6,6]C₇₁ (PC₇₁BM) was obtained from American Dye Source, Inc. Poly(3,4-ethylenedioxythiophene):poly(styrenesulfonate) (PEDOT:PSS) solution PVP AI 4083 was obtained from Heraeus Clevios. Zinc oxide nanoparticles were synthesized by an adapted procedure reported elsewhere^[256]. The nanoparticle was in the size of about 5 nm, and dispersed in 2-methoxyethanol by a weight ratio of 0.5 % for the following device fabrication. The monocrystalline solar cells were provided by Dr. Jixiang Zhou and Prof. Hui Shen in Sun Yat-Sen University, China.

7.2.2 PSC fabrication

Patterned FTO/glass slides (obtained from Zhuhai Kaivo Optoelectronic Technology Co., Ltd.) were washed in ultrasonic bath of acetone, isopropanol and water for 30 min respectively. The FTO films were then cleaned with piranha solution (mixture of 98% H₂SO₄ and 30% H₂O₂, volume ratio 3:1) for 10 min. Afterwards, a solution of titanium isopropoxide (350 μ L in 5 mL ethanol, added with 5 μ L niobium (V) ethoxide) was spin-coated on the rinsed and dried FTO films at 5000 rpm for 30 s, and then annealed at 150 °C for 30 min in air. The slides were then treated with plasma for 1 min to remove the organic residues. Afterwards, the slides were transferred in a N₂-filled glove box, followed by spin-coating a perovskite solution (2.4 mol/L CH₃NH₃I and 0.8 mol/L PbCl₂ in DMF) at 2000 rpm for 1 min. After annealing at 100 °C for 90 min, a chlorobenzene solution of spiro-OMeTAD (doped with 50 μ L 520 mg/mL Li-TFSI acetonitrile solution and 72 μ L *t*BP for each 2 mL solution) was spin-coated on top of the perovskite layer. The slides were stored in dry air overnight. Finally, 100 nm Au was deposited on top of the spiro-OMeTAD layer by thermal evaporation at a rate of 0.1 nm/s.

7.2.3 OSC fabrication

The active layer solution was prepared as follows. PDPP3T:PC₆₁BM (5 mg/mL : 10 mg/mL) was firstly dissolved into *o*-dichlorobenzene (*o*DCB) and stirred at 70 °C for 5 h. Then, after the temperature of the solution was cooled down to room temperature (about 25 °C), chloroform (CF) was added, and the solution was stirred for another 1 h. At last, DIO was added in the solution, and the solution was stirred for another 20 min before use. For the ternary solvent system, *o*DCB:CF:DIO were mixed by volume ratio of 76:19:5. For the solar cell fabrication, ITO/glass was ultrasonically cleaned by acetone, ethanol, and deionized water in sequence. Then PEDOT:PSS (AI 4083) HTL was spin-coated onto the ITO at 1500 rpm for 1 min, and then annealed at 120 °C for 10 min to evaporate the solvent. The solution of PDPP3T:PC₇₁BM was spin-coated at 2500 rpm for 1 min and annealed at 80 °C for 20 min to form the active layer. The ZnO ETL was spin-coated at 1500

rpm for 30 s and dried at 80 °C for 30 min. Finally, 100 nm aluminum electrode was thermal evaporated on the ZnO layer at a rate of 0.1 nm/s for the first 20 nm and 1 nm/s for the rest.

7.2.4 Characterization

All optical measurements of the BHF except the optical reflection were performed by Agilent Cary 7000 with integrating sphere. The optical reflection was tested using Olympus USPM-RU micro spectrophotometer. A CARL ZEISS ULTRA 55 SEM was used to characterize the BHF surface and cross-sectional morphology. A Keithley 2400 source meter was used to measure the J - V curves of the solar cells, and a 300 W Oriel solar simulator (91160, Newport, 100 mW/cm², equipped with AM1.5 filter) was used as the light source. The solar simulator was calibrated by a standard silicon solar cell before J - V test. The active area of the devices was determined by the common area of top and bottom electrodes. Typically, the active area was 0.08 cm² for OSC and PSC. The EQE of the devices were measured with a standard system equipped with a xenon lamp (Oriel 66902, 300 W), a monochromator (Newport 66902), a Si detector (Oriel 76175_71580) and a dual channel power meter (Newport 2931_C).

7.3 Results and Discussions

BHFs were prepared by one-step soft lithographic molding of yellow rose petal^[257]. Briefly, PDMS and its curing agent were mixed together at a ratio of 10:1, and then casted atop the yellow rose petal. After cured at room temperature for 48 h, BHF was obtained by peeling off the textured PDMS from the surface of rose petal. This soft lithography molding replicated the epidermis pattern of rose petal onto PDMS completely. The overall thickness of the BHF was ~300 μm. The topography of BHFs showed microscale craters, which are similar to concave semi-spheres that are typically used in microlens array. In each of the microcraters, wrinkle-like sub-structures in the size of several hundred nanometers were observed, which were also

duplicated from the surface texture of rose petal (Figure 7.1b and c). The average size of closely packed microcraters was $\sim 25 \mu\text{m}$ in diameter and $\sim 20 \mu\text{m}$ in depth (Figure 7.1d).

The light-scattering mechanism of BHF is illustrated in Figure 7.1e. Because the refractive index of air ($n_{air} = 1$) is lower than that of PDMS ($n_{PDMS} \sim 1.41$), the microcrater structure (Figure 7.1d) functions as concave lens to diverge incident light that passes through. Meanwhile, the submicron wrinkles in each microcrater (Figure 7.1c) offer additional anti-reflection functionality to the underlying substrate^[258, 259]. As a proof-of-concept of the remarkable haze effect, the BHF was placed above a paper printed with a “Haze” logo. When directly attached to the paper, the haze effect was not obvious because the distance between the textured surface and the logo was too low. However, the logo could not be observed when the BHF was lifted 1 cm away from the paper (Figure 7.1f).

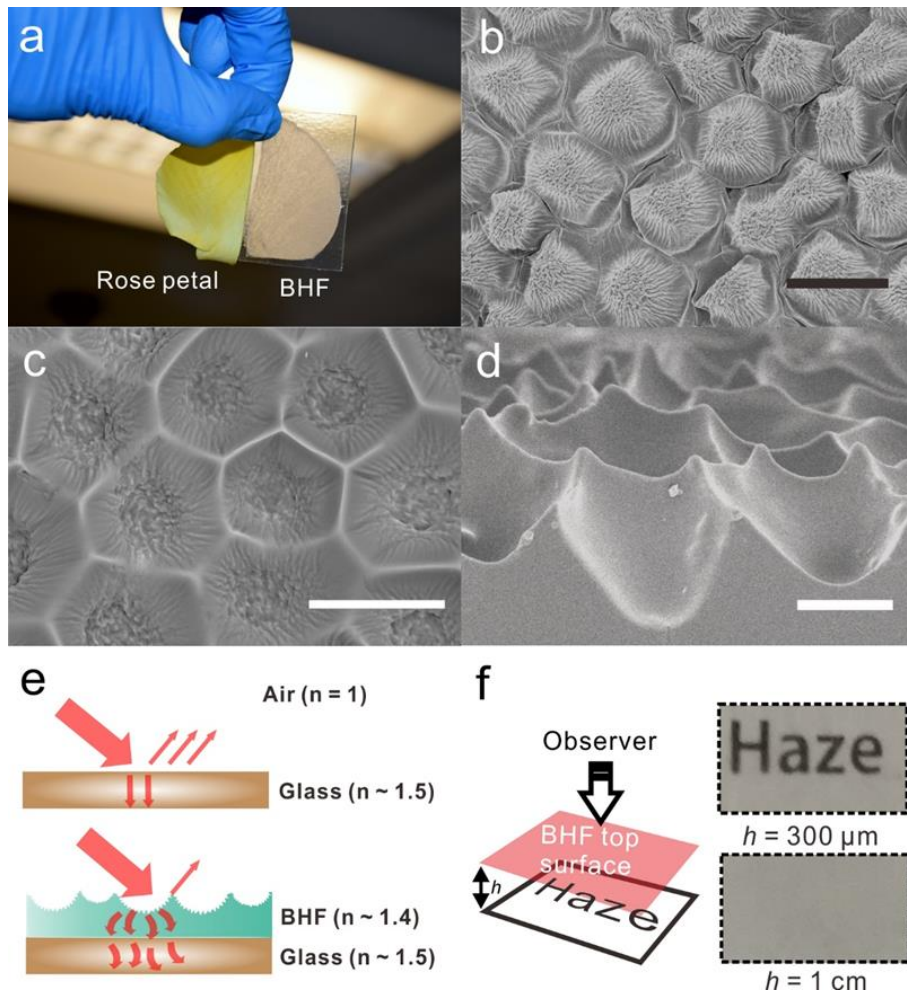


Figure 7.1 (a) Optical image of rose petal and BHF. SEM images of the top surface of rose petal (b) and textured surface of BHF (c). Scale bar is $30 \mu\text{m}$ for each graph. (d) SEM cross-sectional image of the BHF. Scale bar is $10 \mu\text{m}$. (e) Illustration of the light-scattering and anti-reflection mechanism of the BHF. (f) Illustration of the haze effect of the BHF. As shown in the scheme, the BHF (thickness = $300 \mu\text{m}$) was placed above a paper printed with the word “Haze”, where h represents the distance between the paper surface and the textured surface of the BHF.

Optical measurements, including the diffusion/haze transmittance and the angular distribution of the scattering light power, were carried out to quantitatively evaluate the haze ability of BHF. The diffusion transmittance refers to the ratio of the total power of transmitted light to the power of incident light, while the haze transmittance is the percentage of the light scattered by BHF among the total transmitted light. These two parameters

demonstrate the haze ability from the perspective of optical power. A commonly used optical measuring setup is illustrated in Figure 7.2a, where a spectrophotometer with an integration sphere was used to collect the transmitted light in every spatial direction to obtain the diffusion transmittance while the transmitted light parallel to the incident light was absorbed by the optical absorber. The BHF presented ultrahigh diffusion transmittance of 97% over the entire testing spectrum ranging from 400 nm to 800 nm. More significantly, the BHF also possessed ultrahigh haze transmittance of 75% at the same range. Compared with other reports in the literature (Figure 7.3), the BHF has a very high haze value as well as the highest diffusion transmittance.

The variation of the haze transmittance by angle was further studied in detail, by using the system illustrated in Figure 7.2c. A photodetector which moved along a circular path was employed to collect the scattering light that passed through the BHF. The light intensity between the photodetector and the BHF was measured at different angles, where the perpendicular direction to the BHF was defined as 0° . As demonstrated in Figure 7.2d, the angular distribution of the transmitted light changed very little over the entire visible spectrum region (400 ~ 800 nm), which further indicates that the haze effect of the BHF is not wavelength-dependent. Thus, the BHF is versatile for most of the solar cell applications. More importantly, the intensity of the scattering light remained over 10% of the maximum value over a spatial angle as large as 56° (Figure 7.2e). This is critical for enhancing the light-harvesting of solar cells at small incident angles, which will be demonstrated in detail in a later section.

As a result, the BHF was assumed to be ideal for photovoltaic applications by weakening the reflection loss and strengthening the absorption efficiency of photovoltaic devices at the same time. In the following, we applied the BHF on the photovoltaic material (silicon), and devices (organic solar cells and perovskite solar cells) to demonstrate its effectiveness in absorption enhancement. As a common solar material, silicon loses a lot of light

absorption by surface reflection due to its high refractive indices (n ranges from ~ 3.7 to 5.6 between 400 to 800 nm^[17]). Anti-reflection coating and nano-structure were applied to reduce the surface reflection and improve absorption in previous works^[260, 261]. Our BHF, on the other hand, provides a low-cost and facile approach to realize the anti-reflection function. As illustrated in Figure 7.2f, a flat PDMS film increased the absorption of Si wafer by $\sim 10\%$, while the BHF improved the absorption by $13\% \sim 15\%$. Based on these results, we assume that the BHF improve the absorption of Si wafer through two aspects. On one hand, the BHF is made of low refractive PDMS, which reduced the light reflection and preserved more light power for the absorptive material. On the other hand, the textured BHF scattered the incident light, and thus lengthened optical paths inside the Si absorber for more efficient absorption. It is notable that the optical thickness of Si wafer is high enough for sufficient absorption, so the absorption enhancement was mainly attributed to the anti-reflection effect from the BHF. A 6.8% improvement in PCE was obtained by attaching the BHF atop a Si solar cell, indicating a remarkable enhancement in light absorption with the help of BHF (Table 7.1).

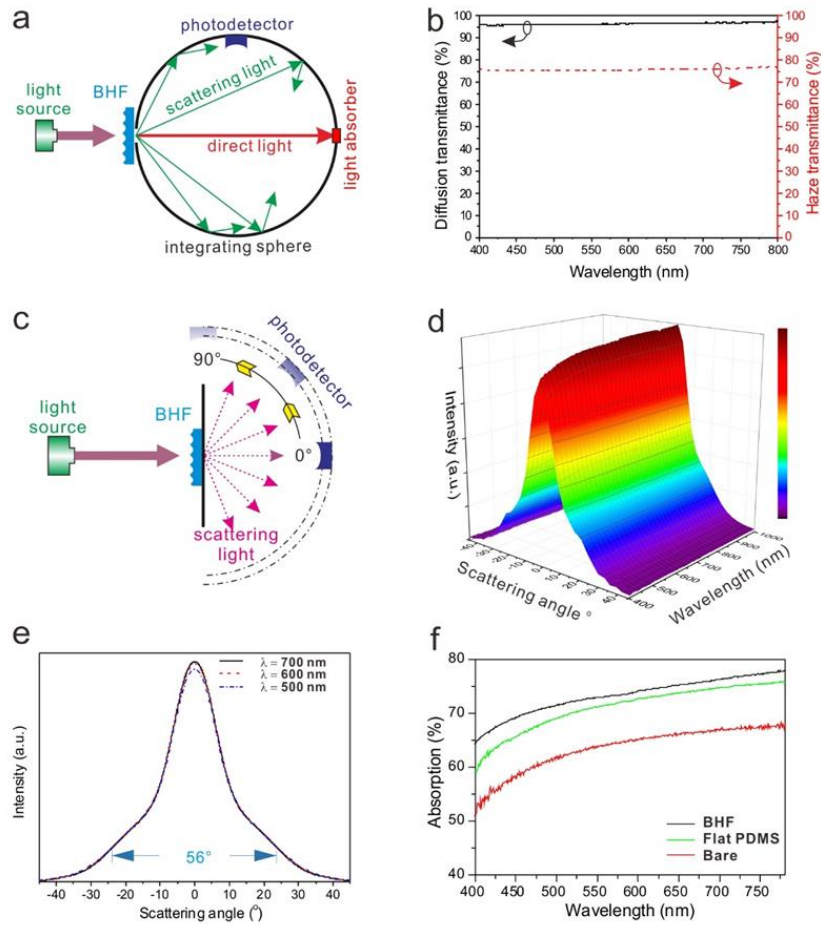


Figure 7.2 (a) The experimental setup for diffusion and haze transmittance measurement (b) The UV-Vis absorption spectra of diffusion and absorption haze. (c) and (d) The schematic diagram of experimental setup for scattering light power angular distribution measurement, and the corresponding results tested between wavelength range of 400 ~ 800 nm, respectively. (e) Scattering light power angular distribution of BHF at specific 3 wavelengths, 500nm, 600nm and 700nm. (f) The absorption spectra of bare Si wafer, flat PDMS film-covered Si wafer, and BHF-covered Si wafer.

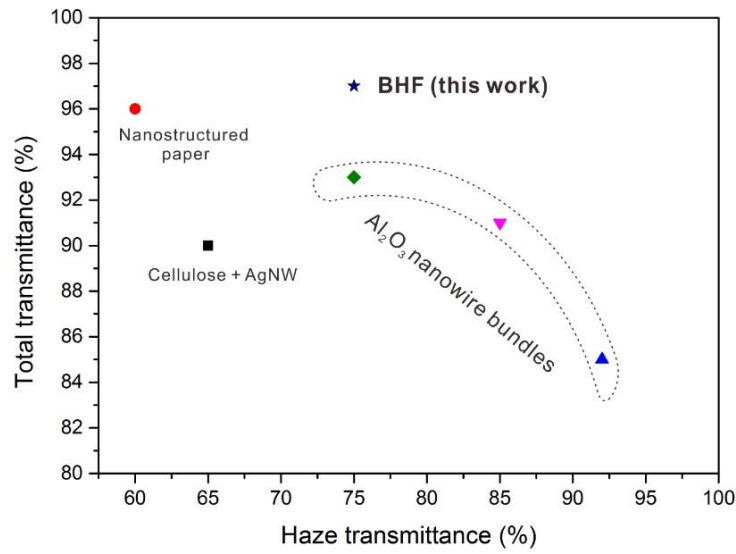


Figure 7.3 The comparison of average haze and diffusion transmittance of reported haze films and BHF from 400 nm to 800 nm. Details are listed in Table 7.2.

Table 7.1. Photovoltaic characteristics of c-Si solar cells, OSCs and PSCs with and without BHF.

Device Type	Device Structure	J_{sc} (mA/cm ²)	V_{oc} (V)	FF (%)	PCE (%)
c-Si	Bare	37.9	0.58	72.7	16.0
	With flat PDMS	37.6	0.58	72.4	15.8
	With BHF	40.4	0.58	72.8	17.1
PSC	Bare	20.8	1.03	77.6	16.6
	With flat PDMS	21.4	1.03	74.8	16.5
	With BHF	24.5	1.03	75.9	19.2
OSC	Bare	10.5	0.70	60.7	4.46
	With flat PDMS	10.8	0.70	60.8	4.60
	With BHF	11.9	0.70	60.7	5.06

Table 7.2. Comparison of optical haze and transmittance for some typical haze materials reported previously.

Materials	Haze value @400-800nm	Total Transmittance
ZnO:Al ^[262]	~30%	N.A.
Nanofibrillated cellulose+Ag nanowire ^[263]	63~70%, 65% on average	~90%
Nanostructured paper ^[264]	~60%	~96%
TiO ₂ ^[265]	55%~75%	N.A.
Pyramidal type SnO ₂ :F (FTO) ^[266]	5%~30%,18% on average	N.A.
w-Textured SnO ₂ :F (FTO) ^[266]	50%~85%,70% on average	N.A.
Alumina nanowire bundles A ^[267]	92%	~85%
Alumina nanowire bundles B ^[267]	85%	~91%
Alumina nanowire bundles C ^[267]	75%	~93%
Wood composites ^[264]	~80%	~90%
BHF PDMS (this work)	>75%	~97%

Comparing with Si solar cells, thin-film solar cells could benefit more from the scattering effect since the thickness of their active layers is always too thin to fully absorb the incident light. The insufficient active layer thickness is basically due to the low exciton diffusion length of such active materials. Hence, improve the light trapping through the scattering effect of BHF is especially promising for thin-film photovoltaics. To evaluate the utility of BHF on thin-film devices, we fabricated thin-film solar cells based on organolead halide perovskite absorber through low-temperature solution processes. As illustrated in Figure 7.4a, the perovskite solar cell employed a traditional planar structure^[11]. The champion device showed an open-circuit voltage (V_{OC}) of 1.03 V, a short-circuit current density (J_{SC}) of 20.8 mA/cm², a fill factor (FF) of 77.6% and a high PCE value of 16.6%. We further measured the current density-voltage ($J-V$) characteristics of the device attached with BHF. As expected, the PCE improved dramatically with the help of BHF. The high J_{SC} of 24.5 mA/cm², which was ~18% larger than that of the bare device, strongly indicated a more thorough absorption of incident light. The PCE value of the device also boosted to 19.2%, which is 15.6% higher than that of the bare device (Figure 7.4b). Afterwards, another 9 randomly selected devices were tested with and without the BHF. All the devices showed significant improvement on device performance with the aid

of BHF, and the average enhancement in PCE value was 12.3%. OSCs based on PDPP3T:PC₇₁BM active material were also tested with and without BHF (Figure 7.4b and Table 7.1). It is worth noting that the PSC enjoyed a larger extent of photocurrent density enhancement than OSC, probably due to the more efficient photon recycling process in PSC^[54, 126]. The external quantum efficiency (EQE) data also indicated the improvement of photocurrent (Figure 7.4c). The calculated current density of PSC from the EQE data increased from 19.7 mA/cm² to 22.1 mA/cm², showing an enhancement of 12.2%. As mentioned above, our BHF also provides a more stable device performance versus varied light incident angle. In case of setting the photocurrent of perpendicularly illuminated devices (Figure 7.4d) as the benchmark, the photocurrent of the PSC devices with BHF maintained ~90% at an incident angle of 50° (40° in Figure 7.4d), and ~65% of maximum power conversion efficiencies still exist even at a very small incident angle of 10° (80° in Figure 7.4d). On the contrary, the photocurrent of the bare devices decreased dramatically once the incident angle went down. Such advantage of BHF based devices results from the large light scattering angle of the BHF, as discussed before. For real application, the BHF is supposed to survive after weathering such as acid rain. Hence, an acid treatment of the BHF was demonstrated by immersing the BHF in a diluted HCl solution with a pH value of 1, which is far more extreme than that of acid rain (pH ~ 5). The performance of BHF-enhanced PSCs remained unchanged before and after the treatment of BHF, indicating a stable optical performance of the BHF in acidic environment.

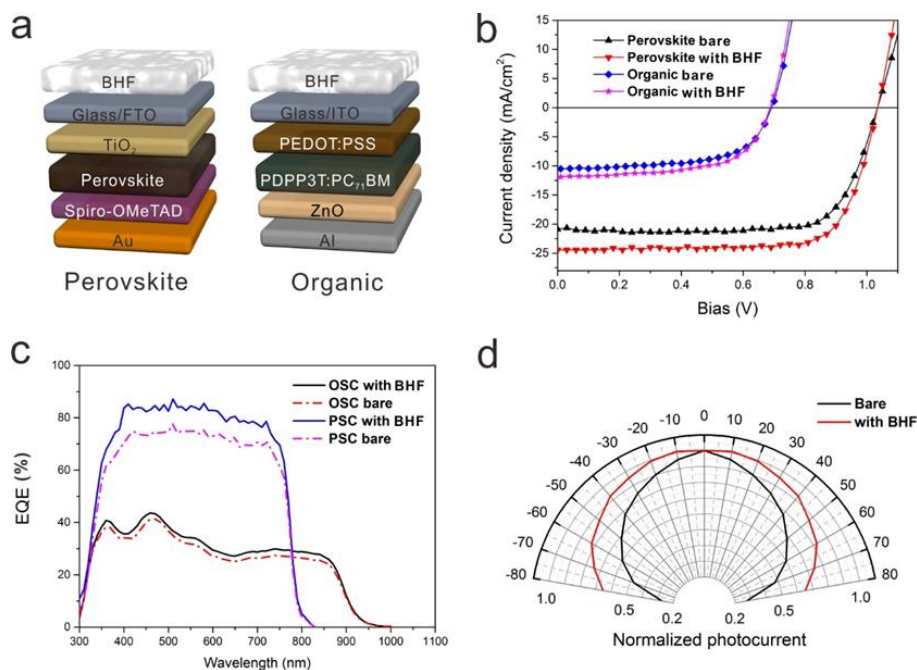


Figure 7.4 (a) Structural illustration of BHF-enhanced PSC and OSC. The BHF can be attached and detached at any time. (b) J - V curves comparison of the best solar cells with and without BHF. (c) EQE spectra of solar cells w/ and w/o BHF. (d) The normalized photocurrent values of PSCs w/ and w/o BHF versus the complementary angle of the incident light (i.e., 0 means the incident angle is 90°).

7.4 Conclusions

In summary, we demonstrate a low-cost, bio-inspired, high haze film by duplicating the surface texture of rose petals with PDMS. The Soft lithography replication method we used to duplicate the haze texture is fast, scalable and cost-efficient comparing with those top-down lithography and bottom-up growth method for micro- or nanotextures. This film possesses ultra-high transmission haze of 75% and high diffusion transmittance of 97%. Over 15% improvement of the power conversion efficiency of perovskite solar cell was obtained by simply attaching the haze film on the glass substrate. We believe that such advantages will make our BHF a promising enhancing accessory for existed photovoltaic devices. In addition, the haze film enhanced solar cells can maintain high power output even at very small incident angle, leading to more efficient light harvesting, especially for those

devices settled at high latitude areas. Such enhancement is of the best results among all the published works using micro- or nanostructures to enhance light absorption of solar cells, and more importantly, the ease of fabrication, flexible and detachable natures of our BHF provide capacious space of application on various types of photovoltaic devices.

CHAPTER 8. CONCLUSIONS AND OUTLOOK

8.1 Conclusions

In this thesis, fully-solution-based strategies have been investigated for the fabrication of highly efficient PSCs and OSCs. The physical and chemical properties of solution-processed Cu and PEDOT:PSS electrodes are characterized by multiple technologies. The performance of the solar cells is characterized by *J-V* and EQE measurement, and the mechanical flexibility of the solar cells is evaluated by repeated bending or stretch-compress test. In addition, BHF is fabricated and characterized as anti-reflection and light-trapping layer for the absorption enhancement of OSCs and PSCs.

In chapter 4, PAMD was studied as a solution-based technique for the fabrication of Cu electrodes. The fundamental chemistry of PAMD was discussed, and two patterning strategies, PCP and PFP, were illustrated and compared. Cu thin films were deposited on multiple substrates to study the versatility of PAMD. The surface topography and thickness of the Cu electrodes were characterized by AFM, and the chemical composition of the Cu electrodes was analyzed by XPS. The thickness of Cu electrodes prepared by PCP method was determined to be ~100 nm, which is suitable for solar cell applications. Moreover, the surface roughness of Cu electrodes fabricated by PCP method was ~4 nm, which is ideal for bottom electrode applications.

In chapter 5, n-PEDOT:PSS was investigated as transparent electrodes for fully-solution-processed TCO-free st-PSCs. The sheet resistance of 50 nm-thick n-PEDOT:PSS film was $38 \Omega/\square$, and the optical transmittance of n-PEDOT:PSS at 550 nm was ~85%. The n-PEDOT:PSS was found to be printable by a simple dry transfer technique, and thus is suitable moisture-sensitive PSCs. *J-V* and EQE characteristics of the TCO-free st-PSCs were compared with ITO-based reference PSCs. The PCE of standalone TCO-free st-PSC was 13.9%, which is one of the highest among all reported TCO-free

PSCs. Furthermore, the st-PSCs were combined with c-Si solar cells as 4-terminal tandem solar cells, and the overall PCE of TCO-free st-PSC/c-Si tandem solar cell was 19.2%. In addition, flexible st-PSCs were fabricated on PET and ultrathin PI substrates to investigate the flexibility of n-PEDOT:PSS based solar cells. The retention of TCO-free@PET was 90% after 1,000 bending cycles at a radius of 5 mm, which is one of the best among all reported flexible PSCs.

In chapter 6, all-solution-processed OSCs were fabricated on solution-processed ultrathin PI substrate for the first time. Solution-processed Cu electrodes and PEDOT:PSS electrodes were integrated together in the OSC. The surface topography of each layer in the OSC was characterized by AFM to study the interfaces. The J-V characteristics of the all-solution-processed OSCs were compared with a vacuum-deposited Cu electrode based reference devices. The best all-solution-processed OSC showed 3.01% PCE, which is higher than that of the reference device. More importantly, the all-solution-processed OSC were highly flexible that ~88% of its initial PCE was maintained after 1,000 cycles of repeated stretch and compress on a 50% pre-stretched elastomer. This result is the best among all reported stretchable OSCs.

In chapter 7, BHF was developed as an absorption-enhancing accessory for OSCs and PSCs. The BHF was fabricated by one-step soft lithography replication of rose petals. The micro- and nanostructured surface texture of rose petal and BHF were studied by SEM. The haze effect of the BHF was investigated by multiple optical characterizations. These characterizations revealed that the haze film exhibited very high haze (~75%) while showing ultrahigh optical transmittance (~97%). As a result, the BHF enhanced the PCE of the champion OSC and PSC for 13.5% and 15.6%, respectively. In addition, the BHF reduced the angular dependence of the solar cells on incident light significantly, which is important for solar cell applications on high latitude areas.

8.2 Outlooks

This research has demonstrated solution-processed Cu and PEDOT:PSS electrodes, and their applications on OSCs and PSCs. Although several examples of OSCs and PSCs have been illustrated in this thesis, detailed studies and further development of these solution-based technologies need to be done in the future. For example:

1. PSCs based on solution-processed Cu bottom electrodes haven't been studied. Although fully-solution-processed st-PSC based on n-PEDOT:PSS electrodes has been fabricated successfully, the relatively low conductivity of the polymer conductor limited the PCE of the PSCs. Hence, highly conductive solution-processed Cu bottom electrodes are essential for high performance TCO-free flexible PSCs.
2. Although the OSCs and PSCs in this work were fabricated by solution processes, they all employed spin-coating technique, which is not compatible with large-scale R2R process. Future work need to focus on scalable solution processes such as doctor-blading, slot-die coating, etc.
3. The long-term stability of the solar cells is very important. Although the mechanical durability of the flexible OSCs and PSCs has been investigated by multiple method, the long-term stability of the solar cells hasn't been studied yet. Since the perovskite and organic active materials are usually unstable in air, effective encapsulation technologies that isolate the devices from air are required. In the meantime, the flexibility of the devices shouldn't be reduced by the encapsulation.

REFERENCES

- [1] S. Bai, N. Sakai, W. Zhang, Z. Wang, J. T.-W. Wang, F. Gao, H. J. Snaith, *Chem. Mater.* **2016**, *29*, 462.
- [2] A. Hagfeldt, G. Boschloo, L. Sun, L. Kloo, H. Pettersson, *Chem. Rev.* **2010**, *110*, 6595.
- [3] B. O'regan, M. Grätzel, *Nature* **1991**, *353*, 737.
- [4] S. Mathew, A. Yella, P. Gao, R. Humphry-Baker, B. F. Curchod, N. Ashari-Astani, I. Tavernelli, U. Rothlisberger, M. K. Nazeeruddin, M. Grätzel, *Nature chemistry* **2014**, *6*, 242.
- [5] Y.-J. Cheng, S.-H. Yang, C.-S. Hsu, *Chem. Rev.* **2009**, *109*, 5868.
- [6] D. Wöhrle, D. Meissner, *Adv. Mater.* **1991**, *3*, 129.
- [7] A. Kyaw, X. Sun, C. Jiang, G. Lo, D. Zhao, D. Kwong, *Appl. Phys. Lett.* **2008**, *93*, 221107.
- [8] A. Kojima, K. Teshima, Y. Shirai, T. Miyasaka, *J. Am. Chem. Soc.* **2009**, *131*, 6050.
- [9] J. M. Ball, M. M. Lee, A. Hey, H. J. Snaith, *Energy Environ. Sci.* **2013**, *6*, 1739.
- [10] W. S. Yang, B.-W. Park, E. H. Jung, N. J. Jeon, Y. C. Kim, D. U. Lee, S. S. Shin, J. Seo, E. K. Kim, J. H. Noh, *Science* **2017**, *356*, 1376.
- [11] H. Zhou, Q. Chen, G. Li, S. Luo, T.-b. Song, H.-S. Duan, Z. Hong, J. You, Y. Liu, Y. Yang, *Science* **2014**, *345*, 542.
- [12] M. A. Green, Y. Hishikawa, E. D. Dunlop, D. H. Levi, J. Hohl-Ebinger, A. W. Y. Ho-Baillie, *Prog. Photovoltaics* **2018**, *26*, 3.
- [13] J. Zhao, A. Wang, M. A. Green, F. Ferrazza, *Appl. Phys. Lett.* **1998**, *73*, 1991.
- [14] W. Zeng, L. Shu, Q. Li, S. Chen, F. Wang, X. M. Tao, *Adv. Mater.* **2014**, *26*, 5310.
- [15] W. S. Wong, A. Salleo, *Flexible electronics: materials and applications*, Vol. 11, Springer Science & Business Media, 2009.
- [16] J. A. Rogers, T. Someya, Y. Huang, *Science* **2010**, *327*, 1603.
- [17] M. A. Green, M. J. Keevers, *Progress in Photovoltaics: Research and Applications* **1995**, *3*, 189.
- [18] S. H. Liao, H. J. Jhuo, Y. S. Cheng, S. A. Chen, *Adv. Mater.* **2013**, *25*, 4766.
- [19] S. D. Stranks, G. E. Eperon, G. Grancini, C. Menelaou, M. J. Alcocer, T. Leijtens, L. M. Herz, A. Petrozza, H. J. Snaith, *Science* **2013**, *342*, 341.
- [20] C. Lungenschmied, G. Dennler, H. Neugebauer, S. N. Sariciftci, M. Glatthaar, T. Meyer, A. Meyer, *Sol. Energy Mater. Sol. Cells* **2007**, *91*, 379.
- [21] J. You, Z. Hong, Y. M. Yang, Q. Chen, M. Cai, T.-B. Song, C.-C. Chen, S. Lu, Y. Liu, H. Zhou, Y. Yang, *ACS Nano* **2014**, *8*, 1674.
- [22] C. Bi, B. Chen, H. Wei, S. DeLuca, J. Huang, *Adv. Mater.* **2017**, *29*, 1605900.
- [23] F. Di Giacomo, A. Fakharuddin, R. Jose, T. M. Brown, *Energy Environ. Sci.* **2016**, *9*, 3007.
- [24] T. Minami, *Semicond. Sci. Technol.* **2005**, *20*, S35.
- [25] D. S. Ginley, C. Bright, *MRS Bull.* **2000**, *25*, 15.
- [26] H. Kim, C. Gilmore, A. Pique, J. Horwitz, H. Mattoussi, H. Murata, Z. Kafafi, D. Chrisey, *J. Appl. Phys.* **1999**, *86*, 6451.
- [27] M. Mizunashi, *Thin Solid Films* **1980**, *70*, 91.
- [28] H. Kim, J. Horwitz, G. Kushto, A. Pique, Z. Kafafi, C. Gilmore, D. Chrisey, *J. Appl. Phys.* **2000**, *88*, 6021.
- [29] K. Alzoubi, M. M. Hamasha, S. Lu, B. Sammakia, *Journal of Display Technology* **2011**, *7*, 593.
- [30] Z. Chen, B. Cotterell, W. Wang, E. Guenther, S.-J. Chua, *Thin Solid Films* **2001**, *394*, 201.

- [31] J. Wu, H. A. Becerril, Z. Bao, Z. Liu, Y. Chen, P. Peumans, *Appl. Phys. Lett.* **2008**, *92*, 237.
- [32] K. S. Kim, Y. Zhao, H. Jang, S. Y. Lee, J. M. Kim, K. S. Kim, J.-H. Ahn, P. Kim, J.-Y. Choi, B. H. Hong, *Nature* **2009**, *457*, 706.
- [33] J.-Y. Lee, S. T. Connor, Y. Cui, P. Peumans, *Nano Lett.* **2008**, *8*, 689.
- [34] L. Hu, H. Wu, Y. Cui, *MRS Bull.* **2011**, *36*, 760.
- [35] A. Hübler, B. Trnovec, T. Zillger, M. Ali, N. Wetzold, M. Mingeback, A. Wagenpfahl, C. Deibel, V. Dyakonov, *Adv. Energy Mater.* **2011**, *1*, 1018.
- [36] L. Cattin, M. Morsli, F. Dahou, S. Y. Abe, A. Khelil, J. Bernède, *Thin Solid Films* **2010**, *518*, 4560.
- [37] F. C. Krebs, T. Tromholt, M. Jørgensen, *Nanoscale* **2010**, *2*, 873.
- [38] K. Hwang, Y. S. Jung, Y. J. Heo, F. H. Scholes, S. E. Watkins, J. Subbiah, D. J. Jones, D. Y. Kim, D. Vak, *Adv. Mater.* **2015**, *27*, 1241.
- [39] M. Hösel, R. R. Søndergaard, M. Jørgensen, F. C. Krebs, *Energy Technology* **2013**, *1*, 102.
- [40] Y. H. Kim, C. Sachse, M. L. Machala, C. May, L. Müller-Meskamp, K. Leo, *Adv. Funct. Mater.* **2011**, *21*, 1076.
- [41] M. Vosgueritchian, D. J. Lipomi, Z. Bao, *Adv. Funct. Mater.* **2012**, *22*, 421.
- [42] T. Brown, J. Kim, R. Friend, F. Cacialli, R. Daik, W. Feast, *Appl. Phys. Lett.* **1999**, *75*, 1679.
- [43] J. Y. Kim, K. Lee, N. E. Coates, D. Moses, T.-Q. Nguyen, M. Dante, A. J. Heeger, *Science* **2007**, *317*, 222.
- [44] A. Nardes, M. Kemerink, R. Janssen, *Physical Review B* **2007**, *76*, 085208.
- [45] A. Sandström, H. F. Dam, F. C. Krebs, L. Edman, *Nat. Comm.* **2012**, *3*, ncomms2002.
- [46] C. N. Hoth, S. A. Choulis, P. Schilinsky, C. J. Brabec, *Adv. Mater.* **2007**, *19*, 3973.
- [47] H. Sirringhaus, T. Kawase, R. Friend, T. Shimoda, M. Inbasekaran, W. Wu, E. Woo, *Science* **2000**, *290*, 2123.
- [48] F. C. Krebs, M. Jørgensen, K. Norrman, O. Hagemann, J. Alstrup, T. D. Nielsen, J. Fyenbo, K. Larsen, J. Kristensen, *Sol. Energy Mater. Sol. Cells* **2009**, *93*, 422.
- [49] X. Crispin, F. Jakobsson, A. Crispin, P. Grim, P. Andersson, A. Volodin, C. Van Haesendonck, M. Van der Auweraer, W. R. Salaneck, M. Berggren, *Chem. Mater.* **2006**, *18*, 4354.
- [50] W. Gaynor, G. F. Burkhard, M. D. McGehee, P. Peumans, *Adv. Mater.* **2011**, *23*, 2905.
- [51] Y. Yu, C. Yan, Z. Zheng, *Adv. Mater.* **2014**, *26*, 5508.
- [52] T. A. Berhe, W.-N. Su, C.-H. Chen, C.-J. Pan, J.-H. Cheng, H.-M. Chen, M.-C. Tsai, L.-Y. Chen, A. A. Dubale, B.-J. Hwang, *Energy Environ. Sci.* **2016**, *9*, 323.
- [53] J. You, L. Dou, K. Yoshimura, T. Kato, K. Ohya, T. Moriarty, K. Emery, C.-C. Chen, J. Gao, G. Li, *Nat. Comm.* **2013**, *4*, 1446.
- [54] D. P. McMeekin, G. Sadoughi, W. Rehman, G. E. Eperon, M. Saliba, M. T. Hörantner, A. Haghighirad, N. Sakai, L. Korte, B. Rech, *Science* **2016**, *351*, 151.
- [55] G. E. Eperon, V. M. Burlakov, A. Goriely, H. J. Snaith, *ACS Nano* **2013**, *8*, 591.
- [56] Y. Sun, J. H. Seo, C. J. Takacs, J. Seifert, A. J. Heeger, *Adv. Mater.* **2011**, *23*, 1679.
- [57] Y. Wu, X. Yang, H. Chen, K. Zhang, C. Qin, J. Liu, W. Peng, A. Islam, E. Bi, F. Ye, *Appl. Phys. Exp.* **2014**, *7*, 052301.
- [58] O. Malinkiewicz, A. Yella, Y. H. Lee, G. M. Espallargas, M. Graetzel, M. K. Nazeeruddin, H. J. Bolink, *Nat. Photon.* **2014**, *8*, 128.

- [59] H.-S. Kim, C.-R. Lee, J.-H. Im, K.-B. Lee, T. Moehl, A. Marchioro, S.-J. Moon, R. Humphry-Baker, J.-H. Yum, J. E. Moser, M. Gratzel, N.-G. Park, *Scientific reports* **2012**, *2*, 591.
- [60] D. Liu, J. Yang, T. L. Kelly, *J. Am. Chem. Soc.* **2014**, *136*, 17116.
- [61] K. Yan, Z. Wei, J. Li, H. Chen, Y. Yi, X. Zheng, X. Long, Z. Wang, J. Wang, J. Xu, *Small* **2015**, *11*, 2269.
- [62] D. Morel, A. Ghosh, T. Feng, E. Stogryn, P. Purwin, R. Shaw, C. Fishman, *Appl. Phys. Lett.* **1978**, *32*, 495.
- [63] C. W. Tang, *Appl. Phys. Lett.* **1986**, *48*, 183.
- [64] P. Peumans, S. Uchida, S. R. Forrest, *Nature* **2003**, *425*, 158.
- [65] Y. Cui, H. Yao, B. Gao, Y. Qin, S. Zhang, B. Yang, C. He, B. Xu, J. Hou, *J. Am. Chem. Soc.* **2017**, *139*, 7302.
- [66] F. Padinger, R. S. Rittberger, N. S. Sariciftci, *Adv. Funct. Mater.* **2003**, *13*, 85.
- [67] N. D. Treat, M. A. Brady, G. Smith, M. F. Toney, E. J. Kramer, C. J. Hawker, M. L. Chabynyc, *Adv. Energy Mater.* **2011**, *1*, 82.
- [68] B. Kadem, W. Cranton, A. Hassan, *Org. Electron.* **2015**, *24*, 73.
- [69] M. T. Dang, L. Hirsch, G. Wantz, *Adv. Mater.* **2011**, *23*, 3597.
- [70] Y. Sun, C. J. Takacs, S. R. Cowan, J. H. Seo, X. Gong, A. Roy, A. J. Heeger, *Adv. Mater.* **2011**, *23*, 2226.
- [71] N. J. Jeon, J. H. Noh, W. S. Yang, Y. C. Kim, S. Ryu, J. Seo, S. I. Seok, *Nature* **2015**, *517*, 476.
- [72] G. E. Eperon, S. D. Stranks, C. Menelaou, M. B. Johnston, L. M. Herz, H. J. Snaith, *Energy Environ. Sci.* **2014**, *7*, 982.
- [73] L. Protesescu, S. Yakunin, M. I. Bodnarchuk, F. Krieg, R. Caputo, C. H. Hendon, R. X. Yang, A. Walsh, M. V. Kovalenko, *Nano Lett.* **2015**, *15*, 3692.
- [74] S. Albrecht, M. Saliba, J. P. C. Baena, F. Lang, L. Kegelmann, M. Mews, L. Steier, A. Abate, J. Rappich, L. Korte, *Energy Environ. Sci.* **2016**, *9*, 81.
- [75] T. Todorov, T. Gershon, O. Gunawan, Y. S. Lee, C. Sturdevant, L. Y. Chang, S. Guha, *Adv. Energy Mater.* **2015**, *5*, 1500799.
- [76] G. E. Eperon, T. Leijtens, K. A. Bush, R. Prasanna, T. Green, J. T.-W. Wang, D. P. McMeekin, G. Volonakis, R. L. Milot, R. May, *Science* **2016**, *354*, 861.
- [77] P. Gao, M. Grätzel, M. K. Nazeeruddin, *Energy Environ. Sci.* **2014**, *7*, 2448.
- [78] Y. Tao, A. Rohatgi, *Nanostructured Solar Cells*, InTech, **2017**.
- [79] H. Hoppe, N. S. Sariciftci, *J. Mater. Res.* **2004**, *19*, 1924.
- [80] A. Martí, J. Balenzategui, R. Reyna, *J. Appl. Phys.* **1997**, *82*, 4067.
- [81] W. Smith, *Nature* **1873**, *7*, 303.
- [82] D. M. Chapin, C. Fuller, G. Pearson, *J. Appl. Phys.* **1954**, *25*, 676.
- [83] M. A. Green, Y. Hishikawa, W. Warta, E. D. Dunlop, D. H. Levi, J. Hohl-Ebinger, A. W. Ho-Baillie, *Prog. Photovolt.* **2017**, *25*, 668.
- [84] M. Li, Y. T. Li, D. W. Li, Y. T. Long, *Anal. Chim. Acta* **2012**, *734*, 31.
- [85] M. A. Green, *Prog. Photovolt.* **2001**, *9*, 123.
- [86] D. E. Carlson, C. R. Wronski, *Appl. Phys. Lett.* **1976**, *28*, 671.
- [87] J. Britt, C. Ferekides, *Appl. Phys. Lett.* **1993**, *62*, 2851.
- [88] S. Magdassi, M. Grouchko, O. Berezin, A. Kamysny, *Acs Nano* **2010**, *4*, 1943.
- [89] P. Capezzuto, A. Madan, *Plasma Deposition of Amorphous Silicon-Based Materials*, Academic Press, **1995**.
- [90] Y. Liang, Z. Xu, J. Xia, S. T. Tsai, Y. Wu, G. Li, C. Ray, L. Yu, *Adv. Mater.* **2010**, *22*, E135.
- [91] S. Günes, H. Neugebauer, N. S. Sariciftci, *Chem. Rev.* **2007**, *107*, 1324.
- [92] C. C. Chen, W. H. Chang, K. Yoshimura, K. Ohya, J. You, J. Gao, Z. Hong, Y. Yang, *Adv. Mater.* **2014**, *26*, 5670.

- [93] T. R. Andersen, H. F. Dam, M. Hösel, M. Helgesen, J. E. Carlé, T. T. Larsen-Olsen, S. A. Gevorgyan, J. W. Andreasen, J. Adams, N. Li, *Energy Environ. Sci.* **2014**, *7*, 2925.
- [94] F. Machui, M. Hösel, N. Li, G. D. Spyropoulos, T. Ameri, R. R. Søndergaard, M. Jørgensen, A. Scheel, D. Gaiser, K. Kreul, *Energy Environ. Sci.* **2014**, *7*, 2792.
- [95] Y. L. Wu, Y. N. Li, B. S. Ong, *J. Am. Chem. Soc.* **2007**, *129*, 1862.
- [96] A. Nozik, *Physica E*, **2002**, *14*, 115.
- [97] W.-J. Yin, J.-H. Yang, J. Kang, Y. Yan, S.-H. Wei, *J. Mater. Chem. A* **2015**, *3*, 8926.
- [98] M. Grätzel, *Nat. Mater.* **2014**, *13*, 838.
- [99] S. Chung, J. Lee, H. Song, S. Kim, J. Jeong, Y. Hong, *Appl. Phys. Lett.* **2011**, *98*, 153110.
- [100] M. M. Lee, J. Teuscher, T. Miyasaka, T. N. Murakami, H. J. Snaith, *Science* **2012**, *338*, 643.
- [101] M. Liu, M. B. Johnston, H. J. Snaith, *Nature* **2013**, *501*, 395.
- [102] J. H. Heo, H. J. Han, D. Kim, T. K. Ahn, S. H. Im, *Energy Environ. Sci.* **2015**, *8*, 1602.
- [103] J. S. Kim, J. H. Lee, J. H. Park, C. Shim, M. Sim, K. Cho, *Adv. Funct. Mater.* **2011**, *21*, 480.
- [104] H. Zhou, L. Yang, A. C. Stuart, S. C. Price, S. Liu, W. You, *Angew. Chem.* **2011**, *123*, 3051.
- [105] Y. Lin, P. Cheng, Y. Li, X. Zhan, *Chem. Commun.* **2012**, *48*, 4773.
- [106] L. Huo, T. Liu, X. Sun, Y. Cai, A. J. Heeger, Y. Sun, *Adv. Mater.* **2015**, *27*, 2938.
- [107] M. C. Scharber, D. Mühlbacher, M. Koppe, P. Denk, C. Waldauf, A. J. Heeger, C. J. Brabec, *Adv. Mater.* **2006**, *18*, 789.
- [108] Z. He, C. Zhong, S. Su, M. Xu, H. Wu, Y. Cao, *Nat. Photon.* **2012**, *6*, 591.
- [109] J. Hou, X. Guo, *Organic Solar Cells*, Springer, **2013**, 17.
- [110] T. Miyazaki, A. Akisawa, T. Kashiwagi, *Renew. Energy* **2005**, *30*, 281.
- [111] C. Lee, X. Wei, J. W. Kysar, J. Hone, *Science* **2008**, *321*, 385.
- [112] X. Li, Y. Zhu, W. Cai, M. Borysiak, B. Han, D. Chen, R. D. Piner, L. Colombo, R. S. Ruoff, *Nano Lett.* **2009**, *9*, 4359.
- [113] S. Bae, H. Kim, Y. Lee, X. Xu, J.-S. Park, Y. Zheng, J. Balakrishnan, T. Lei, H. R. Kim, Y. I. Song, *Nat. Nanotech.* **2010**, *5*, 574.
- [114] S. Rühle, *Solar Energy* **2016**, *130*, 139.
- [115] A. De Vos, *J. Phys. D: Appl. Phys.* **1980**, *13*, 839.
- [116] J. W. Shim, Y. Zhou, C. Fuentes-Hernandez, A. Dindar, Z. Guan, H. Cheun, A. Kahn, B. Kippelen, *Sol. Energy Mater. Sol. Cells* **2012**, *107*, 51.
- [117] S. R. K. AA, T. Ameri, *J. Mater. Sci. Eng.* **2017**, *6*, 16.
- [118] S. H. Park, A. Roy, S. Beaupré, S. Cho, N. Coates, J. S. Moon, D. Moses, M. Leclerc, K. Lee, A. J. Heeger, *Nat. Photon.* **2009**, *3*, 297.
- [119] Z. Liu, J. Li, Z.-H. Sun, G. Tai, S.-P. Lau, F. Yan, *ACS Nano* **2011**, *6*, 810.
- [120] S. Triebwasser, *Phys. Rev.* **1959**, *114*, 63.
- [121] T. Oku, *Nanotech. Rev.* **2014**, *3*, 413.
- [122] Y. Deng, E. Peng, Y. Shao, Z. Xiao, Q. Dong, J. Huang, *Energy Environ. Sci.* **2015**, *8*, 1544.
- [123] Y. Terao, H. Sasabe, C. Adachi, *Appl. Phys. Lett.* **2007**, *90*, 103515.
- [124] Q. Dong, Y. Fang, Y. Shao, P. Mulligan, J. Qiu, L. Cao, J. Huang, *Science* **2015**, *347*, 967.
- [125] G. Xing, N. Mathews, S. Sun, S. S. Lim, Y. M. Lam, M. Grätzel, S. Mhaisalkar, T. C. Sum, *Science* **2013**, *342*, 344.
- [126] L. M. Pazos-Outón, M. Szumilo, R. Lamboll, J. M. Richter, M. Crespo-Quesada, M. Abdi-Jalebi, H. J. Beeson, M. Vrucinić, M. Alsari, H. J. Snaith, *Science* **2016**, *351*, 1430.

- [127] C. H. Wu, J. T. Jiu, T. Araki, H. Koga, T. Sekitani, H. Wang, K. Suganuma, *Nanotechnology* **2017**, 28, 01LT01.
- [128] M. A. Green, A. Ho-Baillie, H. J. Snaith, *Nat. Photon.* **2014**, 8, 506.
- [129] Z. Xiao, Y. Yan, *Adv. Energy Mater.* **2017**.
- [130] G. Niu, X. Guo, L. Wang, *J. Mater. Chem. A* **2015**, 3, 8970.
- [131] A. Swarnkar, A. R. Marshall, E. M. Sanehira, B. D. Chernomordik, D. T. Moore, J. A. Christians, T. Chakrabarti, J. M. Luther, *Science* **2016**, 354, 92.
- [132] G. Grancini, C. Roldán-Carmona, I. Zimmermann, E. Mosconi, X. Lee, D. Martineau, S. Narbey, F. Oswald, F. De Angelis, M. Graetzel, *Nat. Comm.* **2017**, 8, 15684.
- [133] H. Tsai, W. Nie, J.-C. Blancon, C. C. Stoumpos, R. Asadpour, B. Harutyunyan, A. J. Neukirch, R. Verduzco, J. J. Crochet, S. Tretiak, *Nature* **2016**, 536, 312.
- [134] F. C. Krebs, N. Espinosa, M. Hösel, R. R. Søndergaard, M. Jørgensen, *Adv. Mater.* **2014**, 26, 29.
- [135] F. C. Krebs, S. A. Gevorgyan, J. Alstrup, *J. Mater. Chem.* **2009**, 19, 5442.
- [136] B. Zimmermann, H.-F. Schleiermacher, M. Niggemann, U. Würfel, *Sol. Energy Mater. Sol. Cells* **2011**, 95, 1587.
- [137] J. Y. Na, B. Kang, D. H. Sin, K. Cho, Y. D. Park, *Sci. Rep.* **2015**, 5, 13288.
- [138] G. E. Eperon, V. M. Burlakov, P. Docampo, A. Goriely, H. J. Snaith, *Adv. Funct. Mater.* **2014**, 24, 151.
- [139] M. Xiao, F. Huang, W. Huang, Y. Dkhissi, Y. Zhu, J. Etheridge, A. Gray-Weale, U. Bach, Y. B. Cheng, L. Spiccia, *Angew. Chem.* **2014**, 126, 10056.
- [140] K.-M. Lee, C.-J. Lin, B.-Y. Liou, S.-M. Yu, C.-C. Hsu, V. Suryanarayanan, M.-C. Wu, *Sol. Energy Mater. Sol. Cells* **2017**, 172, 368.
- [141] S. Pang, H. Hu, J. Zhang, S. Lv, Y. Yu, F. Wei, T. Qin, H. Xu, Z. Liu, G. Cui, *Chem. Mater.* **2014**, 26, 1485.
- [142] Z. Xiao, C. Bi, Y. Shao, Q. Dong, Q. Wang, Y. Yuan, C. Wang, Y. Gao, J. Huang, *Energy Environ. Sci.* **2014**, 7, 2619.
- [143] N. J. Jeon, J. H. Noh, Y. C. Kim, W. S. Yang, S. Ryu, S. I. Seok, *Nat. Mater.* **2014**, 13, 897.
- [144] J. Ciro, M. A. Mejía-Escobar, F. Jaramillo, *Solar Energy* **2017**, 150, 570.
- [145] H. Chen, F. Ye, W. Tang, J. He, M. Yin, Y. Wang, F. Xie, E. Bi, X. Yang, M. Grätzel, *Nature* **2017**, 550, 92.
- [146] F. Jonas, L. Schrader, *Synth. Met.* **1991**, 41, 831.
- [147] R. Po, C. Carbonera, A. Bernardi, F. Tinti, N. Camaioni, *Sol. Energy Mater. Sol. Cells* **2012**, 100, 97.
- [148] O. Dimitriev, D. Grinko, Y. V. Noskov, N. Ogurtsov, A. Pud, *Synth. Met.* **2009**, 159, 2237.
- [149] D. A. Mengistie, C.-H. Chen, K. M. Boopathi, F. W. Pranoto, L.-J. Li, C.-W. Chu, *ACS applied materials & interfaces* **2014**, 7, 94.
- [150] J. E. McCarthy, C. A. Hanley, L. J. Brennan, V. G. Lambertini, Y. K. Gun'ko, *J. Mater. Chem. C* **2014**, 2, 764.
- [151] N. Kim, S. Kee, S. H. Lee, B. H. Lee, Y. H. Kahng, Y. R. Jo, B. J. Kim, K. Lee, *Adv. Mater.* **2014**, 26, 2268.
- [152] N. Kim, H. Kang, J. H. Lee, S. Kee, S. H. Lee, K. Lee, *Adv. Mater.* **2015**, 27, 2317.
- [153] L. Yang, T. Zhang, H. Zhou, S. C. Price, B. J. Wiley, W. You, *ACS Appl. Mater. Interfaces* **2011**, 3, 4075.
- [154] Y. Galagan, J.-E. J. Rubingh, R. Andriessen, C.-C. Fan, P. W. Blom, S. C. Veenstra, J. M. Kroon, *Sol. Energy Mater. Sol. Cells* **2011**, 95, 1339.
- [155] D. Bryant, P. Greenwood, J. Troughton, M. Wijdekop, M. Carnie, M. Davies, K. Wojciechowski, H. J. Snaith, T. Watson, D. Worsley, *Adv. Mater.* **2014**, 26, 7499.

- [156] J. H. Seo, I. Hwang, H. D. Um, S. Lee, K. Lee, J. Park, H. Shin, T. H. Kwon, S. J. Kang, K. Seo, *Adv. Mater.* **2017**, *29*, 1701479.
- [157] Y. Yu, X. Xiao, Y. Zhang, K. Li, C. Yan, X. Wei, L. Chen, H. Zhen, H. Zhou, S. Zhang, *Adv. Mater.* **2016**, *28*, 4926.
- [158] M. Hösel, R. R. Søndergaard, D. Angmo, F. C. Krebs, *Adv. Eng. Mater.* **2013**, *15*, 995.
- [159] K. Li, H. Zhen, L. Niu, X. Fang, Y. Zhang, R. Guo, Y. Yu, F. Yan, H. Li, Z. Zheng, *Adv. Mater.* **2014**, *26*, 7271.
- [160] C.-C. Lin, M.-C. Chiang, Y.-W. Chen, *Thin Solid Films* **2009**, *518*, 1241.
- [161] Y. Shao, Y. Yuan, J. Huang, *Nat. Energy* **2016**, *1*, 15001.
- [162] K.-H. Choi, J. Kim, Y.-J. Noh, S.-I. Na, H.-K. Kim, *Sol. Energy Mater. Sol. Cells* **2013**, *110*, 147.
- [163] H. Zhang, J. Cheng, F. Lin, H. He, J. Mao, K. S. Wong, A. K.-Y. Jen, W. C. Choy, *ACS Nano* **2015**, *10*, 1503.
- [164] J. W. Jo, M. S. Seo, M. Park, J. Y. Kim, J. S. Park, I. K. Han, H. Ahn, J. W. Jung, B. H. Sohn, M. J. Ko, *Adv. Funct. Mater.* **2016**, *26*, 4464.
- [165] D.-Y. Khang, H. Jiang, Y. Huang, J. A. Rogers, *Science* **2006**, *311*, 208.
- [166] X.-L. Ou, M. Xu, J. Feng, H.-B. Sun, *Sol. Energy Mater. Sol. Cells* **2016**, *157*, 660.
- [167] Y. Li, L. Meng, Y. M. Yang, G. Xu, Z. Hong, Q. Chen, J. You, G. Li, Y. Yang, Y. Li, *Nat. Comm.* **2016**, *7*, 10214.
- [168] M. Kaltenbrunner, M. S. White, E. D. Głowacki, T. Sekitani, T. Someya, N. S. Sariciftci, S. Bauer, *Nat. Comm.* **2012**, *3*, 770.
- [169] M. Kaltenbrunner, G. Adam, E. D. Głowacki, M. Drack, R. Schwödiauer, L. Leonat, D. H. Apaydin, H. Groiss, M. C. Scharber, M. S. White, *Nat. Mater.* **2015**, *14*, 1032.
- [170] D. J. Lipomi, B. C. K. Tee, M. Vosgueritchian, Z. Bao, *Adv. Mater.* **2011**, *23*, 1771.
- [171] H. Miyake, S. Ye, M. Osawa, *Electrochem. Commun.* **2002**, *4*, 973.
- [172] Y. Zhou, F. Li, S. Barrau, W. Tian, O. Inganäs, F. Zhang, *Sol. Energy Mater. Sol. Cells* **2009**, *93*, 497.
- [173] D. Lee, D. Paeng, H. K. Park, C. P. Grigoropoulos, *ACS nano* **2014**, *8*, 9807.
- [174] P. Lee, J. Lee, H. Lee, J. Yeo, S. Hong, K. H. Nam, D. Lee, S. S. Lee, S. H. Ko, *Adv. Mater.* **2012**, *24*, 3326.
- [175] G. Oskam, J. Long, A. Natarajan, P. Searson, *J. Phys. D: Appl. Phys.* **1998**, *31*, 1927.
- [176] A. Hilmi, J. H. Luong, *Anal. Chem.* **2000**, *72*, 4677.
- [177] J. Perelaer, B. J. de Gans, U. S. Schubert, *Adv. Mater.* **2006**, *18*, 2101.
- [178] X. Liu, X. Zhou, Y. Li, Z. Zheng, *Chemistry—An Asian Journal* **2012**, *7*, 862.
- [179] L. A. Porter, H. C. Choi, J. Schmeltzer, A. E. Ribbe, L. C. Elliott, J. M. Buriak, *Nano Lett.* **2002**, *2*, 1369.
- [180] K. J. Park, H.-C. Koo, T. Lim, M. J. Kim, O. J. Kwon, J. J. Kim, *J. Electrochem. Soc.* **2011**, *158*, D541.
- [181] S. H. Ko, H. Pan, C. P. Grigoropoulos, C. K. Luscombe, J. M. Fréchet, D. Poulidakos, *Appl. Phys. Lett.* **2007**, *90*, 141103.
- [182] A. Kamyshny, S. Magdassi, *Small* **2014**, *10*, 3515.
- [183] Y.-H. Tak, K.-B. Kim, H.-G. Park, K.-H. Lee, J.-R. Lee, *Thin Solid Films* **2002**, *411*, 12.
- [184] C.-C. Chen, L. Dou, J. Gao, W.-H. Chang, G. Li, Y. Yang, *Energy Environ. Sci.* **2013**, *6*, 2714.
- [185] R. E. Beal, D. J. Slotcavage, T. Leijtens, A. R. Bowering, R. A. Belisle, W. H. Nguyen, G. F. Burkhard, E. T. Hoke, M. D. McGehee, *J. Phys. Chem. Lett.* **2016**, *7*, 746.

- [186] Y. H. Chen, C. W. Chen, Z. Y. Huang, W. C. Lin, L. Y. Lin, F. Lin, K. T. Wong, H. W. Lin, *Adv. Mater.* **2014**, *26*, 1129.
- [187] Y. Jiang, B. Luo, F. Jiang, F. Jiang, C. Fuentes-Hernandez, T. Liu, L. Mao, S. Xiong, Z. Li, T. Wang, *Nano Lett.* **2016**, *16*, 7829.
- [188] J. Huang, G. Li, Y. Yang, *Adv. Mater.* **2008**, *20*, 415.
- [189] N.-G. Park, *J. Phys. Chem. Lett.* **2013**, *4*, 2423.
- [190] C. Wehrenfennig, G. E. Eperon, M. B. Johnston, H. J. Snaith, L. M. Herz, *Adv. Mater.* **2014**, *26*, 1584.
- [191] C. S. Ponceca Jr, T. J. Savenije, M. Abdellah, K. Zheng, A. Yartsev, T. r. Pascher, T. Harlang, P. Chabera, T. Pullerits, A. Stepanov, *J. Am. Chem. Soc.* **2014**, *136*, 5189.
- [192] H. J. Snaith, *J. Phys. Chem. Lett.* **2013**, *4*, 3623.
- [193] J. You, Z. Hong, Y. M. Yang, Q. Chen, M. Cai, T. B. Song, C. C. Chen, S. Lu, Y. Liu, H. Zhou, Y. Yang, *ACS Nano* **2014**, *8*, 1674.
- [194] D. Yang, R. Yang, J. Zhang, Z. Yang, S. F. Liu, C. Li, *Energy Environ. Sci.* **2015**.
- [195] D. Liu, T. L. Kelly, *Nat. Photon.* **2014**, *8*, 133.
- [196] Z. Li, S. A. Kulkarni, P. P. Boix, E. Shi, A. Cao, K. Fu, S. K. Batabyal, J. Zhang, Q. Xiong, L. H. Wong, *ACS nano* **2014**, *8*, 6797.
- [197] P. You, Z. Liu, Q. Tai, S. Liu, F. Yan, *Adv. Mater.* **2015**.
- [198] N. J. Jeon, J. H. Noh, W. S. Yang, Y. C. Kim, S. Ryu, J. Seo, S. I. Seok, *Nature* **2015**, *517*, 476.
- [199] C. D. Bailie, M. G. Christoforo, J. P. Mailoa, A. R. Bowring, E. L. Unger, W. H. Nguyen, J. Burschka, N. Pellet, J. Z. Lee, M. Grätzel, *Energy Environ. Sci.* **2015**, *8*, 956.
- [200] J. H. Heo, S. H. Im, *Adv. Mater.* **2015**, *26*, 8179.
- [201] F. Fu, T. Feurer, T. P. Weiss, S. Pisoni, E. Avancini, C. Andres, S. Buecheler, A. N. Tiwari, *Nat. Energy* **2016**, *2*, 16190.
- [202] C. J. Emmott, A. Urbina, J. Nelson, *Sol. Energy Mater. Sol. Cells* **2012**, *97*, 14.
- [203] M. Cai, Y. Wu, H. Chen, X. Yang, Y. Qiang, L. Han, *Adv. Sci.* **2016**.
- [204] S. K. Hau, H.-L. Yip, J. Zou, A. K.-Y. Jen, *Org. Electron.* **2009**, *10*, 1401.
- [205] J. F. Salinas, H. L. Yip, C. C. Chueh, C. Z. Li, J. L. Maldonado, A. K. Y. Jen, *Adv. Mater.* **2012**, *24*, 6362.
- [206] M. Dianetti, F. Di Giacomo, G. Polino, C. Ciceroni, A. Liscio, A. D'Epifanio, S. Licocchia, T. Brown, A. Di Carlo, F. Brunetti, *Sol. Energy Mater. Sol. Cells* **2015**, *140*, 150.
- [207] H. Sung, N. Ahn, M. S. Jang, J. K. Lee, H. Yoon, N. G. Park, M. Choi, *Adv. Energy Mater.* **2016**, *6*, 1501873.
- [208] X. Li, D. Bi, C. Yi, J.-D. Décoppet, J. Luo, S. M. Zakeeruddin, A. Hagfeldt, M. Grätzel, *Science* **2016**, *353*, 58.
- [209] M. Saliba, T. Matsui, J.-Y. Seo, K. Domanski, J.-P. Correa-Baena, M. K. Nazeeruddin, S. M. Zakeeruddin, W. Tress, A. Abate, A. Hagfeldt, *Energy Environ. Sci.* **2016**, *9*, 1989.
- [210] D. Angmo, T. T. Larsen-Olsen, M. Jørgensen, R. R. Søndergaard, F. C. Krebs, *Adv. Energy Mater.* **2013**, *3*, 172.
- [211] T. Leijtens, G. E. Eperon, N. K. Noel, S. N. Habisreutinger, A. Petrozza, H. J. Snaith, *Adv. Energy Mater.* **2015**, *5*, 1500962.
- [212] J. You, L. Meng, T.-B. Song, T.-F. Guo, Y. M. Yang, W.-H. Chang, Z. Hong, H. Chen, H. Zhou, Q. Chen, *Nat. Nanotech.* **2015**, *11*, 75.
- [213] C. Yeon, S. J. Yun, J. Kim, J. W. Lim, *Adv. Electron. Mater.* **2015**, *1*, 1500121.
- [214] Y. H. Lee, J. Luo, M. K. Son, P. Gao, K. T. Cho, J. Seo, S. M. Zakeeruddin, M. Grätzel, M. K. Nazeeruddin, *Adv. Mater.* **2016**, *28*, 3966.

- [215] Y. Han, S. Meyer, Y. Dkhissi, K. Weber, J. M. Pringle, U. Bach, L. Spiccia, Y.-B. Cheng, *J. Mater. Chem. A* **2015**, 3, 8139.
- [216] D. H. Kim, J. H. Ahn, W. M. Choi, H. S. Kim, T. H. Kim, J. Z. Song, Y. G. Y. Huang, Z. J. Liu, C. Lu, J. A. Rogers, *Science* **2008**, 320, 507.
- [217] S. P. Lacour, J. Jones, S. Wagner, T. Li, Z. G. Suo, *Proc. IEEE* **2005**, 93, 1459.
- [218] Y. Meng, Y. Zhao, C. Hu, H. Cheng, Y. Hu, Z. Zhang, G. Shi, L. Qu, *Advanced materials* **2013**, 25, 2326.
- [219] M. Ramuz, B. C. K. Tee, J. B. H. Tok, Z. Bao, *Adv. Mater.* **2012**, 24, 3223.
- [220] C. Dagdeviren, Y. Shi, P. Joe, R. Ghaffari, G. Balooch, K. Usgaonkar, O. Gur, P. L. Tran, J. R. Crosby, M. Meyer, *Nat. Mater.* **2015**, 14, 728.
- [221] N. Matsuhisa, M. Kaltenbrunner, T. Yokota, H. Jinno, K. Kuribara, T. Sekitani, T. Someya, *Nat. Comm.* **2015**, 6, 7461.
- [222] D. H. Kim, J. Xiao, J. Song, Y. Huang, J. A. Rogers, *Adv. Mater.* **2010**, 22, 2108.
- [223] D.-Y. Khang, J. A. Rogers, H. H. Lee, *Adv. Funct. Mater* **2009**, 19, 1526.
- [224] F. C. Krebs, *Solar Energy Materials and Solar Cells* **2009**, 93, 465.
- [225] K. Alzoubi, M. M. Hamasha, S. Lu, B. Sammakia, *J. Display Technol.* **2011**, 7, 593.
- [226] Y. Lan, W. Peng, Y. Lo, J. He, *Org. Electron.* **2010**, 11, 670.
- [227] T. Ma, X. Fang, M. Akiyama, K. Inoue, H. Noma, E. Abe, *J. Electroanal. Chem.* **2004**, 574, 77.
- [228] D. Alemu, H.-Y. Wei, K.-C. Ho, C.-W. Chu, *Energy Environ. Sci.* **2012**, 5, 9662.
- [229] T. T. Larsen-Olsen, R. R. Søndergaard, K. Norrman, M. Jørgensen, F. C. Krebs, *Energy Environ. Sci.* **2012**, 5, 9467.
- [230] J. E. Carlé, T. R. Andersen, M. Helgesen, E. Bundgaard, M. Jørgensen, F. C. Krebs, *Sol. Energy Mater. Sol. Cells* **2013**, 108, 126.
- [231] Y.-M. Chang, C.-P. Chen, J.-M. Ding, C.-Y. Leu, M.-J. Lee, R.-D. Chen, *Sol. Energy Mater. Sol. Cells* **2013**, 109, 91.
- [232] C. Girotto, B. P. Rand, S. Steudel, J. Genoe, P. Heremans, *Org. Electron.* **2009**, 10, 735.
- [233] M. Kaltenbrunner, G. Adam, E. D. Głowacki, M. Drack, R. Schwödiauer, L. Leonat, D. H. Apaydin, H. Groiss, M. C. Scharber, M. S. White, *Nat. Mater.* **2015**, 14, 1032.
- [234] S. Xu, Y. Zhang, L. Jia, K. E. Mathewson, K.-I. Jang, J. Kim, H. Fu, X. Huang, P. Chava, R. Wang, *Science* **2014**, 344, 70.
- [235] Q. Cao, H.-s. Kim, N. Pimparkar, J. P. Kulkarni, C. Wang, M. Shim, K. Roy, M. A. Alam, J. A. Rogers, *Nature* **2008**, 454, 495.
- [236] T. Sekitani, U. Zschieschang, H. Klauk, T. Someya, *Nat. Mater.* **2010**, 9, 1015.
- [237] J.-S. Yu, I. Kim, J.-S. Kim, J. Jo, T. T. Larsen-Olsen, R. R. Søndergaard, M. Hösel, D. Angmo, M. Jørgensen, F. C. Krebs, *Nanoscale* **2012**, 4, 6032.
- [238] G. Li, R. Zhu, Y. Yang, *Nat. Photon.* **2012**, 6, 153.
- [239] Y. Wang, S. W. Tong, X. F. Xu, B. Özyilmaz, K. P. Loh, *Advanced Materials* **2011**, 23, 1514.
- [240] R. R. Lunt, J. B. Benziger, S. R. Forrest, *Adv. Mater.* **2010**, 22, 1233.
- [241] Z. Xiao, Q. Dong, C. Bi, Y. Shao, Y. Yuan, J. Huang, *Adv. Mater.* **2014**, 26, 6503.
- [242] J. D. Chen, C. Cui, Y. Q. Li, L. Zhou, Q. D. Ou, C. Li, Y. Li, J. X. Tang, *Adv. Mater.* **2015**, 27, 1035.
- [243] M. Zhang, Y. Wang, M. Xu, W. Ma, R. Li, P. Wang, *Energy Environ. Sci.* **2013**, 6, 2944.

- [244] B. Dudem, J. H. Heo, J. W. Leem, J. S. Yu, S. H. Im, *J. Mater. Chem. A* **2016**, *4*, 7573.
- [245] S.-B. Rim, S. Zhao, S. R. Scully, M. D. McGehee, P. Peumans, *Appl. Phys. Lett.* **2007**, *91*, 243501.
- [246] H. Zhen, K. Li, Z. Huang, Z. Tang, R. Wu, G. Li, X. Liu, F. Zhang, *Appl. Phys. Lett.* **2012**, *100*, 213901.
- [247] M. Berginski, J. Hüpkens, M. Schulte, G. Schöpe, H. Stiebig, B. Rech, M. Wuttig, *J. Appl. Phys.* **2007**, *101*, 074903.
- [248] Y. Chiba, A. Islam, R. Komiya, N. Koide, L. Han, *Appl. Phys. Lett.* **2006**, *88*, 223505.
- [249] K. Li, H. Zhen, Z. Huang, G. Li, X. Liu, *ACS Appl. Mater. Interfaces* **2012**, *4*, 4393.
- [250] D. H. Ko, J. R. Tumbleston, W. Schenck, R. Lopez, E. T. Samulski, *J. Phys. Chem. C* **2011**, *115*, 4247.
- [251] X. Li, W. C. Choy, L. Huo, F. Xie, W. E. Sha, B. Ding, X. Guo, Y. Li, J. Hou, J. You, *Adv. Mater.* **2012**, *24*, 3046.
- [252] W. Zhang, M. Saliba, S. D. Stranks, Y. Sun, X. Shi, U. Wiesner, H. J. Snaith, *Nano Lett.* **2013**, *13*, 4505.
- [253] Y. H. Lee, T. K. Lee, I. Song, H. Yu, J. Lee, H. Ko, S. K. Kwak, J. H. Oh, *Adv. Mater.* **2016**, *28*, 4976.
- [254] Z. Fang, H. Zhu, Y. Yuan, D. Ha, S. Zhu, C. Preston, Q. Chen, Y. Li, X. Han, S. Lee, *Nano Lett.* **2013**, *14*, 765.
- [255] G. Kang, K. Bae, M. Nam, D. H. Ko, K. Kim, W. J. Padilla, *Energy Environ. Sci.* **2015**, *8*, 2650.
- [256] C. Pacholski, A. Kornowski, H. Weller, *Angew. Chem. Inter. Ed.* **2002**, *41*, 1188.
- [257] R. Guo, Y. Yu, J. Zeng, X. Liu, X. Zhou, L. Niu, T. Gao, K. Li, Y. Yang, F. Zhou, Z. Zheng, *Adv. Sci.* **2015**, *2*, 1400021.
- [258] K. Forberich, G. Dennler, M. C. Scharber, K. Hingerl, T. Fromherz, C. J. Brabec, *Thin Solid Films* **2008**, *516*, 7167.
- [259] D.-H. Ko, J. R. Tumbleston, K. J. Henderson, L. E. Euliss, J. M. DeSimone, R. Lopez, E. T. Samulski, *Soft Matter* **2011**, *7*, 6404.
- [260] S. Chhajed, M. F. Schubert, J. K. Kim, E. F. Schubert, *Appl. Phys. Lett.* **2008**, *93*, 251108.
- [261] B. M. Phillips, P. Jiang, B. Jiang, *Appl. Phys. Lett.* **2011**, *99*, 191103
- [262] F. Ruske, C. Jacobs, V. Sittinger, B. Szyszka, W. Werner, *Thin Solid Films* **2007**, *515*, 8695.
- [263] C. Preston, Z. Fang, J. Murray, H. Zhu, J. Dai, J. N. Munday, L. Hu, *J. Mater. Chem. C* **2014**, *2*, 1248.
- [264] Z. Fang, H. Zhu, Y. Yuan, D. Ha, S. Zhu, C. Preston, Q. Chen, Y. Li, X. Han, S. Lee, *Nano Lett.* **2014**, *14*, 765.
- [265] Y. Chiba, A. Islam, R. Komiya, N. Koide, L. Han, *Appl. Phys. Lett.* **2006**, *88*, 223505.
- [266] J. Krc, B. Lipovsek, M. Bokalic, A. Campa, T. Oyama, M. Kambe, T. Matsui, H. Sai, M. Kondo, M. Topic, *Thin Solid Films* **2010**, *518*, 3054.
- [267] G. Kang, K. Bae, M. Nam, D.-H. Ko, K. Kim, W. J. Padilla, *Energy Environ. Sci.* **2015**, *8*, 2650.